WASHINGTON UNIVERSITY IN ST. LOUIS
Department of Physics

Dissertation Examination Committee:
Kater W. Murch, Chair
James H. Buckley
Erik A. Henrikson
Mark Lawrence
Karthik Ramanathan
Chong Zu

Parametric Control and Amplification in Superconducting Quantum Systems: From Entanglement Probes to PT-Symmetric Architectures

by
Chandrashekhar Rao Gaikwad

A dissertation presented to
Washington University in St. Louis
in partial fulfillment of the
requirements for the degree
of Doctor of Philosophy

December 2025
St. Louis, Missouri

Contents

List of Figures

List of Tables

Acknowledgements

I could not have asked for a better place to pursue my PhD. My time at Washington University in St. Louis has been shaped by exceptional mentorship, a supportive community, and many friendships that I will always value.

I would like to express my deepest gratitude to my advisor, Kater Murch. Throughout my PhD journey, Kater has been a constant source of guidance, encouragement, and inspiration. When I first joined the Murch Lab, I started with simple projects, but he soon directed me toward research that would lead to publications and helped me become the go-to person for microwave engineering in the group. His experience, from designing experiments to completing and publishing them, provided me with a well-rounded foundation as a scientist. Beyond academics, Kater also played an essential role in my career development. His support was instrumental in helping me secure a position at IBM immediately after my PhD. He also set an example of maintaining a healthy work-life balance, something I hope to carry forward. I am deeply grateful for his mentorship, patience, and the many dinners and gatherings at his home. Those lab parties will be greatly missed. Thank you, Kater, for being an exceptional advisor during my doctoral studies.

I am also fortunate to have had a second mentor, James Buckley. Jim's patience, enthusiasm, and eagerness to learn new things have always impressed me. I hope to remain as motivated and curious as he is throughout my career. Thank you, Jim, for bringing me into the ADMX community and for everything I learned there, from designing amplifiers to gaining a broader scientific perspective. Your support contributed significantly to the completion of my PhD projects.

My sincere appreciation extends to all my colleagues and mentors in the lab. I am especially grateful to Daria Kowasari for his patient and skillful fabrication of my designs,

particularly given how hesitant I have always been to enter the cleanroom. Thank you, Daria, for handling the fabrication side of my work with such care. I would also like to thank Patrick Harrington and Jonathan Monroe, who guided me in my early years and taught me how to measure and understand quantum systems. I am equally thankful to Weijian Cheng, whose insight and support as a postdoc strengthened my research. To every member of the Murch Lab, past and present, thank you for the thoughtful conversations, enjoyable collaborations, and the supportive environment that made my time in the lab so meaningful.

I would also like to thank my PhD committee members: Erik A. Henrikson, Mark Lawrence, Karthik Ramanathan, and Chong Zu, for their time, guidance, and constructive feedback. Additionally, I am grateful to the Physics Department staff, especially Sarah Akin, for their constant help with logistics throughout my time at WashU.

Finally, I am deeply thankful to my family. Even though it was often difficult to explain what I was working on from far away, they never stopped believing in me. Their unconditional support made this journey possible.

Chandrashekhar Rao Gaikwad

Washington University in St. Louis

December 2025

ABSTRACT OF THE DISSERTATION

Parametric Control and Amplification in Superconducting Quantum Systems: From Entanglement Probes to PT-Symmetric Architectures

by

Chandrashekhar Rao Gaikwad

Doctor of Philosophy in Physics

Washington University in St.Louis, 2025

Professor Kater W. Murch (Chair)

The precise control, entanglement, and measurement of quantum systems are central challenges in realizing scalable quantum information processing. This dissertation investigates how parametric modulation and engineered nonlinearity can be harnessed to both manipulate and measure superconducting qubits with high fidelity. In one part, controlled parametric drives are used to generate entanglement between qubit pairs and employ their joint states as probes of environmental dynamics. This approach enables the exploration of the non-Markovian nature of quantum environments, revealing how memory effects influence qubit coherence and energy relaxation. In a separate but conceptually related study, the same principle of parametric driving is utilized to design and analyze quantum-limited amplifiers based on three-wave mixing in weakly nonlinear Josephson circuits. An amplifier with a higher coupling quality factor than conventional JPAs is employed, allowing the two modes of a parity-time (PT) symmetric dimer to be mapped onto the in-phase (I) and quadrature (Q) components of the Josephson parametric amplifier. This mapping enables controlled exploration of non-Hermitian dynamics and mode coalescence within the amplifier's quadrature space, offering new insights into PT-symmetric behavior and quantum-limited detection.

Collectively, these investigations unify the themes of parametric control, entanglement, and amplification, advancing the broader understanding of quantum measurement and open-system dynamics.

So it goes.

—Kurt Vonnegut, Slaughterhouse-Five

Chapter 1

Introduction

Scalable quantum information processing hinges on three capabilities: coherent control of quantum degrees of freedom, reliable generation and verification of entanglement, and high-fidelity measurement near the quantum limit. In superconducting circuits, these capabilities can be addressed by a single physical resource—*parametric coupling* enabled by Josephson nonlinearity. By modulating circuit parameters in time, one activates controlled mixing processes that exchange energy between modes, tailor effective Hamiltonians, and transduce weak signals with minimal added noise. The central theme of this dissertation is that *parametric mixing* provides a unifying mechanism linking entanglement-based probes of open-system dynamics with quantum-limited amplification, and even opens a route to explore non-Hermitian (PT-symmetric) physics within measurement hardware.

Parametric interactions arise when a system parameter (frequency, coupling rate, or phase) is driven near a sum or difference of mode frequencies. In weakly nonlinear Josephson circuits, such drives realize effective three-wave or four-wave mixing that can be switched on and off with microwave tones. The same mechanism that mediates exchange-type two-qubit gates (e.g., iSWAP) can, under different biasing and coupling conditions, produce phase-sensitive gain that amplifies one quadrature while de-amplifying the other. This shared origin ties together the *preparation* of delicate quantum states and their *readout* at the

quantum limit, allowing control and measurement to be co-designed rather than treated as disjoint tasks.

Building on this perspective, the first part of the thesis uses entanglement as a metrological resource to interrogate environmental memory. A pair of superconducting qubits is entangled via parametric gates and coupled to a third qubit that plays the role of a tunable environment. By injecting controlled dephasing noise into the environment, we vary its effective memory time and observe a crossover from non-Markovian to Markovian dynamics in the evolution of bipartite correlations. At sufficiently high dephasing rates, signatures consistent with a quantum Zeno regime emerge, in which frequent phase randomization suppresses environment-induced evolution and restores dynamics approaching those of uncoupled probes.

The second part focuses on parametric amplification as both a practical tool for measurement and a platform for exploring non-Hermitian physics. We examine design choices—coupling quality factor, pump configuration, impedance environment, and saturation mechanisms—that set the achievable gain–bandwidth product, noise temperature, and dynamic range of Josephson parametric amplifiers. Leveraging these design levers, we then implement an amplifier with higher coupling-Q than conventional JPAs and show how the two modes of a PT-symmetric dimer can be mapped onto the in-phase (I) and quadrature (Q) components of the device. This mapping enables controlled access to PT-symmetric and PT-broken regimes, with observable features associated with exceptional points and mode coalescence, all within the quadrature space of a working measurement device.

Contributions

This dissertation advances a unified view of parametric mixing as a control–and–measurement primitive in superconducting circuits: it demonstrates entanglement generation with parametrically activated exchange gates under realistic loss and anharmonicity constraints; establishes an entangled-pair protocol to probe environmental memory and its dephasing-controlled crossover to Markovian behavior, including quantum-Zeno-like suppression at high rates; develops a practical design framework for quantum-limited amplification that clarifies gain–bandwidth–noise–saturation trade-offs; and realizes PT-symmetric dynamics within a working Josephson parametric amplifier by mapping the dimer's modes onto I/Q quadratures, enabling controlled exploration of exceptional-point physics in a measurement setting.

Thesis outline

Chapter 2: Foundations of superconducting qubits; intuitive view of anharmonicity; loss channels and Purcell estimates; parametric iSWAP-type gates for entanglement.

Chapter 3: Entangled-pair probing of a third qubit as a tunable environment; dephasing-controlled crossover from non-Markovian to Markovian dynamics; high-dephasing quantum-Zeno signatures.

Chapter 4: Quantum-limited parametric amplification in weakly nonlinear Josephson circuits; design levers and performance trade-offs for gain, bandwidth, noise, and saturation.

Chapter 5: Implementation of a high coupling-Q parametric amplifier that realizes an ef-

fective PT-symmetric Hamiltonian via I/Q mapping; observation of exceptional-point features and implications for quantum-limited detection.

As a whole, the dissertation advances a single throughline: parametric mixing is a versatile control–and–measurement primitive that unifies the preparation of quantum states, the diagnosis of environmental memory, and the realization of engineered non-Hermitian dynamics. The chapters that follow develop this arc from fundamentals to applications—beginning with core models and assumptions in Chapter 2, moving to entanglement as a probe of open-system dynamics in Chapter 3, distilling design trade-offs for quantum-limited amplification in Chapter 4, and finally demonstrating PT-symmetric behavior within a working JPA in Chapter 5.

Chapter 2

An Engineer's Approach to Qubits

Wave-particle duality, superposition, and entanglement are among the most intriguing and unique properties of quantum mechanics, with no direct classical counterparts. These phenomena, which defy classical intuition, form the foundation of quantum computing. In a controlled environment, these properties can be harnessed to build a quantum computer, a revolutionary computational device that leverages the principles of quantum mechanics to solve problems intractable for classical computers [1]. Quantum computers have been proposed to be powerful tools for simulating quantum systems, optimizing complex processes, and solving cryptographic problems, all while adhering strictly to the laws of quantum physics [2].

At the heart of a quantum computer lies the **qubit** (quantum bit), the fundamental carrier of quantum information. Unlike classical bits, which hold a single value (0 or 1), qubits can be in superpositions, and—most importantly—many qubits can be *entangled*, creating correlations that cannot be split into independent pieces. With n qubits the joint state lives in a 2^n-dimensional Hilbert space. Quantum algorithms set relative phases so that interference *boosts* the probability of correct answers and *cancels* many wrong ones (as in Shor's factoring, which achieves an exponential speedup, and Grover's search, which achieves a quadratic speedup). Although measurement returns a single outcome, the work

has already been done in the larger Hilbert space; when a problem's structure fits this use of superposition, entanglement, and interference, quantum computers can outperform classical ones. Quantum computing isn't just "faster computers." It's faster for specific problems (cryptography, optimization, quantum chemistry, etc.). A qubit is typically realized using an **anharmonic oscillator**, a device capable of storing and manipulating measurable quanta of energy, such as photons or other excitations in superconducting circuits [3]. The anharmonic nature of these oscillators allows for the creation of discrete energy levels, which can be used to encode qubits (two-level systems), qutrits (three-level systems), and beyond.

In this chapter, we explore the properties of anharmonic oscillators that underpin qubit design. We develop both an intuitive and mathematical understanding of qubit anharmonicity and measurement, and we discuss the main mechanisms of qubit decoherence.

2.1 Harmonic and anharmonic resonator

2.1.1 Simple Harmonic Oscillator

A simple and classic example of a harmonic oscillator is a mass attached to a spring connected to a wall. In such a system, the potential energy is quadratic, and this leads to a special property: the time period of oscillations is independent of the amplitude. This unique feature implies that the period of a harmonic oscillator is independent of the stored energy in the oscillator. An electrical equivalent of the harmonic oscillator is an **LC tank circuit**, as shown in Fig. 2.1. The total energy stored in this circuit is the sum of the energy stored in each element and can be written as:

$$H_{\mathrm{LC}}(\phi, Q) = \frac{Q^2}{2C} + \frac{\phi^2}{2L}, \tag{2.1}$$

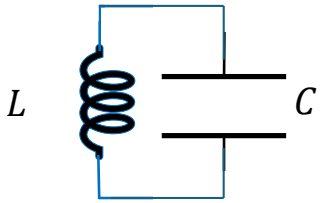

Fig. 2.1: LC circuit (inductor L in series with capacitor C) as the electrical analog of a simple harmonic oscillator. The resonant frequency $\omega = 1/\sqrt{LC}$ and characteristic impedance $Z = \sqrt{L/C}$ follow directly from the quadratic energy $Q^2/(2C) + \phi^2/(2L)$ in Eq. (2.1).

which is the Hamiltonian of a simple harmonic oscillator with frequency

$$\omega = \frac{1}{\sqrt{LC}}, \qquad Z \equiv \sqrt{\frac{L}{C}} \text{ (characteristic impedance)}. \tag{2.2}$$

Here, ϕ is the flux associated with the inductor of inductance L, and Q is the charge on the capacitor of capacitance C. When treated quantum mechanically, we promote the flux and charge to operators, and the harmonic oscillator is described by the Hamiltonian:

$$\hat{H} = \frac{\hat{Q}^2}{2C} + \frac{\hat{\phi}^2}{2L}, \tag{2.3}$$

where $\phi \to \hat{\phi}$ and $Q \to \hat{Q}$ are operators obeying the canonical commutation relation

$$[\hat{\phi}, \hat{Q}] = i\hbar. \tag{2.4}$$

It is convenient to define the zero-point (vacuum) fluctuations

$$\phi_{\text{zpf}} = \sqrt{\frac{\hbar}{2C\omega}} = \sqrt{\frac{\hbar Z}{2}}, \qquad Q_{\text{zpf}} = \sqrt{\frac{\hbar C\omega}{2}} = \sqrt{\frac{\hbar}{2Z}}, \tag{2.5}$$

which satisfy $\phi_{\text{zpf}}\, Q_{\text{zpf}} = \hbar/2$. Using these scales we introduce the bosonic ladder operators

$$\hat{a} = \frac{1}{2}\left(\frac{\hat{\phi}}{\phi_{\text{zpf}}} + i\,\frac{\hat{Q}}{Q_{\text{zpf}}}\right), \qquad \hat{a}^\dagger = \frac{1}{2}\left(\frac{\hat{\phi}}{\phi_{\text{zpf}}} - i\,\frac{\hat{Q}}{Q_{\text{zpf}}}\right), \tag{2.6}$$

equivalently,

$$\hat{\phi} = \phi_{\text{zpf}}\big(\hat{a} + \hat{a}^\dagger\big)\,, \qquad \hat{Q} = -\,i\,Q_{\text{zpf}}\big(\hat{a} - \hat{a}^\dagger\big)\,. \tag{2.7}$$

The choice (2.5) with the commutator (2.4) ensures that the ladder operators obey the canonical bosonic algebra

$$[\hat{a}, \hat{a}^\dagger] = 1. \tag{2.8}$$

To express the Hamiltonian in number-operator form, substitute Eq. (2.7) into Eq. (2.3); using $C\omega = 1/Z$ and $\omega/Z = 1/L$ and simplifying yields

$$\hat{H} = \hbar\omega\left(\hat{a}^\dagger\hat{a} + \frac{1}{2}\right) = \hbar\omega\left(\hat{n} + \frac{1}{2}\right), \tag{2.9}$$

where $\hat{n} \equiv \hat{a}^\dagger\hat{a}$ is the photon-number operator. Thus the quantized LC circuit is exactly a quantum simple harmonic oscillator with evenly spaced energy levels $E_n = \hbar\omega\left(n + \frac{1}{2}\right)$. This property—where the resonator's frequency remains independent of the number of photons it contains—is directly analogous to the classical case discussed at the beginning of this section.

However, rather than measuring a single quantum directly, we infer it by detecting a transition between neighboring energy levels, so a one-quantum gain appears as a resolvable change in the system's response. This requires an **anharmonic resonator**, where the

resonant frequency depends on the amount of energy stored in it. An anharmonic resonator can be of two types: (a) a weak nonlinearity leading to nonlinear resonators typically used to make parametric amplifiers, converters, etc.; (b) a sufficiently strong nonlinearity that can exhibit a significant frequency shift even when excited with a single photon, making it possible to measure and control individual quanta of energy and to realize qubits. This property is crucial for quantum computing and quantum sensing applications.

By analogy, a nonlinear electromagnetic resonator capable of storing a single photon and exhibiting a frequency shift can mimic the behavior of a hydrogen atom, making it a suitable candidate for quantum state manipulation and measurement [3]. To make a harmonic resonator anharmonic, one can introduce a nonlinearity into the inductor, the capacitor, or both. However, for the device to be useful as a quantum anharmonic resonator, this nonlinearity must be essentially lossless.

Such a lossless nonlinear element was discovered by Brian D. Josephson in 1962, now known as the Josephson junction [4], a breakthrough that later earned him the Nobel Prize in Physics. The Josephson junction has since become the cornerstone of superconducting quantum circuits, enabling the engineering of highly coherent and controllable quantum devices; see also the comprehensive perspective in [5].

2.1.2 Josephson junctions and superconducting qubits

A Josephson junction (JJ) is a quantum mechanical element consisting of two superconductors separated by a thin insulating barrier (typically $\sim$1–3 nm thick) [6]. It exhibits unique properties due to the coherent tunneling of Cooper pairs, leading to the DC and AC Josephson effects. These junctions form the nonlinear element essential for superconducting quantum circuits [7]. The DC Josephson effect describes a supercurrent flowing across the

junction without an applied voltage:

$$I = I_c \sin(\phi), \tag{2.10}$$

where I is the supercurrent, I_c is the critical current (maximum zero-voltage supercurrent), and ϕ is the phase difference across the junction [8, 9]. The AC Josephson effect relates a constant voltage V to the time evolution of the phase difference:

$$\frac{d\phi}{dt} = \frac{2e}{\hbar} V, \tag{2.11}$$

where e is the electron charge. The nonlinear inductance of a JJ arises from the current–phase relation. For small phase fluctuations ($\phi \ll 1$), the junction behaves as a linear inductor with Josephson inductance:

$$L_J = \frac{\hbar}{2eI_c} = \frac{\Phi_0}{2\pi I_c}, \tag{2.12}$$

where $\Phi_0 = h/2e$ is the magnetic flux quantum. For finite currents ($I \lesssim I_c$), the inductance becomes current-dependent. A simple superconducting qubit can be realized by replacing the linear inductor in an LC resonator with a Josephson junction (JJ), a nonlinear, lossless element typically represented by a cross symbol in circuit diagrams (see Fig. 2.2).

A single photon trapped in such a resonator can shift the transition frequencies via the current-dependent Josephson inductance. The *anharmonicity* is defined as the difference between successive transition frequencies (e.g., $\alpha = \omega_{12} - \omega_{01}$); its magnitude controls spectral selectivity and strongly impacts readout fidelity by improving the effective signal-to-noise ratio (SNR) [5].

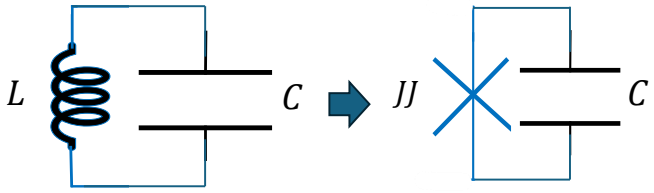

Fig. 2.2: Replacing the linear inductor with a Josephson junction produces a nonlinear, essentially lossless inductance. This converts the LC resonator into an anharmonic oscillator suitable for implementing superconducting qubits.

2.2 Transmon qubit

A transmon qubit is a Josephson junction shunted with a large capacitor. The energy stored in the junction follows from integrating $dU = I(\phi)\, V\, dt$, yielding

$$U_J(\phi) = E_J\,(1 - \cos\phi)\,, \tag{2.13}$$

where the Josephson energy is

$$E_J = \frac{\hbar I_c}{2e} = \frac{\Phi_0 I_c}{2\pi}. \tag{2.14}$$

We explicitly retain the additive constant $+E_J$, which corresponds to the choice of zero for the energy reference.

Now that we know the energy term for the JJ, we can write the full Hamiltonian of the qubit and promote the conjugate variables to quantum operators. The conjugate variables are the phase operator $\hat{\phi}$ and the Cooper-pair number operator $\hat{n}$, which satisfy the canonical commutation relation

$$[\hat{\phi}, \hat{n}] = i. \tag{2.15}$$

The capacitive (charging) energy is quantified by

$$E_C = \frac{e^2}{2C}, \tag{2.16}$$

so the full Hamiltonian reads

$$\hat{H} = 4E_C\,\hat{n}^2 \;+\; E_J\left(1-\cos\hat{\phi}\right). \tag{2.17}$$

Close to the minimum of the potential well at $\phi = 0$, the cosine can be expanded to quartic order,

$$1-\cos\hat{\phi} \;\approx\; \frac{\hat{\phi}^2}{2} - \frac{\hat{\phi}^4}{24}. \tag{2.18}$$

Introducing bosonic annihilation and creation operators b and $b^\dagger$, we write

$$\hat{\phi} = \phi_{\text{zpf}}(b + b^\dagger), \tag{2.19}$$

$$\hat{n} = i\,n_{\text{zpf}}(b^\dagger - b), \tag{2.20}$$

where the zero-point fluctuation amplitudes are

$$\phi_{\text{zpf}} = \left(\frac{2E_C}{E_J}\right)^{1/4}, \tag{2.21}$$

$$n_{\text{zpf}} = \left(\frac{E_J}{32E_C}\right)^{1/4}. \tag{2.22}$$

These satisfy $\phi_{\text{zpf}}\,n_{\text{zpf}} = \frac{1}{2}$, and the harmonic oscillator frequency is

$$\hbar\omega_p = \sqrt{8E_JE_C}. \tag{2.23}$$

Expanding the quartic potential and retaining only number-conserving terms under the rotating-wave approximation gives the effective Hamiltonian

$$\hat{H}_{\text{eff}} = \hbar\omega_p\, b^\dagger b \;-\; \frac{E_C}{2} b^\dagger b \;-\; \frac{E_C}{2} b^\dagger b^\dagger b b \;+\; \text{const}, \tag{2.24}$$

where the constant includes contributions from zero-point fluctuations and the additive E_J offset. In terms of the number operator $\hat{n} = b^\dagger b$, this is often expressed as

$$\hat{H}_{\text{eff}} = \hbar\omega_{01}\,\hat{n} \;-\; \frac{E_C}{2}\hat{n}(\hat{n}-1) \;+\; \text{const.} \tag{2.25}$$

Here the lowest transition frequency is

$$\boxed{\omega_{01} = \frac{1}{\hbar}\sqrt{8E_J E_C} \;-\; \frac{E_C}{\hbar}} \tag{2.26}$$

which is the hallmark result of the transmon qubit [10–12]. The weak anharmonicity, determined by E_C, allows for selective addressing of the qubit transition while maintaining insensitivity to charge noise in the large E_J/E_C regime (typically $E_J/E_C \approx 50$). From Eq. (2.25) it is clear that the additional term causes the individual levels of the transmon to become progressively closer, i.e., to have sequentially lower transition energies. It is useful to build intuition for this behavior.

We start by analyzing what happens when the first excitation is acquired by a qubit. Consider the **ground state** ($|0\rangle$), when no energy is stored in the qubit. In this case the effective inductance of the JJ can be defined through

$$\omega_{01} = \frac{1}{\hbar}\sqrt{8E_J E_C} \;-\; \frac{E_C}{\hbar} \;=\; \frac{1}{\sqrt{L_{01}C}}. \tag{2.27}$$

Here L_{01} is the equivalent (small-signal) inductance of the JJ when the qubit is in its ground state, and $\hbar\omega_{01}$ is the first excitation energy. For this particular discussion we treat the qubit as a semiclassical nonlinear resonator. The inductance of the qubit is nonlinear and will change as energy is stored; however, because the energy of the electromagnetic mode is quantized, we may assume that the inductance remains approximately constant until the qubit is excited with one photon and reaches its first **excited state ($|1\rangle$)**. Once excited, the energy stored in the resonator oscillates between the capacitor and the JJ. When the energy is momentarily stored entirely in the JJ, the current through it is maximized. Approximating the stored energy in the JJ by

$$\frac{1}{2}L_{01}I_{\mathrm{pk}}^2 = \hbar\omega_{01} \quad \Longrightarrow \quad I_{\mathrm{pk}}^2 = \frac{2\hbar\omega_{01}}{L_{01}}, \tag{2.28}$$

where I_{pk} is the peak current through the JJ, and introducing the (small) peak phase amplitude A via $I \approx I_c\,\phi$ so that $A \equiv I_{\mathrm{pk}}/I_c$, we obtain

$$A^2 = \left(\frac{I_{\mathrm{pk}}}{I_c}\right)^2 = \frac{2\hbar\omega_{01}}{I_c^2 L_{01}}. \tag{2.29}$$

Our goal is to calculate the new inductance value of the JJ in the excited state. Once we have that value we can calculate the qubit's new frequency and subsequently estimate the anharmonicity of the qubit. Returning to the instantaneous inductance,

$$L_J(t) = \frac{\Phi_0}{2\pi I_c \cos\phi(t)} = \frac{L_{01}}{\cos\phi(t)}, \qquad \phi(t) \approx A\sin(\omega_{01}t), \tag{2.30}$$

and for small ϕ,

$$\frac{1}{\cos\phi} = 1 + \frac{\phi^2}{2} + \mathcal{O}(\phi^4). \tag{2.31}$$

Because energy is stored in the qubit, the JJ is partially saturated; as a result the effective inductance is larger than the ground-state inductance. To quantify this, consider the error functional

$$\mathrm{Err}(L) = \Big\langle \big(\Phi(t) - L\, I(t)\big)^2 \Big\rangle, \qquad \langle f \rangle = \frac{1}{T}\int_0^T f(t)\, dt, \tag{2.32}$$

and minimize it with respect to L. Setting $\partial \mathrm{Err}/\partial L = 0$ gives

$$L_{\mathrm{eq}} = \frac{\langle \Phi(t)\, I(t) \rangle}{\langle I^2(t) \rangle}, \qquad \Phi(t) = \frac{\Phi_0}{2\pi}\phi(t), \tag{2.33}$$

which provides a time-averaged linearization of the nonlinear inductance under semiclassical conditions. With $I(t) \approx I_c\big(\phi(t) - \phi^3(t)/6\big)$ and using $\langle \phi^2 \rangle = A^2/2$ and $\langle \phi^4 \rangle = 3A^4/8$ for $\phi(t) = A \sin \omega_{01} t$ [13, Sec. 3.3.29], we obtain (to $\mathcal{O}(A^2)$):

$$L_{\mathrm{eq}} = \frac{\Phi_0}{2\pi I_c} \frac{\langle \phi^2 \rangle - \frac{1}{6}\langle \phi^4 \rangle}{\langle \phi^2 \rangle - \frac{1}{3}\langle \phi^4 \rangle} = L_{01}\left[1 + \frac{1}{8}A^2 + \mathcal{O}(A^4)\right]. \tag{2.34}$$

Using L_{eq} in the new resonance frequency of the qubit gives

$$\omega_{12} = \frac{1}{\sqrt{L_{\mathrm{eq}} C}} = \omega_{01}\Big(1 + \tfrac{1}{8}A^2\Big)^{-1/2} \approx \omega_{01}\Big(1 - \tfrac{1}{16}A^2\Big), \tag{2.35}$$

where ω_{12} is the transition frequency from the first to the second excited state ($|1\rangle \to |2\rangle$). The anharmonicity is then

$$\alpha \equiv \omega_{12} - \omega_{01} \approx -\frac{\omega_{01} A^2}{16}. \tag{2.36}$$

Substituting (2.29) and (2.26) into (2.36) yields

$$\alpha \approx -\frac{E_C}{\hbar}\left(1 - \sqrt{\frac{E_C}{8E_J}}\right)^2. \tag{2.37}$$

Finally, since in the transmon regime $E_J \gg E_C$, we obtain the familiar leading-order result

$$\boxed{\alpha = -\frac{e^2}{2\hbar\, C} \equiv -\frac{E_C}{\hbar}\,,} \tag{2.38}$$

which matches the standard weakly nonlinear (Duffing) picture for the $|0\rangle \to |1\rangle$ transition [14]. Higher transitions follow similarly; for example, the next spacing satisfies $\omega_{23} = \omega_{12} - \alpha$ (see Fig. 2.3).

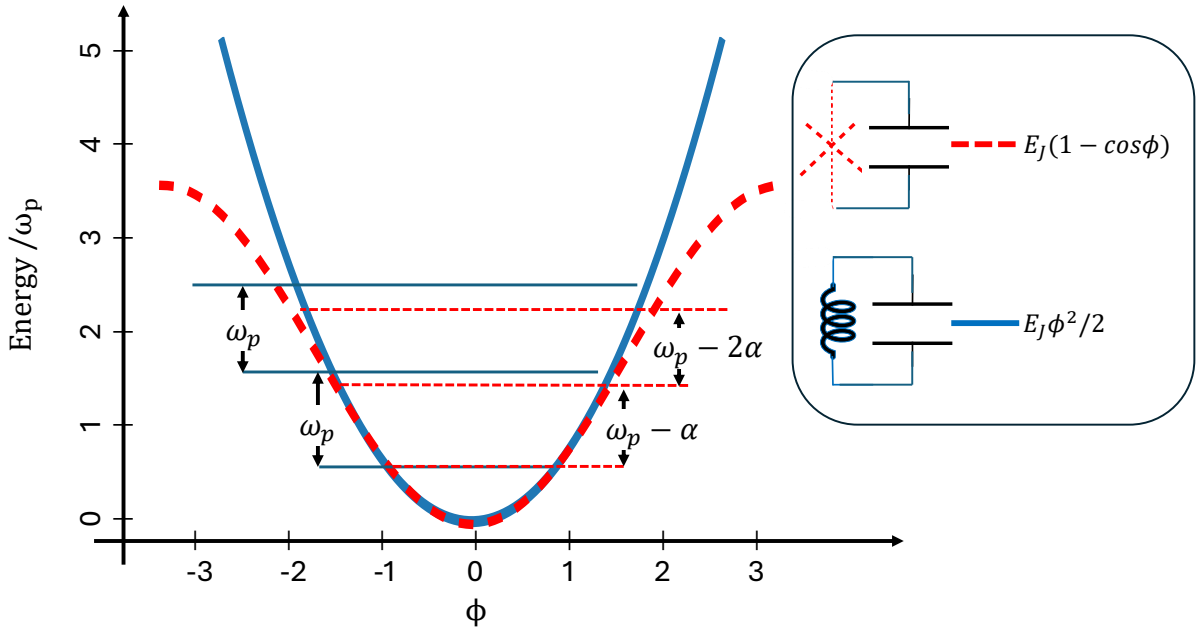

Fig. 2.3: Comparison between the simple-harmonic-oscillator (SHO) potential (solid blue) and the transmon qubit potential (dashed orange). The transmon's nonparabolic potential causes unequally spaced energy levels; the resulting anharmonicity $\alpha = \omega_{12} - \omega_{01}$ enables selective qubit control and high-fidelity measurement.

From (2.38) it is clear that parameter choice in qubit design is a balance: push E_J/E_C high enough for charge insensitivity while keeping E_C/h large enough (hundreds of MHz) to preserve control and measurement performance. Here is a worked example of how to choose

qubit parameters from a target frequency and anharmonicity. Say,

$$\frac{\omega_{01}}{2\pi} = 4.5 \text{ GHz}, \qquad \frac{|\alpha|}{2\pi} = 200 \text{ MHz}.$$

From $|\alpha| = E_C/\hbar$ we get

$$E_C/h = 0.200 \text{ GHz}, \qquad C = \frac{e^2}{2E_C} \approx 96.9 \text{ fF}. \tag{2.39}$$

Using Eq. (2.26) (neglecting the small $-E_C/\hbar$ term for a back-of-the-envelope estimate),

$$\frac{E_J}{E_C} = \frac{(\hbar\omega_{01})^2}{8E_C^2} = \frac{(hf_{01})^2}{8(hf_C)^2} = \left(\frac{f_{01}}{\sqrt{8}\, f_C}\right)^2, \tag{2.40}$$

so with $f_{01} = 4.5\,\text{GHz}$ and $f_C = 0.200\,\text{GHz}$,

$$\boxed{\frac{E_J}{E_C} \approx 63.28} \tag{2.41}$$

which automatically satisfies $\omega_{01} \gg |\alpha|$. This fixes

$$\frac{E_J}{h} = (E_J/E_C)\, f_C \approx 12.66 \text{ GHz}, \quad I_c = \frac{2eE_J}{\hbar} \approx 25.5 \text{ nA}, \quad L_{J0} = \frac{\Phi_0}{2\pi I_c} \approx 12.9 \text{ nH}.$$

What if one insists on E_J/E_C in the 50–60 range? With $E_C/h = 200\,\text{MHz}$ fixed:

$$E_J/E_C = 50 \;\Rightarrow\; f_{01} = \sqrt{8 \cdot 50}\, f_C = 4.00 \text{ GHz},$$
$$E_J/E_C = 60 \;\Rightarrow\; f_{01} = \sqrt{8 \cdot 60}\, f_C \approx 4.382 \text{ GHz}.$$

Both already satisfy $\omega_{01} \gg |\alpha|$, but they fall short of $4.5\,\text{GHz}$ at $|\alpha|/2\pi = 200\,\text{MHz}$. To

reach 4.5 GHz while keeping $E_J/E_C = 60$, solve Eq. (2.40) for f_C:

$$f_C = \frac{f_{01}}{\sqrt{8(E_J/E_C)}} = \frac{4.5}{\sqrt{480}}\ \text{GHz} \approx 205.4\ \text{MHz},$$

i.e., a slightly larger E_C/h (and hence slightly larger $|\alpha|$). Conversely, keeping $E_J/E_C = 50$ would require $f_C = 225\,\text{MHz}$ to hit 4.5 GHz.

The main takeaway is that for charge insensitivity one must ensure $E_J \gg E_C$. You can approach this by increasing E_J or by decreasing E_C; only the former preserves $|\alpha|$, whereas the latter reduces it. The numerical example above quantifies the trade-off: $f_{01} = 4.5\,\text{GHz}$ and $|\alpha|/2\pi = 200\,\text{MHz}$ imply $E_J/E_C \approx 63.3$ (with $C \approx 97\,\text{fF}$, $I_c \approx 25.5\,\text{nA}$). Ratios in the 50–60 range already yield $\omega_{01} \gg |\alpha|$, but at fixed E_C they produce $f_{01} \approx 4.0$–$4.38\,\text{GHz}$; reaching 4.5 GHz at those ratios requires a modest increase of E_C (and therefore $|\alpha|$).

2.3 Surrounding elements of a qubit and basic gates

A stand-alone qubit in an ideal world could store quantum information indefinitely. However, a floating (fully isolated) qubit is useless in practice because we can neither excite it nor read out its state. To make a qubit usable, several auxiliary elements must be coupled to it. Typical examples include a *readout resonator*, a *fast flux line*, and an XY drive line. A layout of a representative device is shown in Fig. 2.4(a), and an equivalent circuit schematic is shown in Fig. 2.4(b). We will study each component that is added, in detail, and explain how it enables control and/or readout of the qubit state.

Before analyzing individual elements, it is essential to understand their *collective* effect. Each component coupled to the qubit introduces a pathway for energy to leak into the environment, i.e., a loss channel. By quantifying the individual and cumulative loss induced

by these components, we can choose the coupling strengths between the qubit and each element in a principled way.

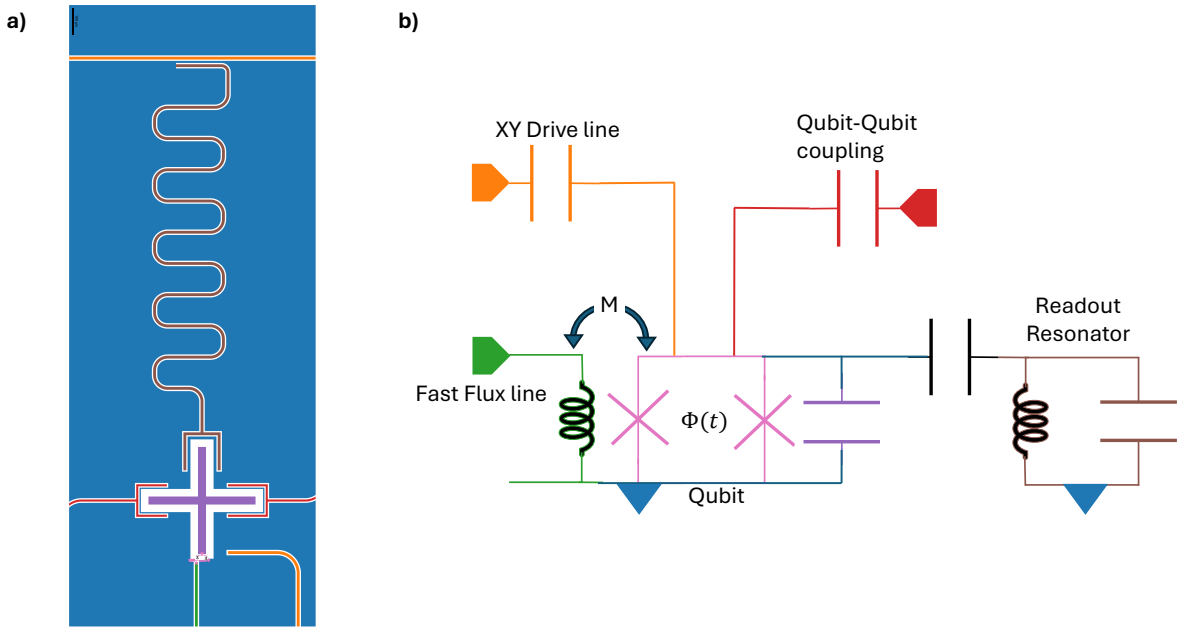

Fig. 2.4: Representative superconducting qubit and its immediate environment. **(a)** Device layout highlighting the qubit island with Josephson junction(s), large shunt capacitor, dedicated XY drive line for transverse control, fast flux line for (near-)DC/low-frequency frequency tuning, and a capacitively coupled readout resonator connected to a feedline. **(b)** Lumped-element circuit model used for analysis and simulation, showing the qubit (effective $L_J \parallel C_Q$) in parallel with the admittances contributed by the attached control and readout ports. The couplings determine both controllability and the Purcell-limited T_1.

2.3.1 Purcell Loss

To analyze the net loss induced by each coupled structure (fast flux line, XY drive, readout resonator + feedline, nearest-neighbour coupler), we reduce the overall network in Fig. 2.4(b) to its Thevenin/Norton equivalent *as seen at the qubit port* and *evaluated at the qubit tran-*

sition frequency ω_q [5, 15]. The environment is then described by an input admittance

$$Y_{\text{in}}(\omega_q) = \Re Y_{\text{in}}(\omega_q) + i\,\Im Y_{\text{in}}(\omega_q), \tag{2.42}$$

placed *in parallel* with the qubit's linearized elements (Josephson inductance L_J in parallel with total shunt capacitance C_Q). Near resonance, we transform to a frame rotating at (or close to) ω_q. In this frame, the slowly varying voltage envelope across the junction and capacitor is insensitive to the reactive load $\Im Y_{\text{in}}$, which produces only a small frequency pull (Lamb/Purcell shift) but no dissipation [5]. For the *purely lossy* envelope dynamics we therefore keep only

$$\Re Y_{\text{in}}(\omega_q) \equiv G_{\text{in}} \quad \text{and neglect} \quad \Im Y_{\text{in}}.$$

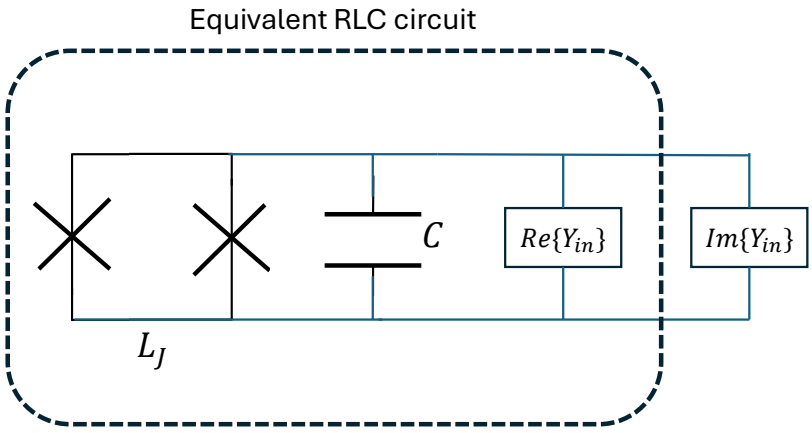

Fig. 2.5: Effective qubit network and input admittance. The port-reduced environment seen by the qubit is captured by an effective admittance $Y_{\text{in}}(\omega)$ placed in parallel with $L_J \parallel C_Q$. Its *real* part at ω_q sets the Purcell-limited energy-relaxation rate via Eqs. (2.44)–(2.45); the *imaginary* part gives a small frequency shift.

2.3.2 Purcell Loss

For the envelope description, the parallel network reduces to an effective parallel RLC (Fig. 2.5) with a conductance G_{in} shunting the qubit capacitor and inductor. Applying Kirchhoff's Current Law (KCL) at the qubit node for the envelope voltage $v(t)$,

$$C_Q \frac{dv}{dt} + G_{\text{in}}\, v(t) \simeq 0, \tag{2.43}$$

whose solution is $v(t) \propto e^{-t/T_1}$ with the parallel-RC time constant

$$T_1 = \frac{C_Q}{G_{\text{in}}} = \frac{C_Q}{\Re Y_{\text{in}}(\omega_q)}. \tag{2.44}$$

Equivalently, the energy decay rate is

$$\Gamma_1 \equiv \frac{1}{T_1} = \frac{\Re Y_{\text{in}}(\omega_q)}{C_Q}. \tag{2.45}$$

This matches the power/energy argument: the time-averaged power lost into the bath is $P = \frac{1}{2}|V|^2 \Re Y_{\text{in}}$, while the stored energy is $U = \frac{1}{2} C_Q |V|^2$, hence $P/U = \Gamma_1$ [5, 15]. Since admittances add in parallel,

$$\Re Y_{\text{in}}(\omega_q) = \sum_p \Re Y_p(\omega_q) \quad \Longrightarrow \quad \Gamma_1 = \frac{1}{C_Q} \sum_p \Re Y_p(\omega_q), \tag{2.46}$$

where $p \in \{\text{flux}, XY, \text{RO+line}, \text{coupler(s)}\}$. Each $\Re Y_p$ can be (i) extracted from EM simulation at the qubit port or (ii) obtained from compact models; for example, a dispersively coupled readout resonator of linewidth κ_r yields the familiar Purcell channel $\Gamma_{\text{Purcell}} \approx (g/\Delta)^2 \kappa_r$ [5, 16].

The value in (2.44) computed from $\Re Y_{\text{in}}$ represents the *best possible* relaxation time set

by external coupling in the given layout (a design-level ceiling). Real devices also suffer from intrinsic mechanisms—quasiparticles, dielectric loss and two-level systems (TLS), surface/interface losses, radiation from seams and packaging, etc. [17, 18]. These add *rates*, so that

$$\frac{1}{T_{1,\text{tot}}} = \underbrace{\frac{\Re Y_{\text{in}}(\omega_q)}{C_Q}}_{\text{Purcell/external}} + \underbrace{\frac{1}{T_{1,\text{intrinsic}}}}_{\text{materials \& defects}} \quad \Longrightarrow \quad T_{1,\text{tot}} \leq T_1\big|_{\Re Y_{\text{in}}}, \tag{2.47}$$

which cleanly separates *engineered* coupling (set by layout and port impedances) from *materials-limited* decoherence. This analysis quantifies the overall loss added by the measurement and control structures surrounding the qubit. In what follows, we study how both energy decay and phase decoherence affect the qubit state.

2.3.3 Decoherence in qubit state

A general state of a two-level quantum system (qubit) can be expressed in the computational basis $\{|g\rangle, |e\rangle\}$ as

$$|\psi\rangle = \alpha|g\rangle + \beta|e\rangle, \tag{2.48}$$

where $\alpha, \beta \in \mathbb{C}$ are complex probability amplitudes that satisfy the normalization condition

$$|\alpha|^2 + |\beta|^2 = 1. \tag{2.49}$$

Since quantum states are defined up to a global phase, we may factor out a phase $e^{i\phi}$ from both α and β without affecting physical predictions. By doing so, one can always choose a representation where either α or β is real. This gauge freedom reduces the number of independent parameters needed to describe a qubit state from four real numbers (two complex amplitudes) to three. Thus, a full qubit state requires three real parameters for its

description. For a pure qubit state, the density matrix is given by the outer product

$$\rho = |\psi\rangle\langle\psi| = \begin{bmatrix} |\alpha|^2 & \alpha\beta^* \\ \alpha^*\beta & |\beta|^2 \end{bmatrix}. \tag{2.50}$$

Here, the *diagonal* entries encode populations and the *off-diagonal* entries encode phase coherence. This density operator is Hermitian, positive semi-definite, and satisfies $\mathrm{Tr}(\rho) = 1$. The condition for a pure state is $\rho^2 = \rho$.

To connect populations with energy relaxation, note first that amplitude damping transfers population from $|e\rangle$ to $|g\rangle$ with characteristic time T_1. For zero-temperature relaxation, the excited-state population decays exponentially,

$$\rho_{ee}(t) = \rho_{ee}(0)\, e^{-t/T_1}, \qquad \rho_{gg}(t) = 1 - \rho_{ee}(t), \tag{2.51}$$

and the coherence also acquires a relaxation-induced factor (see below). Correspondingly, the state's *purity* $\mathcal{P}(t) = \mathrm{Tr}\,\rho^2(t)$ decreases as the phase becomes mixed and the system thermalizes to the noisy environment, but eventually increases again because energy relaxation drives the qubit toward its ground state.

By contrast, the off-diagonal elements ρ_{ge} quantify phase coherence. Under amplitude damping alone,

$$\rho_{ge}(t) = \rho_{ge}(0)\, e^{-t/(2T_1)}. \tag{2.52}$$

Additional phase randomization (pure dephasing) multiplies this by $e^{-\Gamma_\phi t}$ when the noise is effectively white around zero frequency, giving

$$\rho_{ge}(t) \;=\; \rho_{ge}(0)\, \exp\!\left[-\frac{t}{2T_1} - \Gamma_\phi t\right], \qquad \frac{1}{T_2} \;=\; \frac{1}{2T_1} + \Gamma_\phi. \tag{2.53}$$

Here Γ_ϕ is set by fluctuations of the transition frequency $\omega_q(t) = \omega_q + \delta\omega(t)$.

2.3.4 Dispersive Qubit Readout

When a qubit is prepared in its excited state, the transition structure is altered by its anharmonicity. This shift can be detected using classical microwave measurement techniques. Although the excitation stored in a superconducting qubit can be described in terms of a photon, the large anharmonicity renders the energy levels non-degenerate, allowing us to model the qubit as an effective two-level system. In the absence of any other coupling, the qubit is described by

$$\hat{H}_{\mathrm{q}} = \frac{\hbar\omega_q}{2}\hat{\sigma}_z, \tag{2.54}$$

where ω_q is the qubit transition frequency and $\hat{\sigma}_z$ is the Pauli-z operator.

Direct scattering-type measurements of the qubit would irreversibly collapse the quantum state after a single measurement, making them unsuitable for repeated or high-fidelity experiments. To avoid this, *quantum non-demolition* (QND) measurement schemes are employed. In such a scheme, the qubit is dispersively coupled to a linear microwave resonator or cavity (Fig. 2.6), which can be probed without directly affecting the qubit. Because the cavity is coupled to the qubit, the two form a composite system described by the Jaynes–Cummings Hamiltonian:

$$\hat{H} = \hbar\omega_c\,\hat{a}^\dagger\hat{a} + \frac{\hbar\omega_q}{2}\,\hat{\sigma}_z + \hbar g\left(\hat{a}^\dagger\hat{\sigma}_- + \hat{a}\hat{\sigma}_+\right), \tag{2.55}$$

where ω_c is the resonator frequency, $\hat{a}^\dagger$ and $\hat{a}$ are bosonic creation and annihilation operators for the resonator mode, $\hat{\sigma}_\pm$ are the qubit raising and lowering operators, and g is the qubit–resonator coupling rate [19, 20].

In the dispersive regime, where the detuning $|\Delta| = |\omega_q - \omega_c| \gg g$, a Schrieffer–Wolff transformation can be applied to Eq. (2.55) to eliminate the energy-exchange terms to leading

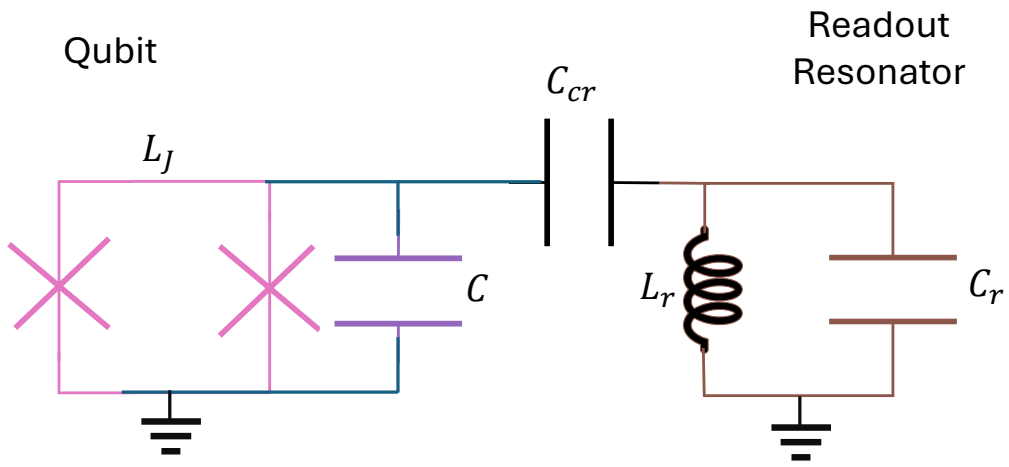

Fig. 2.6: Dispersive readout. A linear readout resonator (frequency ω_c, linewidth κ) is dispersively coupled to the qubit. Probing the resonator near ω_c maps the qubit state onto a state-dependent cavity frequency shift ($\pm\chi$), enabling QND readout via homodyne or heterodyne detection without directly exciting the qubit.

order. The resulting effective Hamiltonian is

$$\hat{H}_{\text{disp}} \approx \hbar\,(\omega_c + \chi\,\hat{\sigma}_z)\,\hat{a}^\dagger\hat{a} + \frac{\hbar}{2}\,(\omega_q + \chi)\,\hat{\sigma}_z, \tag{2.56}$$

where χ is the *dispersive shift*. For an idealized two-level qubit, the dispersive shift is

$$\chi = \frac{g^2}{\Delta}, \tag{2.57}$$

while for a weakly anharmonic qubit, such as a transmon with anharmonicity $\alpha \equiv \omega_{12} - \omega_{01} \approx -E_C/\hbar$, the more accurate expression is [10, 21]:

$$\chi \approx -\frac{g^2\alpha}{\Delta(\Delta+\alpha)}. \tag{2.58}$$

In the limit $|\alpha| \ll |\Delta|$, Eq. (2.58) reduces to the two-level result in Eq. (2.57).

To build intuition for Eq. (2.56), notice first that the resonator frequency is shifted by $\pm\chi$ depending on whether the qubit is in $|g\rangle$ or $|e\rangle$; conversely, the qubit frequency experiences an ac Stark shift proportional to the average photon number in the resonator. This state-dependent cavity frequency enables QND readout: by driving the cavity near $\omega_c \pm \chi$ and measuring the phase or amplitude of the transmitted signal, the qubit state can be inferred without directly exciting it. The magnitude of χ determines both the measurement signal-to-noise ratio (SNR) and the measurement-induced dephasing rate [21]. A larger $|\chi|$ improves the separation of pointer states in phase space (faster, higher-fidelity readout) but also increases backaction on the qubit; thus, χ must be engineered to balance readout speed and fidelity against preservation of coherence.

To make this more concrete, recall that a resonator with linewidth κ has a photon lifetime $\tau_{\text{cav}} = 1/\kappa$, which characterizes how long, on average, a photon remains stored before leaking out. The closer a probe tone is to ω_c, the longer photons dwell in the cavity and the larger the intracavity field amplitude becomes for a given drive power. Quantitatively, the Lorentzian response

$$|\eta(\omega)|^2 \propto \frac{1}{(\omega - \omega_c)^2 + (\kappa/2)^2} \tag{2.59}$$

shows that the stored energy—and hence effective delay—peaks sharply at resonance.

Next, view the qubit–cavity pair as two weakly coupled oscillators: in the dispersive regime ($|\Delta| \gg g$), the normal modes are only slightly hybridized and repel each other in frequency space. If $\omega_q < \omega_c$, the dressed qubit frequency shifts slightly downward while the cavity shifts upward, consistent with the perturbative result $\chi = g^2/\Delta$ [19]. When the qubit is excited, its transition structure (through α) produces a corresponding state-dependent dispersive pull on the cavity frequency—this is the operational heart of the readout scheme.

Furthermore, if the cavity is driven to an average intracavity photon number $\bar{n} = \langle \hat{a}^\dagger \hat{a} \rangle$, the dispersive Hamiltonian predicts a qubit Stark shift $\delta\omega_q = 2\chi\,\bar{n}$. Coherent photons exhibit Poissonian statistics, so the instantaneous photon number fluctuates with variance $\Delta n^2 = \bar{n}$. These fluctuations induce stochastic shifts of the qubit frequency, which lead to *measurement-induced dephasing*. More precisely, the qubit dephasing rate due to photon shot noise is given by [21]

$$\Gamma_\phi^{\text{meas}} \approx 8\chi^2 \frac{\bar{n}}{\kappa}, \tag{2.60}$$

where κ is the cavity decay rate, reflecting the fact that the qubit integrates photon number fluctuations over the cavity lifetime. High-fidelity measurement therefore requires a balance: one must use enough photons to separate the cavity pointer states quickly, but not so many that photon shot-noise-induced dephasing significantly reduces the qubit coherence during the readout.

Finally, to connect with the Purcell channel in the input-admittance picture: for a qubit coupled through a small capacitor C_{cr} to a readout resonator (frequency ω_c, linewidth κ), the environment seen at the qubit port is the resonator plus its feedline. Linearizing, the resonator's effective admittance at the coupling node is

$$Y_{\text{res}}(\omega) \;\approx\; \frac{\kappa/2}{i(\omega_c - \omega) + \kappa/2}, \tag{2.61}$$

up to an overall scale set by the resonator impedance. The series coupling capacitor transforms this to the qubit port as

$$Y_{\text{in}}(\omega) \;\approx\; \omega^2 C_{cr}^2 \,\frac{\kappa/2}{(\omega_c - \omega)i + \kappa/2}. \tag{2.62}$$

Taking the real part at $\omega = \omega_q$ gives

$$\Re\{Y_{\text{in}}(\omega_q)\} \;\approx\; \omega_q^2 C_{cr}^2 \,\frac{\kappa}{(\omega_q - \omega_c)^2 + (\kappa/2)^2}. \tag{2.63}$$

Substituting (2.63) into (2.45) yields the Purcell-limited relaxation rate in the Thevenin picture:

$$\Gamma_1^{\text{Purcell}} \;=\; \frac{\Re\{Y_{\text{in}}(\omega_q)\}}{C_Q} \;\approx\; \frac{C_{cr}^2}{C_Q}\,\omega_q^2\,\frac{\kappa}{(\omega_q - \omega_c)^2 + (\kappa/2)^2}. \tag{2.64}$$

In the large-detuning (dispersive) limit, the term $(\kappa/2)^2$ in the denominator can be neglected, and the rate reduces to

$$\Gamma_1^{\text{Purcell}} \;\simeq\; \left(\frac{g}{\Delta}\right)^2 \kappa, \qquad \Delta = \omega_q - \omega_c, \tag{2.65}$$

upon identifying the coupling g in terms of circuit parameters (C_{cr}, mode impedances, and zero-point voltages) [10, 16, 22]. Equation (2.64) is particularly convenient for *arbitrary* environments: once $Y_{\text{in}}(\omega)$ is computed (analytically or via EM simulation), the Purcell rate follows from Eq. (2.45). In practice, the cavity-induced Purcell limit can be mitigated—and often nearly eliminated—by inserting *Purcell filters* that strongly suppress transmission at the qubit frequency while maintaining a passband around the readout resonator frequency. Engineering the environment so that $\Re\{Y_{\text{in}}(\omega_q)\} \approx 0$ suppresses Purcell loss without sacrificing measurement bandwidth near ω_c. We will discuss specific Purcell-filter realizations in the design chapter of this thesis.

2.3.5 Fast Flux line

A fast flux line delivers a controlled magnetic flux to a SQUID loop to tune a qubit's frequency on ns–μs timescales. In a standard tunable transmon, the Josephson element

is a dc SQUID—two Josephson junctions (JJs) in parallel, forming a loop threaded by an external flux Φ. The flux dependence of the SQUID's effective Josephson energy $E_{J,\mathrm{eff}}(\Phi)$ sets the qubit frequency $\omega_q(\Phi)$, enabling both static tuning and time-dependent (parametric) modulation for gates.

We firsst consider a symmetric SQUID with negligible loop inductance which consists of two identical junctions with critical current I_c and Josephson energy $E_J = \Phi_0 I_c/2\pi$ ($\Phi_0 = h/2e$). Let the junction phases be φ_1 and φ_2, with the fluxoid constraint

$$\varphi_1 - \varphi_2 = 2\pi \frac{\Phi}{\Phi_0} \equiv 2\delta, \qquad \delta \equiv \pi \frac{\Phi}{\Phi_0}. \tag{2.66}$$

Defining the average phase $\varphi \equiv (\varphi_1 + \varphi_2)/2$, the Josephson potential reduces to

$$U_J(\varphi, \Phi) = -2E_J \cos(\delta)\, \cos(\varphi). \tag{2.67}$$

Thus the SQUID behaves like a single effective junction with flux-tunable energy

$$E_{J,\mathrm{eff}}(\Phi) = 2E_J \cos(\delta), \qquad I_{c,\mathrm{eff}}(\Phi) = 2I_c \cos(\delta). \tag{2.68}$$

Linearizing about the minimum, the small-signal Josephson inductance is

$$L_{J,\mathrm{SQ}}(\Phi) = \frac{\Phi_0}{2\pi\, I_{c,\mathrm{eff}}(\Phi)} = \frac{\Phi_0}{4\pi\, I_c \cos(\pi\Phi/\Phi_0)}. \tag{2.69}$$

Now in an asymmetric SQUID with negligible loop inductance. If the junctions have unequal critical currents $I_{c1} \neq I_{c2}$ but the loop inductance is negligible, set

$$\varphi_1 = \varphi + \delta, \qquad \varphi_2 = \varphi - \delta.$$

The total current is

$$\begin{aligned} I(\varphi, \Phi) &= I_{c1} \sin(\varphi + \delta) + I_{c2} \sin(\varphi - \delta) \\ &= (I_{c1} + I_{c2}) \sin\varphi \cos\delta + (I_{c1} - I_{c2}) \cos\varphi \sin\delta. \end{aligned} \tag{2.70}$$

This can be written as

$$I = I_{c,\text{eff}}(\Phi)\ \sin(\varphi + \varphi_0), \tag{2.71}$$

with

$$\begin{aligned} I_{c,\text{eff}}(\Phi) &= \sqrt{\big[(I_{c1} + I_{c2}) \cos\delta\big]^2 + \big[(I_{c1} - I_{c2}) \sin\delta\big]^2} \\ &= \sqrt{I_{c1}^2 + I_{c2}^2 + 2I_{c1}I_{c2} \cos\Big(2\pi \frac{\Phi}{\Phi_0}\Big)}. \end{aligned} \tag{2.72}$$

The corresponding small-signal inductance is

$$L_{J,\text{SQ}}(\Phi) = \frac{\Phi_0}{2\pi\, I_{c,\text{eff}}(\Phi)}. \tag{2.73}$$

For convenience, define the asymmetry parameter $d = (I_{c1} - I_{c2})/(I_{c1} + I_{c2})$ and average critical current $I_c = (I_{c1} + I_{c2})/2$. Then

$$I_{c,\text{eff}}(\Phi) = 2I_c \sqrt{\cos^2\delta + d^2 \sin^2\delta}, \qquad L_{J,\text{SQ}}(\Phi) = \frac{\Phi_0}{4\pi I_c} \frac{1}{\sqrt{\cos^2\delta + d^2 \sin^2\delta}}, \tag{2.74}$$

which recovers Eq. (2.69) for the symmetric case $d = 0$.

For a transmon-like mode with capacitance C_Σ and charging energy $E_C = e^2/2C_\Sigma$, the

qubit transition frequency inherits the tunability of $E_{J,\mathrm{eff}}(\Phi)$:

$$\omega_{01}(\Phi) \approx \frac{1}{\hbar}\Big(\sqrt{8E_{J,\mathrm{eff}}(\Phi)E_C} - E_C\Big), \tag{2.75}$$

valid in the transmon regime $E_{J,\mathrm{eff}} \gg E_C$ [10].

A fast flux line with mutual inductance M to the SQUID loop delivers a flux

$$\Phi(t) = \Phi_{\mathrm{dc}} + M\, I_{\mathrm{ff}}(t), \tag{2.76}$$

allowing both static biasing (Φ_{dc}) and time-dependent modulation $I_{\mathrm{ff}}(t)$. The mutual inductance value must be chosen to strike a practical balance: it should be large enough that a reasonable current in the flux line can tune the qubit over a useful range (ideally approaching a flux quantum Φ_0 with comfortable current margins), yet not so large that the qubit decays through the flux line and dissipate in to the 50 Ω environment.

2.3.6 Qubit-qubit coupling

Up to this point we have discussed various mechanisms for *single-qubit* operations. However, to realize a useful quantum processor we ultimately require a large-scale system containing thousands of qubits, not only with individual addressability but also with the ability to generate *entanglement* between them. In superconducting architectures, the prevailing approach is to arrange qubits in a two-dimensional (2D) lattice geometry, where each qubit interacts only with its nearest neighbors [5, 20, 23, 24]. Such nearest-neighbor connectivity is natural to planar lithographic layouts and provides a balance between hardware scalability and gate fidelity.

There exist multiple physical mechanisms to induce qubit–qubit interactions on this

platform. In this section we introduce some of the canonical approaches, beginning with the simplest case of direct frequency tuning.

2.3.6.1 Direct resonant coupling

The most direct way to couple two superconducting qubits is via a static capacitance or inductance (see Fig. 2.7(a)) between their circuit nodes. This results in an *exchange-type* interaction of the form

$$H = \frac{\hbar\omega_1}{2}\,\sigma_z^{(1)} + \frac{\hbar\omega_2}{2}\,\sigma_z^{(2)} + \hbar g\big(\sigma_+^{(1)}\sigma_-^{(2)} + \sigma_-^{(1)}\sigma_+^{(2)}\big), \tag{2.77}$$

where qubit 1 and qubit 2 have transition frequencies ω_1 and ω_2, and g is the coupling rate determined by the shared capacitance/inductance [5, 10]. Here σ_z denotes the Pauli-z operator and $\sigma_\pm$ the qubit raising/lowering operators.

When the two qubits are brought into resonance ($\omega_1 \approx \omega_2$), the exchange term mediates coherent population transfer between the states $|10\rangle$ and $|01\rangle$ at the Rabi frequency $2g$. This is the hallmark of the so-called *swap* interaction:

$$|10\rangle \;\leftrightarrow\; |01\rangle\,, \qquad \text{oscillating at rate } 2g. \tag{2.78}$$

In practice, one of the qubits (say qubit 2) is fabricated as a tunable transmon (SQUID-based) while the other (qubit 1) remains at fixed frequency. By applying a calibrated dc flux pulse to the tunable qubit, its frequency ω_2 can be shifted into resonance with ω_1. While this detuning condition ($\delta = |\omega_2 - \omega_1| = 0$) is maintained, the Hamiltonian in Eq. (2.77) drives coherent population exchange, observable as oscillations in qubit 2's excitation probability (see Fig. 2.7(d)) if qubit 1 was in the excited state prior to applying the DC bias. This

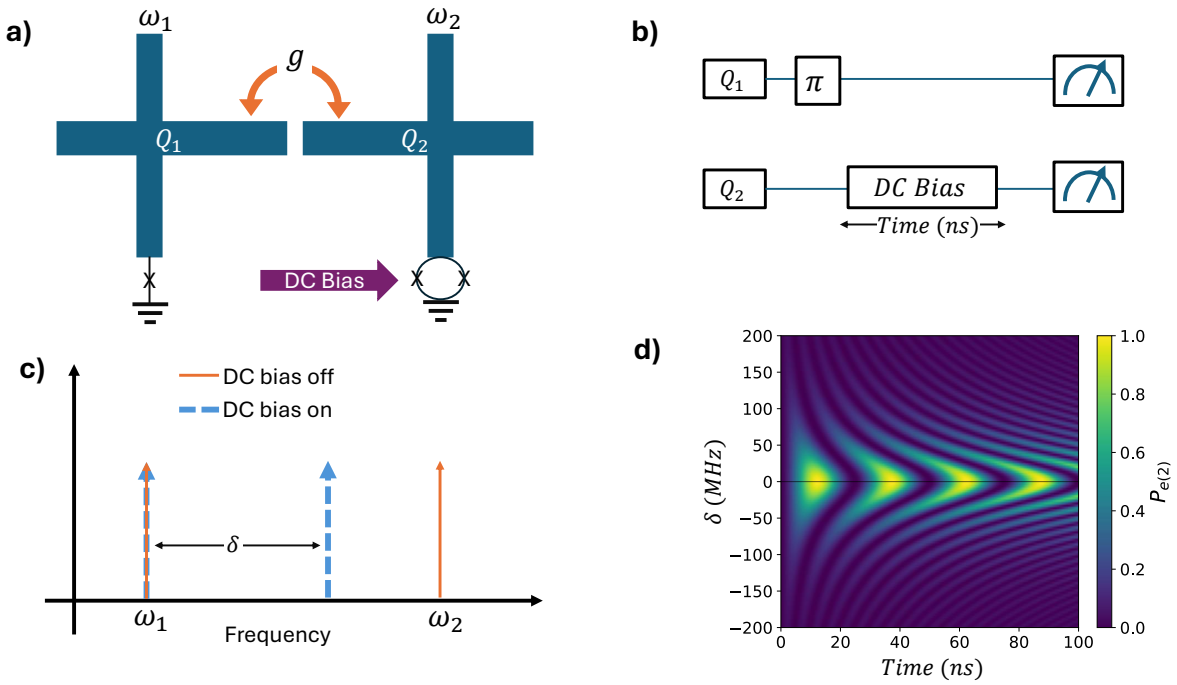

Fig. 2.7: Direct qubit–qubit coupling. **(a)** Two qubits coupled by a fixed capacitance/inductance; qubit 1 is fixed frequency ω_1, qubit 2 is flux-tunable $\omega_2(\Phi)$. **(b)** Gate sequence: bring qubits into resonance to activate exchange for a calibrated dwell time. **(c)** Spectroscopy illustrating the on/off resonance condition via DC flux bias. **(d)** Coherent population oscillations of qubit 2 when $\delta = \omega_2 - \omega_1 = 0$, evidencing excitation exchange; timing to half a period implements $\sqrt{\text{iSWAP}}$.

interaction can be harnessed to implement gates such as $\sqrt{\text{iSWAP}}$ by timing the evolution to half a swap period.

Direct resonant coupling is the *simplest* way to entangle two qubits: it makes use of the full bare coupling strength g without suppression factors, thus enabling fast gates. However, there are trade-offs. When the qubits are parked far detuned in their idle states (to suppress residual interaction), the tunable qubit must be pulsed deep into a flux-sensitive regime during gate activation. This can introduce additional dephasing errors from flux noise and reduce overall gate fidelity [20, 23]. Moreover, the always-on nature of the physical coupling means that crosstalk and frequency-collision issues must be carefully mitigated by frequency

allocation and control calibration [5].

2.3.6.2 Parametric coupling

A *parametric* coupling works exactly as the name implies: we keep the coupled qubits parked at (or near) frequency sweet spots and drive the tunable qubit with a parametric flux modulation to activate qubit–qubit exchange. We consider two coupled qubits similar to the last case; the only difference is that qubit 2's frequency is modulated using an external pump (Fig. 2.8(a)). The tunability of qubit 2 follows the standard SQUID/transmon law [10]. Below we (i) expand the time-dependent qubit frequency in a Taylor series about the DC flux, (ii) write the Hamiltonian, (iii) move to the interaction picture, and (iv) derive the sideband conditions and effective coupling in the two relevant operating regimes. Let the tunable qubit frequency be

$$\omega_2(\phi) = \omega_0 \sqrt{\cos\left(\frac{\pi\phi}{\Phi_0}\right)}, \qquad \phi(t) = \phi_{\mathrm{DC}} + A\cos(\omega_p t), \quad \omega_p = 2\pi f_p, \tag{2.79}$$

where Φ_0 is the flux quantum, ω_0 is a device constant set by circuit energies, and ϕ_{DC} is the static bias. Define $\theta := \pi\phi/\Phi_0$ and $a := \pi\phi_{\mathrm{DC}}/\Phi_0$. With $f(\phi) := \omega_2(\phi) = \omega_0\sqrt{\cos\theta}$, the first two derivatives are

$$\frac{\partial\omega_2}{\partial\phi} = f'(\phi) = -\frac{\omega_0\pi}{2\Phi_0}\,\frac{\sin\theta}{\sqrt{\cos\theta}}, \tag{2.80}$$

$$\frac{\partial^2\omega_2}{\partial\phi^2} = f''(\phi) = -\frac{\omega_0}{2}\left(\frac{\pi}{\Phi_0}\right)^2\left[\sqrt{\cos\theta} + \frac{\sin^2\theta}{2(\cos\theta)^{3/2}}\right]. \tag{2.81}$$

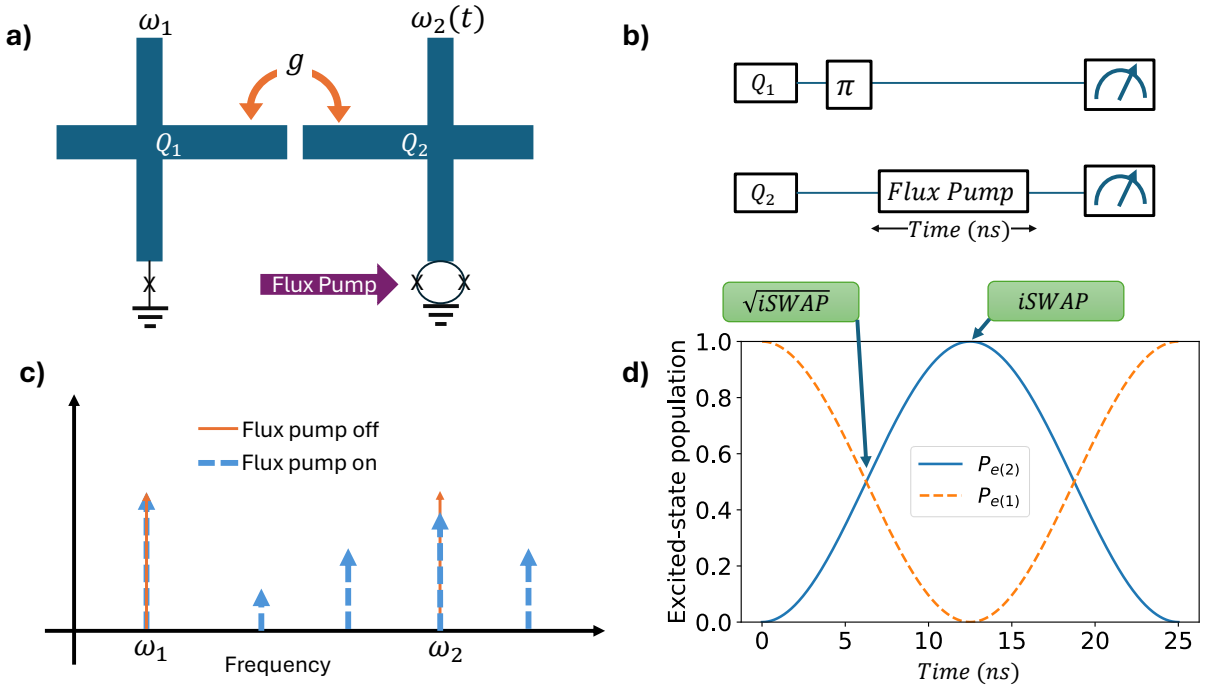

Fig. 2.8: Parametric two-qubit coupling. **(a)** Two qubits with fixed coupling; qubit 2 is flux-modulated at ω_p. **(b)** Gate sequence: apply a calibrated flux pump to activate exchange only during the pulse. **(c)** Spectroscopy with pump off/on: modulation of ω_2 produces sidebands whose resonance condition follows Eq. (2.91) (sweet spot) or Eq. (2.96) (generic bias). **(d)** Population exchange vs. time when the sideband is tuned into resonance; a full swap implements iSWAP, while half the time implements $\sqrt{\text{iSWAP}}$.

Expanding about ϕ_{DC} with $\delta\phi(t) = A\cos(\omega_p t)$ gives, to $\mathcal{O}(A^2)$,

$$\begin{aligned}\omega_2(t) &= f(\phi_{\text{DC}}) + f'(\phi_{\text{DC}})\,\delta\phi(t) + \frac{1}{2}f''(\phi_{\text{DC}})\,\delta\phi(t)^2 + \mathcal{O}(A^3) \\ &= \underbrace{f(\phi_{\text{DC}}) + \frac{A^2}{4}f''(\phi_{\text{DC}})}_{\omega_2^{\text{DC}}} + \underbrace{A\,f'(\phi_{\text{DC}})}_{\varepsilon_1}\cos(\omega_p t) + \underbrace{\frac{A^2}{4}f''(\phi_{\text{DC}})}_{\varepsilon_2}\cos(2\omega_p t) + \mathcal{O}(A^3).\end{aligned} \tag{2.82}$$

Thus the modulation produces a DC shift ω_2^{DC}, a fundamental tone with amplitude ε_1, and a second harmonic with amplitude ε_2.

Sweet spot vs. generic bias. At a *flux sweet spot* ($\sin a = 0$), $f'(\phi_{\mathrm{DC}}) = 0$ so the fundamental vanishes and the leading tone is at $2\omega_p$ (via curvature f''). Away from a sweet spot ($\sin a \neq 0$), both the ω_p and $2\omega_p$ components appear, with the fundamental scaling $\propto A$ and the second harmonic $\propto A^2$.

We use an isotropic XY (exchange) interaction, keeping only flip–flop terms in the single-excitation manifold:

$$\frac{H(t)}{\hbar} = \frac{\omega_1}{2}\,\sigma_z^{(1)} + \frac{\omega_2(t)}{2}\,\sigma_z^{(2)} + g\left(\sigma_1^+\sigma_2^- + \sigma_1^-\sigma_2^+\right). \tag{2.83}$$

Split $H(t) = H_0(t) + V$ with $H_0(t) = \frac{\hbar}{2}[\omega_1\sigma_z^{(1)} + \omega_2(t)\sigma_z^{(2)}]$ and $V = \hbar g(\sigma_1^+\sigma_2^- + \sigma_1^-\sigma_2^+)$. Since $[H_0(t), H_0(t')] = 0$, the interaction-picture propagator is

$$U_0(t) = \exp\left[-\frac{i}{2}\omega_1 t\,\sigma_z^{(1)}\right]\exp\left[-\frac{i}{2}\Theta_2(t)\,\sigma_z^{(2)}\right], \qquad \Theta_2(t) := \int_0^t \omega_2(\tau)\,d\tau. \tag{2.84}$$

Using $e^{\lambda\sigma_z}\sigma_\pm e^{-\lambda\sigma_z} = e^{\pm 2\lambda}\sigma_\pm$,

$$U_0^\dagger\sigma_1^+U_0 = \sigma_1^+e^{+i\omega_1 t}, \qquad U_0^\dagger\sigma_2^-U_0 = \sigma_2^-e^{-i\Theta_2(t)}. \tag{2.85}$$

Hence the interaction-picture Hamiltonian is

$$\frac{H_I(t)}{\hbar} = g\big(\sigma_1^+\sigma_2^-\,e^{-i\phi(t)} + \sigma_1^-\sigma_2^+\,e^{+i\phi(t)}\big), \qquad \phi(t) := \int_0^t \delta(\tau)\,d\tau, \tag{2.86}$$

with instantaneous detuning (using the convention $\delta = \omega_1 - \omega_2$)

$$\delta(t) = \delta_0 - \varepsilon_1 \cos(\omega_p t) - \varepsilon_2 \cos(2\omega_p t) + \cdots, \qquad \delta_0 := \omega_1 - \omega_2^{\mathrm{DC}}. \tag{2.87}$$

Integrating term by term yields a *phase-modulated* exchange,

$$\phi(t) = \delta_0 t - \beta_1 \sin(\omega_p t) - \beta_2 \sin(2\omega_p t) - \cdots, \qquad \beta_1 := \frac{\varepsilon_1}{\omega_p}, \quad \beta_2 := \frac{\varepsilon_2}{2\omega_p}. \tag{2.88}$$

Two operating regimes: zero vs. nonzero DC bias *Zero DC flux bias (sweet spot; "two-photon" activation)* Set $\sin a = 0$ (e.g. $a = 0$). Then $f'(\phi_{\mathrm{DC}}) = 0$ and, from (2.80)–(2.81),

$$\varepsilon_1 = 0, \qquad \varepsilon_2 = \frac{A^2}{4} f''(\phi_{\mathrm{DC}}) = -\frac{\omega_0}{8}\left(\frac{\pi A}{\Phi_0}\right)^2, \qquad \delta_0 = (\omega_1 - \omega_0) + \frac{\omega_0}{8}\left(\frac{\pi A}{\Phi_0}\right)^2. \tag{2.89}$$

The leading modulation index is

$$\beta_2 = \frac{\varepsilon_2}{2\omega_p} = -\frac{\omega_0}{16\,\omega_p}\left(\frac{\pi A}{\Phi_0}\right)^2. \tag{2.90}$$

We use the Jacobi–Anger identity $e^{iz\sin\theta} = \sum_{m=-\infty}^{\infty} J_m(z)\, e^{im\theta}$ to expand

$$e^{-i[\delta_0 t - \beta_2 \sin(2\omega_p t)]} = e^{-i\delta_0 t}\, e^{+i\beta_2 \sin(2\omega_p t)} = \sum_{m=-\infty}^{\infty} J_m(\beta_2)\, e^{-i(\delta_0 - 2m\omega_p)t}.$$

Substituting into H_I shows that each Fourier component carries a Bessel coefficient $J_m(\beta_2)$ and oscillates at $\delta_0 - 2m\omega_p$. *Population exchange occurs when a sideband is (nearly) stationary*, i.e.

$$\delta_0 \approx 2m\,\omega_p \quad (m \in \mathbb{Z}). \tag{2.91}$$

The first accessible sideband is $m = \pm 1$, giving the pump frequency

$$\boxed{\omega_p^*(A) = \frac{1}{2}\,|\delta_0(A)| = \frac{1}{2}\left|(\omega_1 - \omega_0) + \frac{\omega_0}{8}\left(\frac{\pi A}{\Phi_0}\right)^2\right|} \tag{2.92}$$

On this resonance, the effective exchange rate is [25, 26]

$$\boxed{g_{\text{eff}} = g\left|J_1(\beta_2)\right| \;\approx\; g\,\frac{|\beta_2|}{2} = g\,\frac{\omega_0}{32\,\omega_p}\left(\frac{\pi A}{\Phi_0}\right)^2 \quad (\ |\beta_2| \ll 1\ ),} \tag{2.93}$$

with the theoretical single-tone ceiling

$$\boxed{g_{\text{eff}}^{\max} \approx 0.582\,g \quad \text{at} \quad |\beta_2| \approx 1.84,} \tag{2.94}$$

set by the global maximum of $|J_1|$ [27]. Solving $|\beta_2| = 1.84$ for A gives

$$A_{\text{opt}} = \frac{4\Phi_0}{\pi}\sqrt{\frac{1.84\,\omega_p}{\omega_0}}, \qquad \text{(idealized; ignores higher-order/RWA breakdown/dephasing).} \tag{2.95}$$

Harmonics at $\delta_0 \approx 4\omega_p, 6\omega_p, \ldots$ are present but suppressed: their amplitudes scale as $J_m(\beta_2) \sim (\beta_2/2)^m$ for $|\beta_2| \ll 1$ [27]. Since here $\beta_2 \propto A^2$ [Eq. (2.90)], the sideband of order m scales as A^{2m}, i.e. much weaker than the leading ($m = 1$) channel when the pump amplitude is small compared to one flux quantum. Operating at this point keeps the qubit's frequency modulated *around its flux sweet spot* (where $d\omega_q/d\Phi = 0$), which minimizes phase–decoherence (dephasing) during the mixing process. The downside is that the frequency at which population transfer occurs becomes *amplitude dependent*: the effective resonance (and hence the exchange rate) shifts with the pump amplitude. In practice, this is addressed by jointly calibrating the exchange-pulse frequency and amplitude. The benefit of near-minimal phase

error at the sweet spot far outweighs the modest, additional calibration step required to track the amplitude-dependent resonance.

When the qubit is set to a nonzero DC flux bias (generic bias; "one-photon" activation) or for $\sin a \neq 0$ we have $\varepsilon_1 = Af'(\phi_{\rm DC}) \neq 0$ and $\beta_1 = \varepsilon_1/\omega_p \neq 0$. The expansion of $e^{-i\phi(t)}$ then contains fundamental sidebands at $\delta_0 \approx n\omega_p$ $(n = 1, 2, \ldots)$ with the *primary* resonance at

$$\delta_0(A) \approx \omega_p \quad \Rightarrow \quad \omega_p^*(A) \approx |\delta_0(A)|, \tag{2.96}$$

and effective coupling $g_{\rm eff} \approx g\,|J_1(\beta_1)| \simeq g\,|\beta_1|/2$ for $|\beta_1| \ll 1$ [25, 28]. Here the DC shift $\delta_0(A) = \omega_1 - \omega_2^{\rm DC}(A)$ includes the quadratic term from Eq. (2.82); to this order the amplitude dependence of the *frequency condition* enters only through that DC Stark shift.

We have used the rotating-wave approximation (RWA) for the exchange sector ($g \ll \omega_{1,2}$), small-amplitude expansions in A/Φ_0, and ignored drive-induced dephasing/AC-Stark and counter-rotating Bloch–Siegert corrections. These are well documented in parametric-gate analyses [25, 26, 28] and can be included perturbatively if needed.

2.4 Entanglement and Two-Qubit Gates

Entanglement is a uniquely quantum correlation between subsystems that cannot be described by any classical joint probability distribution. A bipartite pure state $|\psi\rangle_{AB}$ is *entangled* if it cannot be written as a product $|\psi\rangle_A \otimes |\psi\rangle_B$. Entanglement enables nonclassical tasks such as teleportation and superdense coding, and forms a resource underlying quantum advantage in computation and communication [29].

Bell showed that any local hidden-variable (LHV) theory must satisfy certain inequalities on correlators [30]. The Clauser–Horne–Shimony–Holt (CHSH) form bounds the Bell param-

eter S by $|S| \leq 2$ for all LHV models [31]. Quantum mechanics predicts (and experiments confirm) violations up to the Tsirelson bound $|S| \leq 2\sqrt{2}$ with entangled states such as the Bell states [32, 33]. This demonstrates that entanglement has no classical counterpart. The four Bell states form a maximally entangled orthonormal basis:

$$|\Phi^{\pm}\rangle = \frac{1}{\sqrt{2}}\left(|00\rangle \pm |11\rangle\right), \qquad |\Psi^{\pm}\rangle = \frac{1}{\sqrt{2}}\left(|01\rangle \pm |10\rangle\right). \tag{2.97}$$

Two standard routes to generate them are (i) the *circuit* route using a Hadamard and a CNOT, and (ii) the *Hamiltonian* route using exchange interactions (e.g., iSWAP / $\sqrt{\text{iSWAP}}$) that coherently swap single excitations between qubits.

Let the Hadamard and CNOT (control on qubit 1, target qubit 2) be

$$H = \frac{1}{\sqrt{2}}\begin{pmatrix} 1 & 1 \\ 1 & -1 \end{pmatrix}, \qquad \text{CNOT} = \begin{pmatrix} 1 & 0 & 0 & 0 \\ 0 & 1 & 0 & 0 \\ 0 & 0 & 0 & 1 \\ 0 & 0 & 1 & 0 \end{pmatrix}, \tag{2.98}$$

in the computational bases $\{|0\rangle, |1\rangle\}$ and $\{|00\rangle, |01\rangle, |10\rangle, |11\rangle\}$ respectively. Acting on $|00\rangle$:

$$(H \otimes I)\,|00\rangle = \tfrac{1}{\sqrt{2}}(|00\rangle + |10\rangle), \tag{2.99}$$

$$\text{CNOT}(H \otimes I)\,|00\rangle = \tfrac{1}{\sqrt{2}}(|00\rangle + |11\rangle) = |\Phi^{+}\rangle. \tag{2.100}$$

Similarly, choosing different inputs or local Z phases yields any desired Bell state. The Hadamard gate is implemented from native single-qubit rotations available via resonant microwave XY control. For example, H can be synthesized as a short sequence of calibrated X and Y pulses [20, 34]. A CNOT is compiled by combining a CZ with single-qubit Hadamards

on the target qubit:

$$\mathrm{CNOT} = (I \otimes H)\ \mathrm{CZ}\ (I \otimes H).$$

Two-qubit entangling gates on superconducting processors are realized through hardware-native interactions such as the cross-resonance (CR) gate [35] or controlled-Z (CZ) gates activated by flux tuning or tunable couplers [23, 36, 37].

Entanglement from exchange: iSWAP and $\sqrt{\text{iSWAP}}$ The iSWAP gate swaps $|01\rangle \leftrightarrow |10\rangle$ and multiplies by i, leaving $|00\rangle$ and $|11\rangle$ unchanged:

$$U_{\text{iSWAP}} = \begin{pmatrix} 1 & 0 & 0 & 0 \\ 0 & 0 & i & 0 \\ 0 & i & 0 & 0 \\ 0 & 0 & 0 & 1 \end{pmatrix}, \qquad U_{\sqrt{\text{iSWAP}}} = \begin{pmatrix} 1 & 0 & 0 & 0 \\ 0 & \frac{1+i}{2} & \frac{1-i}{2} & 0 \\ 0 & \frac{1-i}{2} & \frac{1+i}{2} & 0 \\ 0 & 0 & 0 & 1 \end{pmatrix}. \tag{2.101}$$

In many superconducting platforms, iSWAP is generated by an XY (exchange) Hamiltonian

$$\frac{H_{\text{ex}}}{\hbar} = J\left(\sigma_1^+\sigma_2^- + \sigma_1^-\sigma_2^+\right), \tag{2.102}$$

so that, restricted to the single-excitation subspace $\{|01\rangle, |10\rangle\}$,

$$U(t) = e^{-iH_{\text{ex}}t/\hbar} = \begin{pmatrix} \cos(Jt) & -i\sin(Jt) \\ -i\sin(Jt) & \cos(Jt) \end{pmatrix}. \tag{2.103}$$

Starting from $|01\rangle$:

$$|\psi(t)\rangle = \cos(Jt)\,|01\rangle - i\sin(Jt)\,|10\rangle. \tag{2.104}$$

At $t = \frac{\pi}{4J}$ (halfway to a full iSWAP),

$$|\psi\big(\tfrac{\pi}{4J}\big)\rangle = \tfrac{1}{\sqrt{2}}(|01\rangle - i\,|10\rangle)\,, \tag{2.105}$$

which is maximally entangled (locally equivalent to $|\Psi^{\pm}\rangle$ up to single-qubit phase shifts). Continuing to $t = \frac{\pi}{2J}$ yields a full iSWAP: $|01\rangle \mapsto -i\,|10\rangle$. This exchange can be achieved directly or parametrically as explained in the previous text. All we have to do is replace $J \to g_{\text{eff}}$; stopping the evolution at $t = \pi/(4g_{\text{eff}})$ implements $\sqrt{\text{iSWAP}}$ and generates Bell-quality entanglement directly from $|01\rangle$ or $|10\rangle$.

2.4.1 Concurrence as an entanglement measure

The basis of entanglement is that two-qubit states cannot be written as a tensor product of two individual qubit states. This inseparability is the root of quantum correlations between subsystems. The Bell states in Eq. (2.97) are examples of maximally entangled states. But if our paired qubits are only partially entangled, how can we measure the correlation between them? To quantify correlations from the full density matrix of a qubit pair, *William K. Wootters* proposed a method [38]. For a general two-qubit *mixed* state ρ, define the "spin-flipped" matrix $\tilde{\rho} = (\sigma_y \otimes \sigma_y)\,\rho^*\,(\sigma_y \otimes \sigma_y)$ and $R = \rho\,\tilde{\rho}$. Let $\{\lambda_i\}$ be the eigenvalues of R in decreasing order of their square roots. The *concurrence* is

$$C(\rho) = \max\Big\{0,\ \sqrt{\lambda_1} - \sqrt{\lambda_2} - \sqrt{\lambda_3} - \sqrt{\lambda_4}\Big\}\,. \tag{2.106}$$

For a *pure* state $|\psi\rangle = a\,|00\rangle + b\,|01\rangle + c\,|10\rangle + d\,|11\rangle$, Eq. (2.106) reduces to

$$C(|\psi\rangle) = 2|ad - bc|. \tag{2.107}$$

Examples:

- $|\Phi^+\rangle = \frac{1}{\sqrt{2}}(|00\rangle + |11\rangle) \Rightarrow C = 1$ (maximal entanglement).
- Exchange evolution $|\psi(t)\rangle = \cos(Jt)\,|01\rangle - i\sin(Jt)\,|10\rangle$ has $C = 2|0{\cdot}0 - \cos(Jt)(-i\sin(Jt))| = |\sin(2Jt)|$, peaking at $t = \pi/(4J)$ (the $\sqrt{\text{iSWAP}}$ point).

So the concurrence value for a two-qubit state ranges from 0 (completely uncorrelated) to 1 for maximally entangled states.

Conclusion In this chapter, we discussed the fundamentals of qubits, with a particular focus on the transmon qubit. We examined how the individual components coupled to a qubit can be used to control and measure its state. We also explored the implementation of two-qubit gates, which enable qubit–qubit coupling and the generation of entanglement. Finally, we considered how entanglement can be quantified from the density matrix of a two-qubit manifold. These tools and concepts are essential for operating a quantum computer and will prove valuable for understanding the experiments and theoretical frameworks presented in the following chapters. Equipped with this foundation, we now turn to the next chapter, where an entangled qubit pair is used to probe the non-Markovianity of an environment.

Chapter 3

Open Quantum Systems

3.1 Introduction

Decoherence is one of the main obstacles to building reliable quantum technologies. It occurs when a quantum system becomes entangled with its environment, and information about the system is lost because the environment is not directly observed [39, 40]. A common way to describe this process is through the Gorini–Kossakowski–Sudarshan–Lindblad (GKSL) master equation [41, 42]. This equation assumes that the environment is weakly coupled to the system and has no memory, a situation known as the Markovian regime [43].

Markovian noise is simple to model and often works well in practice. In fact, carefully designed Markovian dissipation has been used as a tool for state preparation, stabilization, error correction, and quantum simulation [44–51]. However, many physical systems are not purely Markovian. In such cases, the environment retains a memory of its interaction with the system. The resulting non-Markovian dynamics cannot be described by the GKSL equation and are instead captured by the Nakajima–Zwanzig formalism [52, 53], which explicitly includes memory effects. Such dynamics are common in systems with structured reservoirs or strong coupling.

Non-Markovianity is not merely a source of unwanted noise—it can also be a useful

resource. Memory effects can improve fault tolerance [54–56], enable better control [57], protect coherence [58], and enhance quantum protocols such as teleportation [59]. Detecting and quantifying non-Markovianity is therefore an important part of understanding open quantum systems.

In this chapter, we use superconducting qubits both as entanglement probes and as a controllable environment. By coupling one qubit of an entangled pair to an engineered reservoir, we monitor how entanglement evolves over time and detect signatures of information backflow. We also use additional qubits to build a tunable environment with adjustable memory. This approach allows us to study and control the transition between Markovian and non-Markovian dynamics in a highly flexible and programmable way.

3.2 Quantifying Non-Markovian Behavior

To properly capture the non-Markovian behavior of a quantum environment, it is important that the measure we use be sensitive to *both energy relaxation and dephasing memory effects*. In other words, the probe quantity should contain information about changes in both populations and coherences. There are two widely used and experimentally accessible ways to quantify non-Markovianity (fig. 3.1): the **trace distance** method [34, 60–62] and the **concurrence** (entanglement) method [38, 63].

3.2.1 Trace distance method

In the trace distance approach, we prepare two different initial states $\rho_1(0)$ and $\rho_2(0)$ and let both interact with the environment for the same duration. After this interaction, we

measure their *trace distance* [34]

$$D\big(\rho_1(t), \rho_2(t)\big) = \frac{1}{2}\big\|\rho_1(t) - \rho_2(t)\big\|_1. \tag{3.1}$$

If the environment is Markovian, each state is driven toward the same steady (thermalized) state, causing the trace distance to *decay exponentially to zero* over time. This reflects a one-way flow of information from the system to the environment with no memory [61, 62].

However, if the environment retains quantum information, the trace distance exhibits *nontrivial time evolution* [60, 61]. In particular, there can be intervals during which the trace distance *increases*, signaling that some information previously lost has flowed back into the system. This behavior is illustrated schematically in Fig. 3.1 (red curve). The total amount of information backflow can be quantified by integrating over all intervals where the trace distance grows:

$$\mathcal{N}_D = \int_{t_0}^{t_f} dt \left| \frac{dD\big(\rho_1(t), \rho_2(t)\big)}{dt} \right| - \Delta D, \tag{3.2}$$

where $\Delta D = D(t_0) - D(t_f)$. For Markovian dynamics, $\mathcal{N}_D = 0$, whereas any positive contribution indicates non-Markovianity [61, 62].

3.2.2 Concurrence method

Entanglement has no classical analogue, so it is a natural probe of quantum memory effects in the environment [63]. In this method, we prepare two qubits—a system (Q) and an ancilla (A)— in a maximally entangled state, such as

$$|\Phi^+\rangle = \frac{1}{\sqrt{2}}\big(\,|01\rangle + e^{i\phi}\,|10\rangle\,\big), \tag{3.3}$$

and then let one or both qubits interact with the environment while the other is kept isolated. If the environment is Markovian, the *concurrence* $\mathcal{C}[\rho_{Q,A}(t)]$ [38] between the two qubits decays monotonically as the entanglement is irreversibly lost.

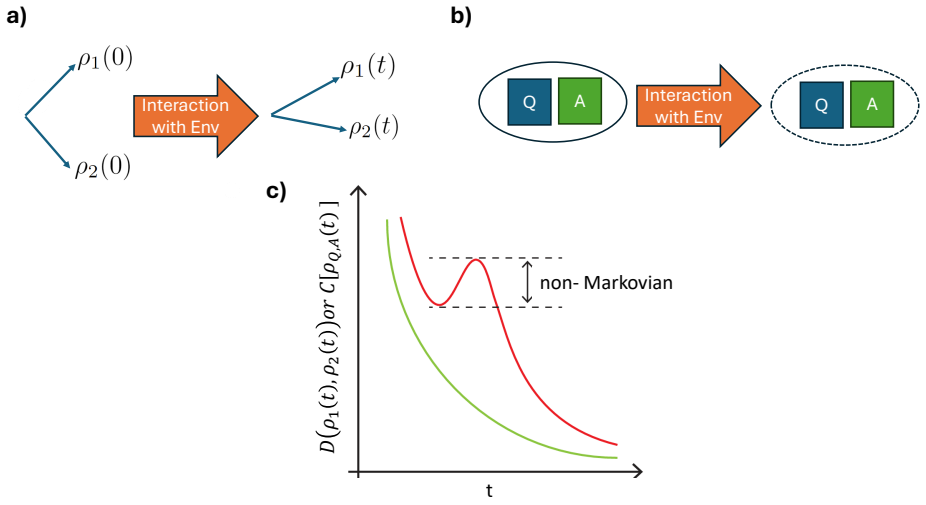

Fig. 3.1: Two methods to measure non-Markovianity of the environment : (a) the trace-distance method and (b) the concurrence method. An example of the time evolution of either quantity is shown in (c). If the observable decreases monotonically, the environment is Markovian (green curve); if there is any revival in the measured quantity, the environment has non-Markovian properties (orange curve).

On the other hand, if the environment can store and later return quantum information, part of the entanglement is temporarily transferred to the environment and then flows back. This appears as an *upward trend or revival* in the concurrence time evolution [62, 63]. We can quantify this effect using

$$\mathcal{N}_{\mathcal{C}} = \int_{t_0}^{t_f} dt \left| \frac{d\mathcal{C}[\rho_{Q,A}(t)]}{dt} \right| - \Delta\mathcal{C}, \tag{3.4}$$

where $\Delta\mathcal{C} = \mathcal{C}(t_0) - \mathcal{C}(t_f)$. As before, if there is no information backflow, $\mathcal{N}_{\mathcal{C}} = 0$; nonzero

values correspond to measurable non-Markovian behavior.

3.3 Concurrence-Based Probing of the Simulated Environment

In this chapter, we present a **Concurrence-based method** to probe the dynamics of a simulated non-Markovian environment. Our platform consists of a *three-qubit superconducting quantum processor* designed to allow controlled interactions between a probe system and an engineered environment. The layout of the processor is shown in Fig. 3.2.

The device comprises two primary qubits: a **system qubit** (Q) and an **ancilla** (A), which together form the entangled probe used to detect environmental memory. Both Q and A are coupled through a $\lambda/2$ coplanar waveguide resonator. The system qubit Q is frequency-tunable through a Superconducting QUantum Interference Device (SQUID) loop that provides a flux-tunable nonlinearity.

A third qubit, labeled **environment** (E), is also frequency-tunable and is coupled to Q via a second $\lambda/2$ resonator. All three qubits are dispersively coupled to their respective readout resonators. This architecture allows us to implement tunable and controllable coupling between the probe and the environment, which is essential for simulating different non-Markovian regimes.

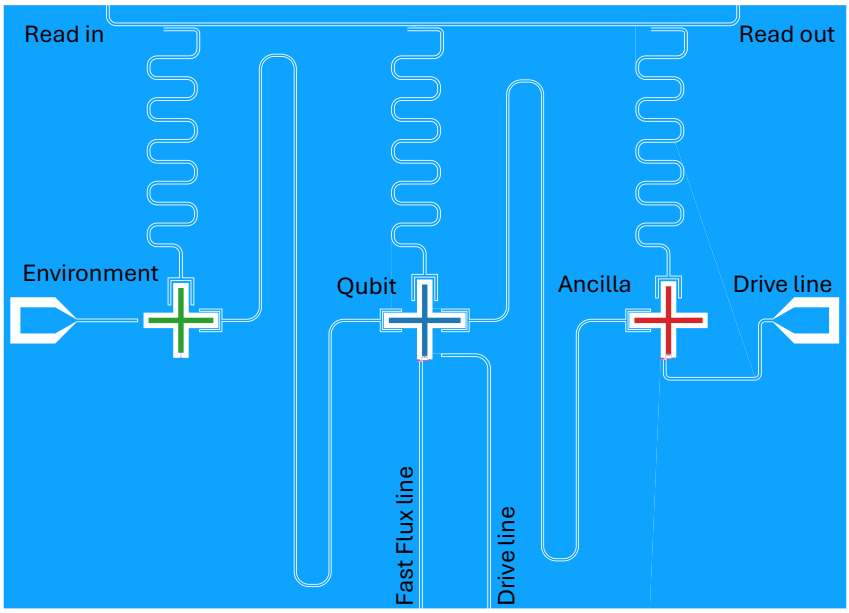

Fig. 3.2: Quantum processor layout. Schematic of the device showing three qubits labeled "Environment" (E), "Qubit" (Q), and "Ancilla" (A). Nearest-neighbor couplings are mediated by $\lambda/2$ resonators. Each qubit is dispersively coupled to a readout resonator probed through a common feedline. E and Q are frequency-tunable using on-chip fast flux lines.

3.3.1 System Hamiltonian

The dynamics of the three-qubit system can be described using the following Hamiltonian in the dispersive frame ($\hbar = 1$),

$$H = \sum_{i=\mathrm{A,Q,E}} \left[-\frac{1}{2}\tilde{\omega}_{\mathrm{q},i}\sigma_z^i + \left(\omega_{\mathrm{c},i} - \chi_{\mathrm{qc},i}\right) a_i^\dagger a_i \sigma_z^i \right] + J_{\mathrm{A,Q}}\sigma_x^{\mathrm{A}}\sigma_x^{\mathrm{Q}} + J_{\mathrm{Q,E}}\sigma_x^{\mathrm{Q}}\sigma_x^{\mathrm{E}}. \tag{3.5}$$

Here, σ_x and σ_z are Pauli operators for each qubit, and $a^\dagger$ (a) are the cavity creation (annihilation) operators. The Lamb-shifted qubit frequency is $\tilde{\omega}_{\mathrm{q}} = \omega_{\mathrm{q}} + \chi_{\mathrm{qc}}$, where χ_{qc}

is the dispersive coupling strength between each qubit and its readout resonator [5]. The coupling rates $J_{\mathrm{A,Q}}$ and $J_{\mathrm{Q,E}}$ are tuned dynamically by applying a parametric flux modulation to Q and E, which effectively activates resonant exchange interactions between the qubits [25, 28].

3.3.2 Dephasing-Induced Uncoupling: Classical vs Quantum Picture

To fully understand the experimental behavior, it is useful first to establish what we should *expect* from the system in the absence of experimental imperfections. For this purpose, we simulate the Hamiltonian dynamics of the system and examine its time evolution. We choose a simple model where the *Qubit* and the *Environment* are coupled, while the *Ancilla* remains uncoupled. The system is initialized in a maximally entangled state between the Qubit and the Ancilla so that we can directly monitor how environmental dephasing affects entanglement dynamics and energy exchange. Since the Qubit and the Ancilla are not coupled, there is no need to write an explicit interaction Hamiltonian for those two subsystems.

This simulation also highlights the fundamental physical difference between the quantum and classical pictures of an otherwise similar coupled system. While classical damping modifies the oscillation spectrum directly, quantum dephasing acts only through the Environment's *phase*, leaving the Hamiltonian spectrum untouched. This is precisely what makes the observation of Zeno suppression in such systems a clean signature of genuinely quantum behavior.

The three-qubit Hamiltonian governing the evolution of the coupled Qubit and Environment is

$$H = g\left(\sigma_E^+\sigma_Q^- + \sigma_E^-\sigma_Q^+\right), \tag{3.6}$$

where g is the coherent exchange coupling between the Environment and the Qubit. The Ancilla remains uncoupled during the evolution. All three qubits are subject to intrinsic energy relaxation at rate γ_1, while the pure dephasing rate γ_ϕ is applied to the Environment and varied systematically.

In all simulations, the pure dephasing rates on the Qubit and Ancilla are fixed at

$$\gamma_\phi^Q = \gamma_\phi^A = 20 \times 10^3 \text{ s}^{-1},$$

while the environmental dephasing rate is swept over

$$\gamma_\phi^E \in [0,\, 3 \times 10^6] \text{ s}^{-1}.$$

The coherent exchange coupling is set to

$$\frac{g}{2\pi} = 0.24 \text{ MHz}.$$

The system is initialized in the Bell state between the Qubit and Ancilla,

$$|\psi_{QA}(0)\rangle = \frac{1}{\sqrt{2}}(|01\rangle + |10\rangle),$$

while the Environment is prepared in its ground state. The Lindblad evolution is computed using `QuTiP` [64, 65], with collapse operators corresponding to both energy relaxation and pure dephasing channels.

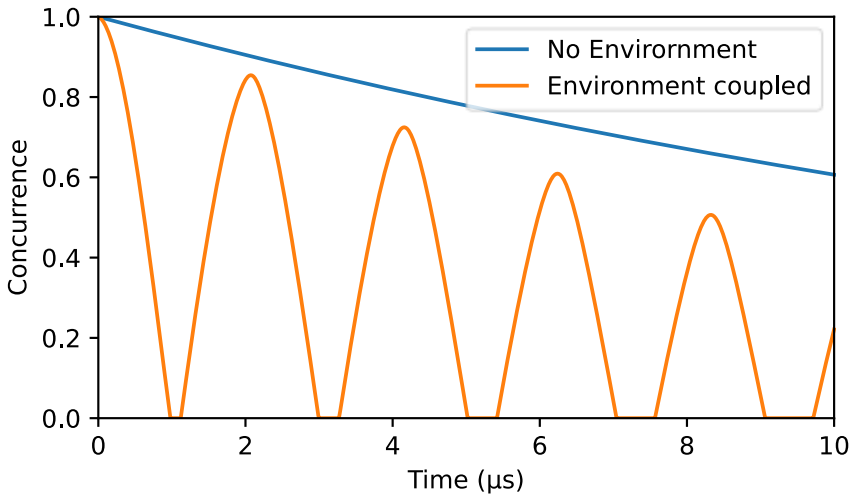

Fig. 3.3: Simulated concurrence value. The plot shows the concurrence evolution in two cases: one in which the Qubit–Environment coupling is set to zero (blue), and a second in which the Qubit is coupled to the Environment (orange).

Figure 3.3 displays the time evolution of the concurrence between the Qubit and Ancilla as the environmental coupling is turned on and off. The oscillatory trend when the coupling is on is the signature we are looking for in a non-Markovian Environment. A far richer physics landscape can be explored if we can tune the memory of the Environment. We do this by increasing the amplitude of the dephasing operator and observing what happens to the concurrence evolution. Figure 3.4(a) displays the time evolution of the concurrence between the Qubit and Ancilla as the environmental dephasing rate γ_ϕ^E is increased. For small dephasing, coherent Rabi-like exchange between the Qubit and the Environment leads to rapid degradation of entanglement between the Qubit and Ancilla. As γ_ϕ^E increases, there comes a point where the oscillations vanish completely and a purely exponential evolution appears. This is the signature of a transition from a non-Markovian to a Markovian environment. At sufficiently large $\gamma_\phi^E \gg g$, we see a reversed trend [Fig. 3.4(b)], and the concurrence

improves as we increase the noise amplitude. This indicates a well-known quantum effect, the *quantum Zeno effect* [66–69], in which frequent or effective measurement of a subsystem inhibits coherent transitions. We will discuss this effect in detail during the experimental data section.

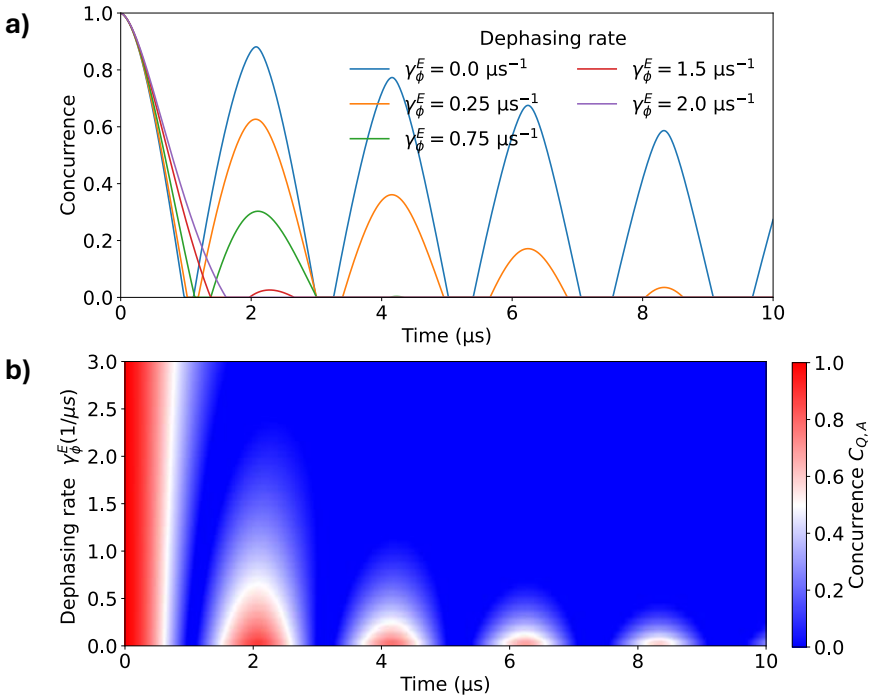

Fig. 3.4: Memory effect of the Environment. (a) Evolution of the concurrence for different dephasing rates of the Environment. (b) A 2D colormap of concurrence evolution while sweeping the dephasing rate of the Environment.

To contrast this behavior with a classical scenario, we consider a pair of linearly coupled harmonic oscillators with coupling rate g, where one oscillator (analogous to the Environment) is subject to damping γ_E. Increasing γ_E suppresses energy exchange and drives the system from underdamped oscillations to critical damping and eventually to overdamping.

The oscillation frequency of the damped classical system is

$$\Omega_{\text{cl}} = \sqrt{\omega_0^2 - \frac{\gamma_E^2}{4}}, \tag{3.7}$$

where ω_0 is the undamped resonance frequency. As γ_E increases, Ω_{cl} softens continuously and eventually vanishes at the critical damping threshold. This frequency renormalization is a direct manifestation of damping modifying the eigenvalue spectrum of the classical system.

The quantum case exhibits a qualitatively different behavior. Pure dephasing of the Environment acts only on its *phase coherence* and leaves the Hamiltonian spectrum unchanged. As a result, increasing γ_ϕ^E strongly suppresses the amplitude of coherent exchange between the Qubit and Environment but does not alter the oscillation frequency itself. Once γ_ϕ^E exceeds the coupling g, the dynamics are abruptly inhibited, effectively decoupling the two subsystems without any spectral softening.

This stands in sharp contrast to the classical picture, where damping renormalizes the normal-mode frequencies and leads to a smooth transition from oscillatory to overdamped behavior. The absence of frequency softening in the quantum case is therefore a direct signature of *quantum Zeno suppression*, reflecting the role of phase as an extra quantum degree of freedom that has no classical counterpart.

All quantum simulations presented in this section were performed using `QuTiP`, while the classical comparison was obtained from coupled linear differential equations for harmonic oscillators with tunable damping.

3.3.3 Device design and simulations

The device layout is designed using the Qiskit Metal package [70], incorporating the prominent Xmon qubit geometry [71]. The layout is then imported into Ansys to perform finite-

	$\omega_q/2\pi$ (GHz)	$\lvert\alpha\rvert/2\pi$ (MHz)	$\chi_{qc}/2\pi$ (kHz)	$\omega_c/2\pi$ (GHz)	$\kappa/2\pi$ (kHz)	T_1 (μs)	T_2^* (μs)
Ancilla	4.6 [4.2]	195 [212]	210 [230]	7.15 [6.94]	200 [270]	[32]	[41]
Qubit	5.1 [4.65]	175 [180]	210 [250]	7.3 [7.09]	200 [206]	[31]	[39]
Env.	5.6 [5.37]	180 [140]	200 [265]	7.47 [7.21]	200 [170]	[28]	[38]

Tab. 3.1: Simulated [measured] parameters of the device used in the experiment.

element simulations using the eigenmode solver. The simulation results are subsequently imported into the energy-participation quantization package [72] to extract the qubit frequencies (ω_q) and anharmonicities (α) as well as the readout resonator frequencies (ω_c) and qubit–cavity dispersive shifts (χ_{qc}). Moreover, the linewidths of the resonators (κ) are estimated using HFSS-driven modal scattering simulations after applying the 3-dB method [73] to the simulated transmission profile (S_{12}). Table 3.1 shows the simulated parameters of the device used in the experiment, with the measured values written in brackets, indicating approximately 90% agreement between simulation and measurement. Additionally, the Ancilla–Qubit and Qubit–Environment mediating resonator frequencies are designed to be 8.0 and 8.6 GHz, respectively.

3.4 Tools required to run the experiment

In this section, we discuss the tools required to experimentally realize the Hamiltonian described above. We need to set up the three-qubit quantum processor, establish two-qubit gates for both the Qubit–Ancilla and Qubit–Environment pairs, and, finally, tune the memory of the Environment.

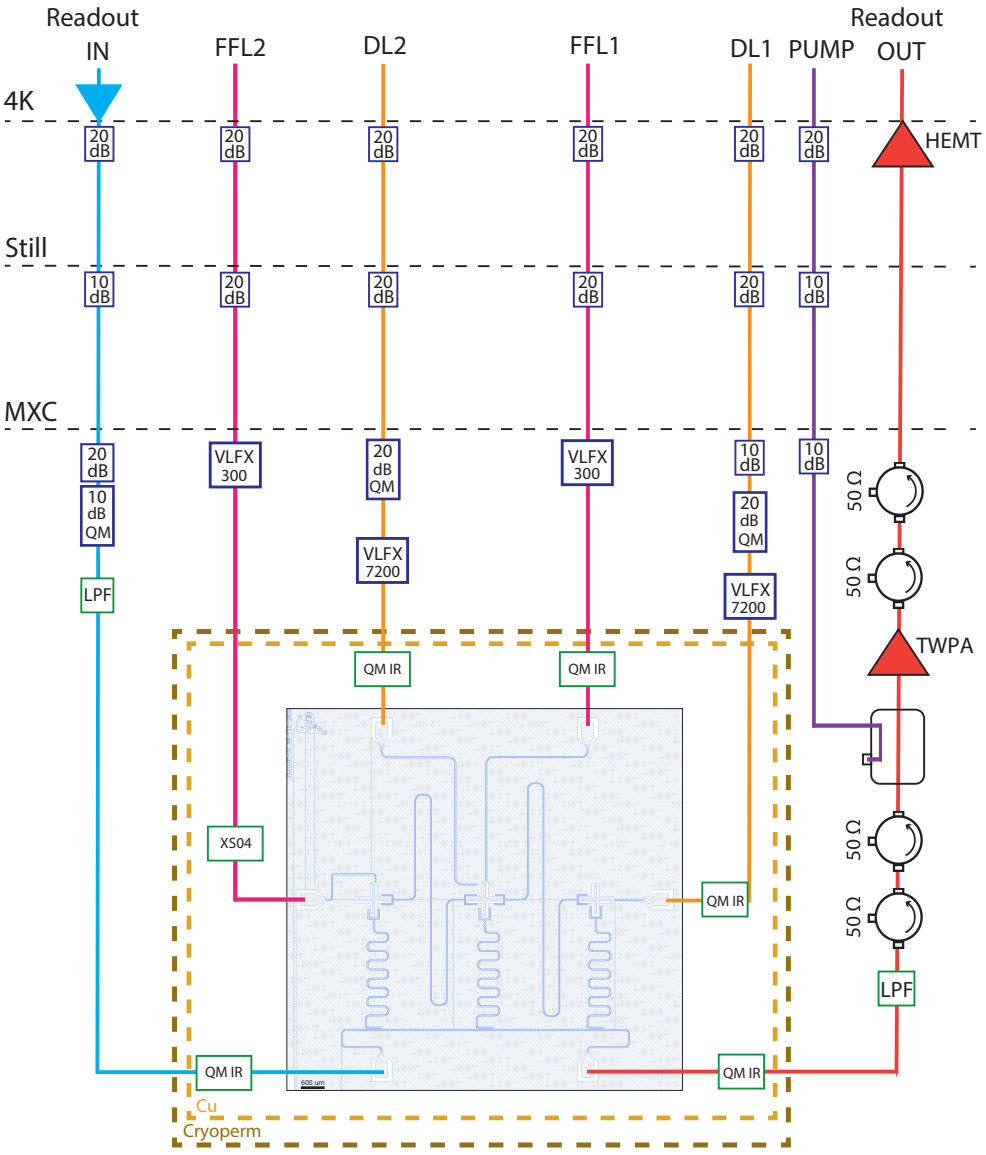

Fig. 3.5: Cryogenic setup of the experiment.

3.4.1 Experimental Setup

Figure 3.5 shows the cryogenic setup of the experiment. The device is packaged in a copper box and surrounded by an additional copper can as well as a Cryoperm shield to protect it from infrared radiation and external magnetic fields. The device is further thermalized to the

mixing-chamber stage via a copper plate. The coaxial lines are thermalized via cryogenic microwave attenuators. Note that the final attenuators are specific cryogenic attenuators (QMC-CRYOATTF).

For the fast flux lines (FFL), we used a total of 40 dB attenuation and 300 MHz low-pass filters (Mini-Circuits VLFX-300) to suppress high-frequency noise, with a bias tee at the top of the fridge to apply a DC current to tune the qubit frequencies. The drive lines DL1 and DL2 have different attenuation values (70 dB and 60 dB) to account for differences in their on-chip coupling. This arrangement of attenuators allows us to achieve Rabi oscillations as fast as 20 MHz. In addition, we installed 7.2 GHz low-pass filters (Mini-Circuits VLFX-7200+) to mitigate high-frequency noise. Finally, for the readout input line, we added 60 dB of attenuation with a K&L low-pass filter (LPF) at 8 GHz (4L250-7344/T12000-O/O). An Eccosorb infrared filter [labeled QM IR (QMC-CRYOIRF-002MF), or XS04 (an equivalent element)] was installed on every microwave line inside the copper shielding with > 10 GHz cutoff to absorb infrared radiation.

To amplify the output signal, we use a high-electron-mobility transistor (HEMT) low-noise amplifier at the 4 K stage and a traveling-wave parametric amplifier (TWPA) at millikelvin temperatures with gains of about 40 dB and 20 dB, respectively. The TWPA used in this experiment is based on the SNAIL architecture, resulting in reversed Kerr phase matching [74], with bandwidths as high as 4 GHz and noise temperatures of about 300 mK. An additional advantage of this type of TWPA is that it can be pumped at frequencies $\sim$2 GHz away from the range of interest through a directional coupler, which results in minimal interference between the pump and the readout signal.

3.4.2 Parametric Coupling and Entanglement Generation of the Qubit and Ancilla

We now move from describing the experimental setup to establishing the key qubit operations required for the experiment. The first step is to prepare the probe—an entangled state between the Qubit and the Ancilla (Fig. 3.6(a)). We implement a $\sqrt{i\text{SWAP}}$ gate to generate a maximally entangled Bell state between these two qubits.

The Qubit is frequency-tunable via a SQUID loop, while the Ancilla is a fixed-frequency transmon [10]. To minimize flux noise and maximize coherence, we park both qubits at their respective flux sweet spots and activate coupling through parametric flux modulation [25, 75]. An AC flux drive is applied to the fast flux line of the Qubit at approximately half the detuning between the Qubit and Ancilla (Fig. 3.6(c)).

To find the optimal parametric pump frequency and amplitude, we prepare the Qubit in its excited state with a π-pulse and perform spectroscopy on the Ancilla (Fig. 3.6(b)) while sweeping the pump frequency. A peak in the Ancilla response marks the resonance condition (Fig. 3.6(d)). A finer scan around this point reveals the characteristic *chevron pattern* (Fig. 3.6(e)) in the excitation probability of the Ancilla, indicating coherent energy exchange between the Qubit and Ancilla. The optimal parametric pump frequency is found to be

$$\omega_{\text{pump}} \approx \frac{1}{2}|\omega_{\text{Q}} - \omega_{\text{A}}|, \tag{3.8}$$

corresponding to half the qubit detuning [26, 28]. From this chevron profile, we extract a parametric coupling rate of $\Omega_{\text{Q,A}}/2\pi = 0.477$ MHz.

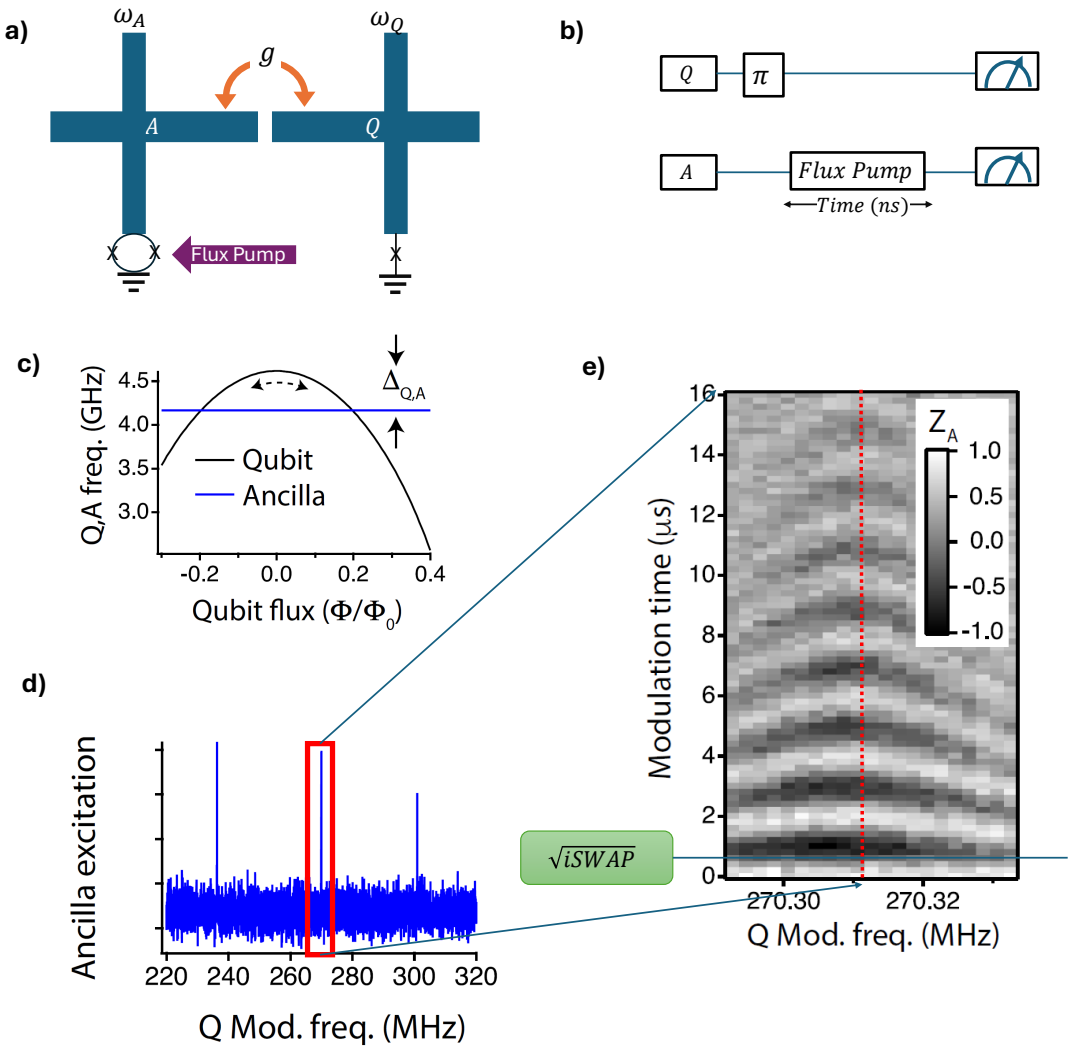

Fig. 3.6: Parametric gate calibration for the Qubit–Ancilla pair. (a) A schematic of the pair to be parametrically coupled. (b) Gate scheme to find the parametric exchange frequency and to acquire the chevron plot. (c) Frequencies of the Qubit and Ancilla while the parametric gate is on. (d) Parametric modulation of Q enables resonant coupling with A at the detuning frequency $\Delta_{\mathrm{Q,A}}/2$. (e) Parametric resonance between Q and A observed by preparing Q in its excited state and scanning the modulation frequency.

With the pump frequency and amplitude calibrated, the parametric modulation imple-

ments a tunable resonant exchange interaction described by

$$H_{\text{int}} = g_{\text{eff}}\big(\sigma_{+}^{\text{Q}}\sigma_{-}^{\text{A}} + \sigma_{-}^{\text{Q}}\sigma_{+}^{\text{A}}\big), \tag{3.9}$$

where g_{eff} is the effective coupling strength. A 530 ns parametric pulse corresponds to a $\sqrt{i\text{SWAP}}$ gate (Fig. 3.6(e)), ideally producing the Bell state

$$|\psi\rangle = \frac{1}{\sqrt{2}}\big(\,|10\rangle + e^{i\phi}\,|01\rangle\,\big), \tag{3.10}$$

where the first and second qubits correspond to the Qubit and the Ancilla, respectively.

We characterize the resulting entangled state using two-qubit quantum state tomography. Nine joint Pauli expectation values $\{\langle\Sigma_{\text{Q}}\Sigma_{\text{A}}\rangle\}$, with $\Sigma_{\text{Q,A}} \in \{X, Y, Z\}$, are measured by simultaneous readout of the Qubit and Ancilla [76]. The average single-shot readout fidelities are 0.97 (Qubit) and 0.96 (Ancilla). We reconstruct the density matrix using maximum-likelihood estimation [77], as shown in Fig. 3.7(b). The prepared Bell state exhibits a fidelity of 0.91 and a concurrence of 0.89 (Fig. 3.7(b)).

With the Qubit and Ancilla entangled, we now study the evolution of the entanglement over time. We apply the same entanglement gate as discussed earlier, but now instead of reading out the Qubit and Ancilla immediately, we wait for an increasing amount of time and plot the concurrence evolution (Fig. 3.7(a)). We display the Qubit–Ancilla concurrence versus time in Fig. 3.7(c). The concurrence slowly decreases over a timescale consistent with the individual dephasing times of the Qubit ($T_2^{*(Q)} = 39\ \mu$s) and the Ancilla ($T_2^{*(A)} = 41\ \mu$s) (Fig. 3.7(c)), i.e., $\mathcal{C} \propto \exp(-t/T_2^{*(Q)} - t/T_2^{*(A)})$, as shown by the dashed line in Fig. 3.7(c).

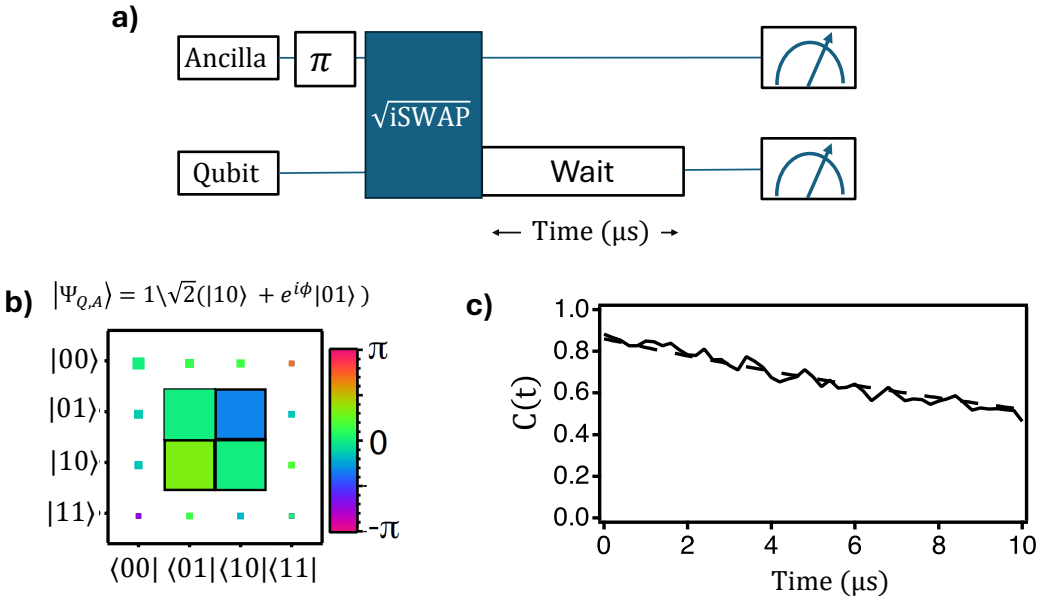

Fig. 3.7: Qubit-Ancilla (no Environment) concurrence evolution: (a) Gate schematic to measure concurrence evolution versus time. (b) The entangled state used to probe the environment. (c) Evolution of the concurrence when no engineered coupling is on. As a result, the concurrence decays exponentially with the total dephasing rate of the Qubit and Ancilla, $\gamma_\phi^Q + \gamma_\phi^A$.

3.4.3 Parametric Coupling Between Qubit and Environment

We now turn to studying the interaction of the Qubit–Ancilla subspace with the Environment. The procedure for coupling the Qubit and the Environment follows the same general approach as the Qubit–Ancilla coupling, but with additional constraints due to the fridge filtering. The detuning between the Qubit and Environment at their respective flux sweet spots is approximately 700 MHz. Driving the Qubit at half this detuning is not possible because of the 300 MHz low-pass filters on the fast flux line.

To overcome this, we use a **symmetric parametric flux modulation scheme** in which both the Qubit and Environment are driven simultaneously with the same amplitude and frequency. This creates sidebands centered between the two qubits and effectively lowers the

required pump frequency by a factor of four:

$$\omega_{\text{pump}} \approx \frac{1}{4}\left|\omega_{\text{Qubit}} - \omega_{\text{Environment}}\right| = 2\pi \times 175 \text{ rad./}\mu\text{s}. \tag{3.11}$$

This brings the two qubits into parametric resonance without modifying the fridge setup. The resulting resonant transverse coupling between the Qubit and Environment has rate

$$\Omega_{\text{Q,E}} = 2\pi \times 0.473 \text{ rad./}\mu\text{s}, \tag{3.12}$$

limited by the resonator-mediated interaction between the pair.

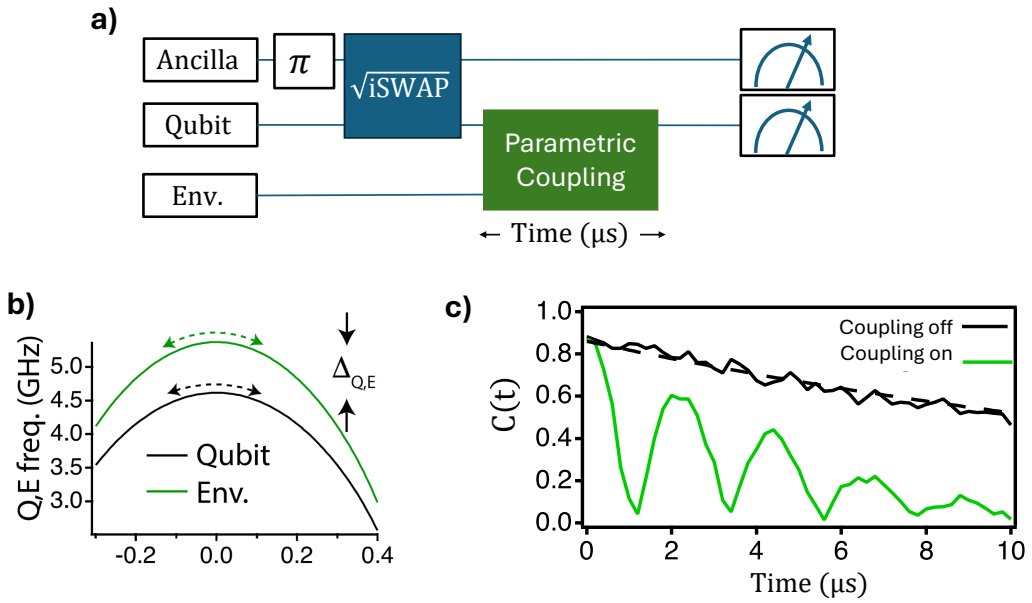

Fig. 3.8: Qubit–Environment coupling. (a) Gate sequence for the coupled Environment and entangled-pair experiment. (b) Parametric modulation of both Q and E enables population exchange at approximately $\Delta_{\text{Q,E}}/4$. (c) Concurrence evolution when the Qubit–Environment coupling is on (green) and when the coupling is off (black).

We calibrate the pump by first exciting the Qubit with a π-pulse and performing spec-

troscopy on the Environment under simultaneous flux modulation. By sweeping the pump frequency, we observe a resonance peak in the Environment response. A finer scan reveals the characteristic chevron pattern, which is used to extract the optimal pump frequency and amplitude for population exchange.

After calibration, we prepare the Qubit–Ancilla subsystem in a Bell state using the $\sqrt{i\text{SWAP}}$ gate. We then apply the parametric modulation to couple the Qubit and Environment (Fig. 3.8(a)). By varying the pump pulse length, we observe the time evolution of the concurrence $\mathcal{C}(t)$ of the Qubit–Ancilla subsystem, as shown in Fig. 3.8 (c) (green curve).

Initially, the entanglement between the Qubit and the Ancilla decreases rapidly due to the monogamy of entanglement [78]: introducing entanglement between the Qubit and the Environment necessarily reduces the entanglement between the Qubit and the Ancilla. At longer times, however, the concurrence revives as the Environment state is swapped back into the Qubit. This revival is a clear, time-resolved signature of non-Markovianity, indicating that the environment has quantum coherent memory—consistent with the fact that the environment here is itself a single two-level system.

By evaluating Eq. 3.3 over the interval $t \in [t_0 = 0\ \mu\text{s},\ t_f = 10\ \mu\text{s}]$, we obtain a non-Markovianity of $\mathcal{N} = 1.4$. This directly quantifies the strength of the memory effect associated with the Qubit–Environment coupling.

3.4.4 Tuning the Memory of the Environment via Pseudo-Thermal Noise

A key feature of this experiment is the ability to **tune the environment's memory on demand** by controlling its dephasing rate. We achieve this by injecting pseudo-thermal noise into the Environment's readout resonator, which shortens its phase-coherence time

and allows us to study how controllable memory affects non-Markovian dynamics.

We generate noise with a thermal-like spectrum by **frequency-modulating a monochromatic tone** at the Environment's readout resonator frequency (Fig. 3.9(a)) with Gaussian noise from a function generator. The modulation bandwidth ($\approx$ 1.8 MHz) ensures a flat noise spectrum around resonance. The bandwidth is set by the modulation amplitude, while the overall photon number is controlled via an I/Q mixer with a DC offset. This tunable pseudo-thermal noise acts as an adjustable dephasing channel for the Environment.

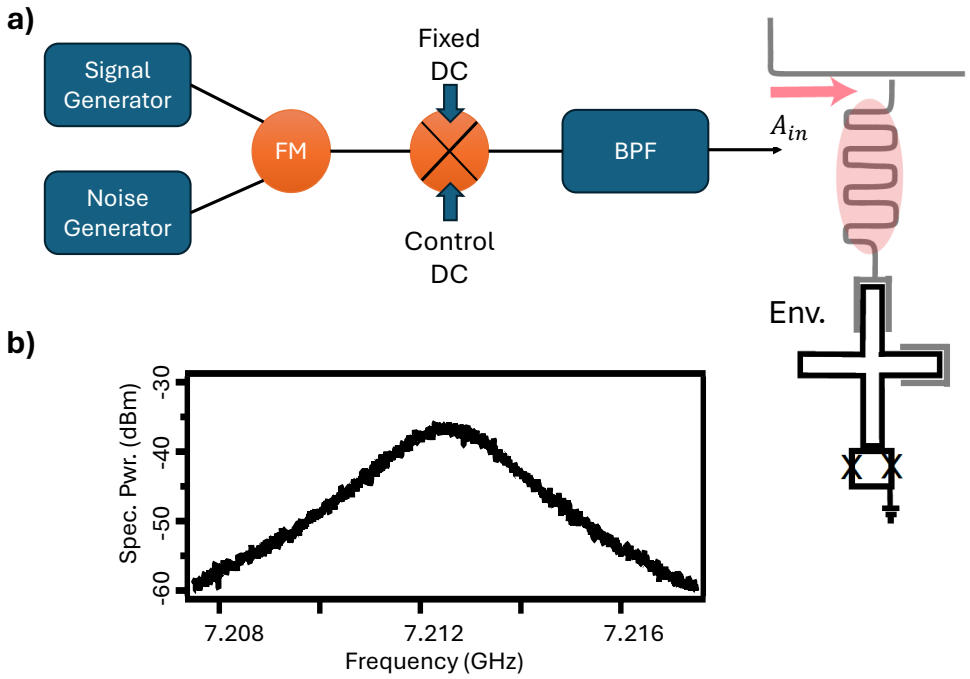

Fig. 3.9: Tuning the memory of the Environment. (a) Generation of Gaussian noise by frequency-modulating a monochromatic tone with a Gaussian noise source. (b) Noise spectrum generated by frequency-modulating a monochromatic tone with Gaussian noise. By driving the Environment's readout resonator with pseudo-thermal noise of amplitude A_{in}, we tune the Environment's memory.

When this dissipation channel is present, the Qubit–Environment parametric resonance is modified. We therefore recalibrate the parametric coupling for each noise amplitude.

Figure 3.9(b) shows the noise spectrum, while Fig. 3.10(a) presents the spectroscopy of the Environment excitation probability under parametric driving of both qubits.

At higher noise amplitudes, the resonance becomes asymmetric [Fig. 3.10(b)], consistent with a thermal photon distribution. From these spectra, we extract the FWHM linewidth, which directly corresponds to the increased Environment dephasing. We calculate the dephasing rate by performing Ramsey measurements on the Environment as we increase the noise amplitude [Fig. 3.10(c), blue]. While Ramsey is a good method to convert arbitrary noise amplitude to Environment dephasing at low rates, at higher dephasing rates Ramsey is not a reliable tool for measuring dephasing. Instead, we calculate the Environment dephasing rate at higher amplitudes by measuring the linewidth [Fig. 3.10(c), green] of the spectroscopy of the Environment excitation probability under parametric driving of both qubits and scaling by 8π to account for symmetric modulation of the Qubit and Environment at their flux sweet spots. When compared to the Environment dephasing rate obtained via Ramsey measurements [Fig. 3.10(c), blue], the scaled-linewidth method shows good agreement across a wide range of noise amplitudes, demonstrating that the parametric coupling remains robust even under strong dephasing.

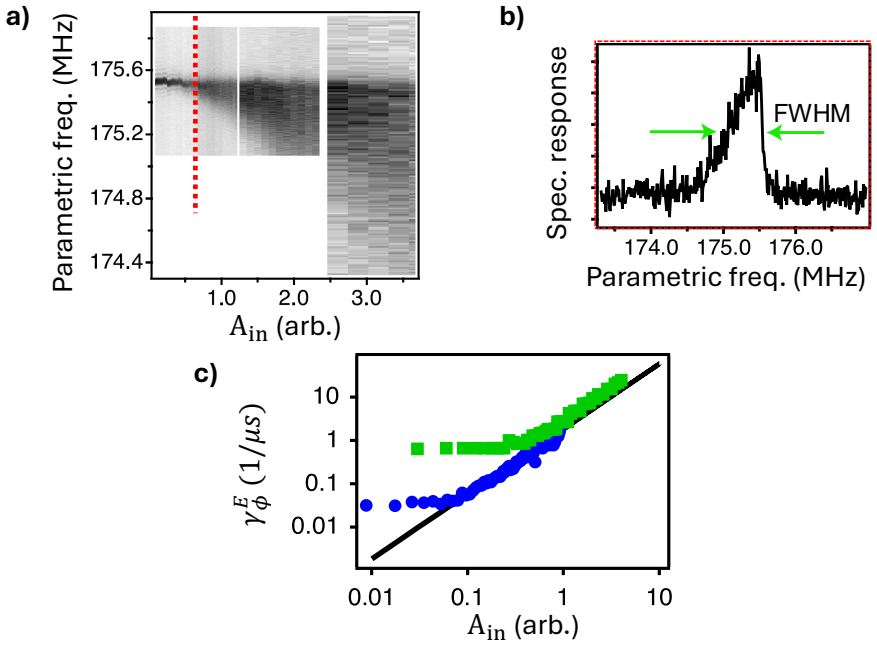

Fig. 3.10: Qubit–Environment parametric resonance in the presence of pseudo-thermal noise. (a) Spectroscopy of the Qubit–Environment parametric resonance for different noise amplitudes. (b) Asymmetric resonance profile indicative of thermal photon statistics (used to calculate line width of the Environment using FWHM). (c) Comparison between scaled linewidth (green) of Environment and its dephasing rate extracted from Ramsey measurements (blue).

Introducing pseudo-thermal photons effectively enlarges the Environment to include the quantum states of light in the readout resonator. This is described by a dispersive interaction Hamiltonian

$$H_{\text{int}} = \chi a^\dagger a \sigma_z^{\text{E}}, \tag{3.13}$$

where $\chi/2\pi = 200$ kHz is the dispersive coupling rate, $a^\dagger a$ is the resonator photon-number operator, and σ_z^{E} acts on the Environment. Fluctuations in the intra-resonator photon number induce dephasing of the Environment through an AC Stark shift [47, 79].

The noise-source bandwidth (1.8 MHz) exceeds χ, ensuring a uniform drive independent

of the Environment state, with a short correlation time (90 ns) that allows us to treat the dephasing as effectively Markovian. Direct Ramsey measurements establish a relationship between the dephasing rate γ and the input noise amplitude A_{in}:

$$\gamma = 1.84\ (\mu\text{s})^{-1} A_{\text{in}}^{1.5}, \tag{3.14}$$

as shown in Fig. 3.10(c) (black straight line).

3.5 Concurrence Evolution for Different Dephasing Rates in the Environment

We study how dephasing in the Environment controls the entanglement dynamics of the Qubit–Ancilla pair. Broadband thermal photons injected into the Environment cause a slight dispersive shift of the parametric exchange condition between the Qubit and the Environment. Consequently, for each injected-noise amplitude A_{in} we first calibrate the parametric-drive frequency so that the Qubit–Environment exchange is on resonance. Figure 3.11(a) shows the resulting calibration: starting from the Qubit in the excited state, we activate the parametric drive for a variable duration and study $Z_Q(t)$ to maximize population transfer. As the Environment dephasing is increased, the exchange contrast in the Qubit–Environment manifold diminishes.

Having calibrated the exchange frequency for each A_{in}, we next measure the time evolution of the Qubit–Ancilla concurrence for a range of Environment dephasing rates. The experimental sequence at each setting is: (i) prepare the Qubit and Ancilla in a maximally entangled Bell state, (ii) turn on the Qubit–Environment coupling, and (iii) record the concurrence versus time. In Fig. 3.11(c) we observe that increasing the Environment dephasing

induces a transition from non-Markovian (oscillatory, revival-prone) to Markovian (monotonic, envelope-like) dynamics. We quantify the suppression of memory effects using the non-Markovianity measure defined in Eq. (3.4) and summarized in Fig. 3.11(d): as the Environment dephasing is increased beyond $\gamma \simeq 1\ (\mu\mathrm{s})^{-1}$, $\mathcal{N}$ becomes consistent with zero. However, the dynamics are not immediately Markovian in the sense of being well captured by a time-homogeneous GKSL description of the reduced Qubit–Ancilla subsystem (see Introduction and [41, 42]); rather, there is a crossover. In our data, a simple exponential model for the concurrence matches well for $\gamma \gtrsim 3\ (\mu\mathrm{s})^{-1}$, whereas it fails to capture revivals and non-monotonic envelopes at smaller γ (cf. [80]). Thus, the transition is *gradual*, reflecting both experimental sensitivity and the definition of an envelope in traces with residual oscillations.

To present the complete data in one visualization, we plot a color map of concurrence versus time and Environment dephasing rate in Fig. 3.11(c). Panel 3.11(b) shows several time-domain traces for selected values of γ to illustrate two clear trends. First, in the non-Markovian regime, increasing dephasing *accelerates* the decay envelope by damping revivals (compare $\gamma = 0$ and $\gamma = 0.5$). Second, once the dynamics are Markovian, further increasing dephasing *slows* the decay of the concurrence (e.g., $\gamma = 2.4$ vs. $\gamma = 6.4$)—a hallmark of Zeno stabilization of entanglement [81–88]. Operationally, the thermal photons implement continuous measurement of the Environment at a rate set by γ, which reduces the effective Qubit–Environment exchange.

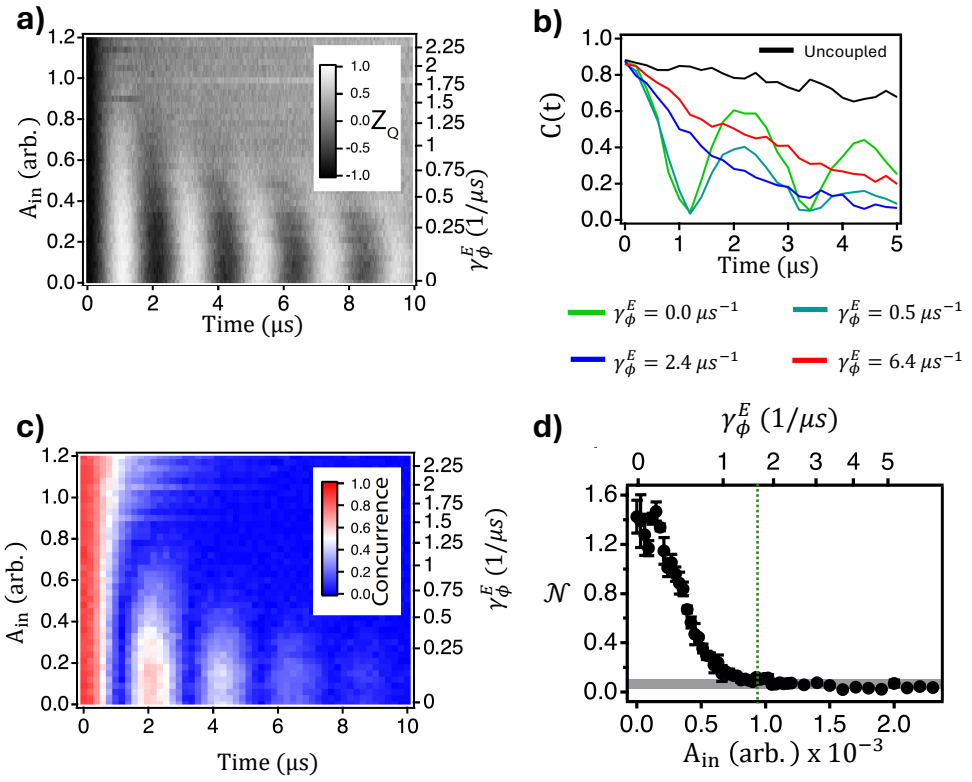

Fig. 3.11: Concurrence evolution while tuning the Environment's memory. (a) For each A_{in} we calibrate the parametric-drive frequency between the Qubit and Environment by studying $Z_Q(t)$ and maximizing the exchange [80]. (b) Concurrence versus time for selected dephasing rates. (c) Qubit–Ancilla concurrence versus time across Environment dephasing rates. The onset of monotonic behavior marks the crossover from non-Markovian to Markovian dynamics. (d) The non-Markovianity measure (3.4) across the transition. Error bars denote the standard error of the mean from three independent runs. The gray bar indicates the measure applied in the Environment decoupled case, providing a background reference.

Separating control and observable rates. A common source of confusion is the difference between the *control rate* (Environment dephasing) and the *observed decay rate* (con-

currence envelope). We therefore make this separation explicit:

$$\begin{aligned} \text{Control (set):} \quad & \gamma_\phi^E \ \text{via injected noise,} \\ \text{Observable (fit):} \quad & \Gamma_\mathrm{c} \ \text{from the concurrence envelope.} \end{aligned} \tag{3.15}$$

In the non-Markovian regime, the concurrence $C(t)$ can be oscillatory and non-monotonic; we define an upper envelope $C_{\mathrm{env}}(t)$ (via the sequence of local maxima or an equivalent monotone-envelope procedure) and fit

$$C_{\mathrm{env}}(t) \;\approx\; C_0\, e^{-\Gamma_\mathrm{c}\, t}, \qquad \text{(non-Markovian regime)}, \tag{3.16}$$

to obtain an *effective* envelope rate Γ_c. In the Markovian regime, the full trace is well modeled by a single exponential,

$$C(t) \;\approx\; C_0\, e^{-\Gamma_\mathrm{c}\, t}, \qquad \text{(Markovian regime)}, \tag{3.17}$$

so that Γ_c follows directly from a linear fit to $\ln C(t)$ on the chosen time window. For a general discussion of non-Markovianity measures and their operational signatures, see [61].

Figure 3.12 collects these observations. Panel 3.12a shows time-domain concurrence traces in the Markovian regime, where the decay slows as γ_ϕ^E increases and approaches the limiting case set by the individual dephasing of the Qubit and Ancilla when the Environment is effectively uninvolved. Panel 3.12b shows the extracted Γ_c versus γ_ϕ^E across both regimes. In the non-Markovian region (gray) Γ_c increases as revivals are suppressed; in the Markovian region Γ_c *decreases* with further increases of γ_ϕ^E, consistent with the quantum Zeno effect.

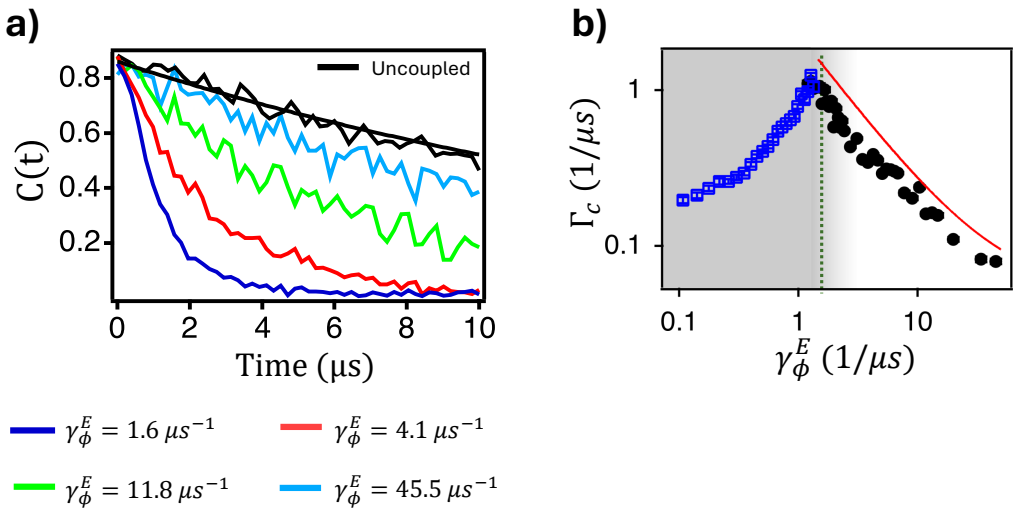

Fig. 3.12: Non-Markovianity and Quantum Zeno transition. (a) Qubit–Ancilla concurrence versus time for different Environment dephasing rates; as γ_ϕ^E increases, the decay approaches the uncoupled limit given by the Qubit and Ancilla single-qubit dephasing. (b) The exponential decay rate of the concurrence, Γ_c, versus γ_ϕ^E. The gray region denotes the non-Markovian regime, where Γ_c is obtained from fits to the (non-monotonic) envelope; in the Markovian regime Γ_c follows the expected Zeno scaling (red line).

Zeno scaling and the pinning limit. On exact resonance, the coherent exchange between the Qubit and Environment is generated by

$$H_{\rm int} \;=\; g\left(\sigma_E^+\sigma_Q^- + \sigma_E^-\sigma_Q^+\right), \qquad \Rightarrow \qquad \Omega_{Q,E} \approx 2g, \tag{3.18}$$

where $\Omega_{Q,E}$ is the exchange (Rabi) frequency of the Qubit–Environment subsystem. In the Zeno picture, rapid dephasing of the Environment (frequent effective measurement) suppresses coherent exchange, leading to the inverse-rate scaling

$$\Gamma_c \;=\; \frac{\Omega_{Q,E}^2}{4\,\gamma_\phi^E} \;+\; \Gamma_0, \qquad \Gamma_0 \equiv \frac{1}{T_2^{*Q}} + \frac{1}{T_2^{*A}}, \tag{3.19}$$

which we observe at large γ_ϕ^E [86, 89]. Here Γ_0 is the baseline concurrence decay rate in the absence of Environment-mediated exchange. Importantly, the *disappearance of oscillations* at intermediate γ_ϕ^E indicates a loss-dominated, still-coupled manifold; it does *not* by itself imply full decoupling. Only at very large γ_ϕ^E does Zeno pinning confine the Environment to pointer subspaces, suppressing the *effective* Qubit–Environment coupling and approaching the decoupled limit [67].

Conclusion. By sweeping γ_ϕ^E and jointly tracking the non-Markovianity measure and the fitted envelope rate Γ_c, we map a continuous crossover from non-Markovian dynamics (revivals, memory) to Zeno-stabilized Markovian dynamics (single-exponential decay) using an entanglement-assisted probe. The probe is sensitive to *quantum* memory in the Environment: a classical environment that stores populations but lacks coherence would not generate concurrence revivals, in line with canonical non-Markovianity criteria [61]. This capability is useful for testing the quantum nature of decoherence channels (e.g., in quantum-gravity–motivated scenarios [90]). Moreover, by introducing controllable dissipation to the Environment, we observe stabilization of the Qubit–Ancilla subsystem, underscoring dissipation as a powerful tool for quantum subspace engineering [51].

Chapter 4

Non-linearity and Amplification

The detection and measurement of quantum systems pose unique challenges that fundamentally differ from classical measurement techniques. A typical qubit state in a quantum non-demolition (QND) measurement involves only ∼1–10 photons circulating in the readout resonator. Such weak signal energies make direct measurement with room-temperature electronics impractical, as the signal power is often several orders of magnitude below the thermal noise floor at 300 K. This limitation establishes the essential role of *amplification* in quantum measurement chains. Amplifiers not only enhance the desired signal but also inevitably amplify any existing noise within the system. Furthermore, the amplification process itself introduces additional noise, as illustrated schematically in Fig. 4.1. At first glance, it may appear counterintuitive that amplification could degrade the signal-to-noise ratio (SNR); after all, if both signal and noise are amplified equally, one might expect the SNR to remain constant. However, the key advantage of amplification is that it **raises the signal power above the noise floor** of subsequent measurement stages. Without an initial low-noise amplifier, a weak quantum signal would remain indistinguishable from the background noise of downstream components. By boosting the signal, even at the cost of adding some noise, the relative signal power at later stages increases, making it more discernible to room-temperature detectors. In practice, the first-stage quantum amplifier

determines the overall sensitivity of the entire measurement chain.

The quantitative impact of added noise and gain distribution in a cascade of amplifiers can be understood through the *Friis equation* (Eq. (4.2)), which expresses the total noise figure of a multi-stage amplification chain. The *noise figure* F of a two-port is

$$F \equiv \frac{\mathrm{SNR}_{\mathrm{in}}}{\mathrm{SNR}_{\mathrm{out}}} \geq 1, \tag{4.1}$$

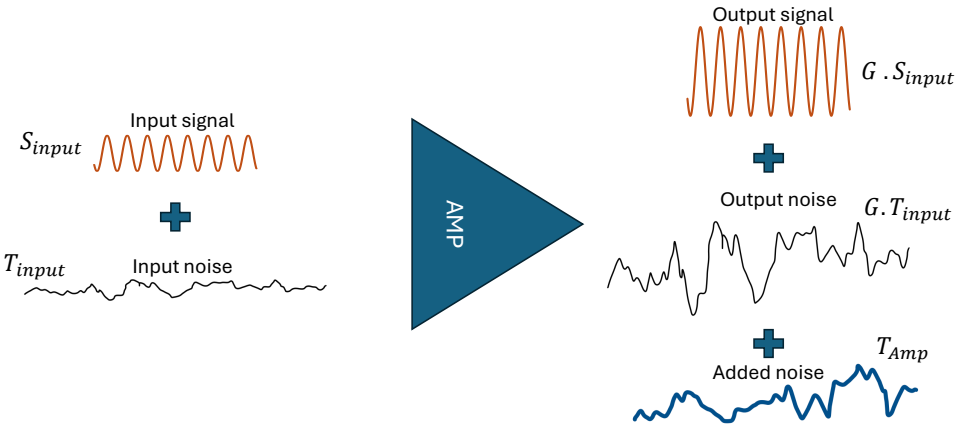

Fig. 4.1: Basic operational principle of an amplifier: the input signal, along with its inherent noise, is amplified to a level well above the noise floor of subsequent stages. Additional noise introduced by the amplifier is also shown schematically.

and in a cascade amplifier arrangement, the total noise figure obeys the *Friis formula*

$$F_{\mathrm{tot}} = F_1 \; + \; \frac{F_2 - 1}{G_1} \; + \; \frac{F_3 - 1}{G_1 G_2} \; + \; \cdots \, , \tag{4.2}$$

with G_i the (power) gain of stage i [91]. In the equivalent noise-temperature form,

$$T_{\text{sys}} = T_1 \; + \; \frac{T_2}{G_1} \; + \; \frac{T_3}{G_1 G_2} \; + \; \cdots \, , \tag{4.3}$$

so **large first-stage gain** suppresses the contributions of all following stages. Classically, the input noise floor is $k_{\text{B}}TB$ (per unit bandwidth B) and gets multiplied by the gain, while internal resistive and device noise adds in quadrature via (4.2)–(4.3).

For example, a cryogenic high-electron-mobility transistor (HEMT) still exhibits excess noise from carrier scattering and tunneling processes. But even at 4 K—the temperature at which HEMTs are typically operated in a quantum computing environment—the thermal noise overwhelms any quantum fluctuations. But what happens at sub-millikelvin temperatures, when the amplifier has zero resistivity? That is where quantum amplifiers operate. The knowledge of quantum limitations becomes more useful here, since T_1 now corresponds to the noise temperature of a quantum-limited amplifier, and any noise dictated by quantum phenomena becomes comparable to the thermal noise. We will study the quantum limit imposed on the amplification process.

4.1 Quantum Amplification

Noiseless, phase-preserving amplification of an *arbitrary* quantum state would effectively copy both quadratures without disturbance. That runs headlong into the no-cloning theorem: a physical (linear, CPTP) map cannot duplicate unknown states. The only consistent way for a deterministic phase-preserving amplifier to exist is to *add noise* so that information is not duplicated perfectly and the map remains linear. This intuition is formalized by the Haus–Caves limit. To quantitatively understand it, we should look at the process of

amplification. We work with bosonic operators obeying $[a, a^\dagger] = 1$. A naive single-mode rescaling $a_{\text{out}} = \sqrt{G}\, a_{\text{in}}$ violates the commutator unless $G = 1$ [92, 93]. This forces either (i) a second *idler* mode (phase-preserving case), or (ii) mixing a mode with its own conjugate (phase-sensitive case).

4.1.1 Phase-preserving (nondegenerate)

Postulate the most transparent linear map with an *arbitrary* idler amplitude gain g_i:

$$a_{s,\text{out}} = \sqrt{G}\, a_{s,\text{in}} + g_i\, e^{i\phi}\, a_{i,\text{in}}^\dagger, \tag{4.4}$$

and assume $[a_{s,\text{in}}, a_{i,\text{in}}] = [a_{s,\text{in}}, a_{i,\text{in}}^\dagger] = 0$ (distinct modes). Imposing the canonical commutator at the output,

$$\left[a_{s,\text{out}}, a_{s,\text{out}}^\dagger\right] = G\,[a_{s,\text{in}}, a_{s,\text{in}}^\dagger] - |g_i|^2\,[a_{i,\text{in}}, a_{i,\text{in}}^\dagger] = G - |g_i|^2 \stackrel{!}{=} 1, \tag{4.5}$$

fixes the idler amplitude gain to

$$|g_i| = \sqrt{G-1}. \tag{4.6}$$

Thus the physically allowed, commutation-preserving input–output relation is

$$a_{s,\text{out}} = \sqrt{G}\, a_{s,\text{in}} + \sqrt{G-1}\, e^{i\phi}\, a_{i,\text{in}}^\dagger, \qquad G \geq 1, \tag{4.7}$$

which is exactly the standard form usually obtained via a Bogoliubov parametrization [92–94]. Define signal quadratures $I_s = (a_s + a_s^\dagger)/2$ and $Q_s = (a_s - a_s^\dagger)/(2i)$. Equation (4.7) amplifies both I_s and Q_s by the same *amplitude* factor $\sqrt{G}$ (up to a global rotation set by ϕ), so their relative phase is unchanged—hence the name *phase-preserving* amplification.

4.1.2 Phase-sensitive (degenerate)

For a degenerate parametric amplifier (DPA), there is *no independent idler mode*. Work directly in quadratures and assign *arbitrary* amplitude gains $\sqrt{G_I}$ and $\sqrt{G_Q}$ to the two conjugate quadratures:

$$I_{\text{out}} = \sqrt{G_I}\, I_{\text{in}}, \qquad Q_{\text{out}} = \sqrt{G_Q}\, Q_{\text{in}}. \tag{4.8}$$

To preserve the canonical commutator $[I, Q] = i/2$, we require

$$[I_{\text{out}}, Q_{\text{out}}] = \sqrt{G_I G_Q}\, [I_{\text{in}}, Q_{\text{in}}] = i\, \frac{\sqrt{G_I G_Q}}{2} \stackrel{!}{=} i\, \frac{1}{2}, \tag{4.9}$$

which *fixes* the product of the gains:

$$G_I\, G_Q = 1. \tag{4.10}$$

Choosing the device phase so that X is the amplified quadrature ($G_I \equiv G \geq 1$) gives the unique companion gain

$$G_Q = \frac{1}{G}. \tag{4.11}$$

Thus a DPA necessarily *amplifies* one quadrature and *deamplifies* (compresses) the orthogonal one:

$$I_{\text{out}} = \sqrt{G}\, I_{\text{in}}, \qquad Q_{\text{out}} = \frac{1}{\sqrt{G}}\, Q_{\text{in}}. \tag{4.12}$$

In annihilation-operator form this is equivalent to

$$a_{\text{out}} = \mu\, a_{\text{in}} + \nu\, e^{i\phi}\, a_{\text{in}}^{\dagger}, \quad \mu = \frac{\sqrt{G} + \frac{1}{\sqrt{G}}}{2}, \quad \nu = \frac{\sqrt{G} - \frac{1}{\sqrt{G}}}{2}, \tag{4.13}$$

which indeed satisfies $|\mu|^2 - |\nu|^2 = 1$ and reproduces Eq. (4.12) [93, 95].

Added Noise in Each Case In a phase-preserving amplifier, the extra, independent idler port *must* inject vacuum fluctuations to keep $[a_{\text{out}}, a_{\text{out}}^\dagger] = 1$. That vacuum is the entire origin of the added noise. From $a_{s,\text{out}} = \sqrt{G}\, a_{s,\text{in}} + \sqrt{G-1}\, e^{i\phi} a_{i,\text{in}}^\dagger$ (fixed by the commutator), the idler contributes $(G-1) \times \text{Var(vacuum)}$ to the *output* variance per quadrature. With $\text{Var}(I_{\text{vac}}) = \text{Var}(Q_{\text{vac}}) = \frac{1}{4}$ and noise units $S \equiv 2\,\text{Var}$ (so vacuum is $S_{\text{vac}} = \frac{1}{2}$ "quanta per quadrature"), the input-referred added noise is simply

$$N_{\text{add}}^{(\text{PP})} = \frac{(G-1)\, S_{\text{vac}}}{G} = \frac{G-1}{2G} \xrightarrow{G \gg 1} \frac{1}{2}.$$

The *idler's vacuum* is exactly the added noise, and in the large-gain limit it amounts to *half a quantum per quadrature* (the Haus–Caves limit) [92, 93]. By contrast, in the phase-sensitive (degenerate) case there is no independent idler; properly phased, one quadrature (say I) can be amplified with *zero* added noise while the orthogonal quadrature Q is squeezed [93, 95].

4.2 Parametric Amplifier

A *parametric amplifier* is an amplifier in which work is supplied by *modulating a circuit parameter*—typically a reactive element such as an effective capacitance or inductance—at a pump frequency. A strong pump performs this parametric work; a weak input signal then *draws energy from the pump* via the time-dependent reactance, resulting in gain [**ManleyRowe1956**, 95].

We begin with the **classical** small-signal picture, modeling a resonator whose reactance is modulated at (or near) a combination of the signal and idler frequencies. This viewpoint makes the basic features transparent: the *gain–detuning* dependence emerges from the lin-

earized equations of motion and phase matching, and the familiar *gain–bandwidth trade-off* follows from how parametric coupling loads the resonator's response [93, 94]. We then turn to the **quantum** description, where amplification is conveniently viewed as *photon conversion* mediated by the pump: in three-wave processes a pump photon splits into a signal–idler pair, while in four-wave processes two pump photons convert into one signal and one idler. This perspective naturally explains phase-preserving versus phase-sensitive operation and the fundamental noise constraints (e.g., the Haus–Caves limit for phase-preserving gain) [92, 93]. Practically, two pumping modalities are common: (i) *three-wave mixing* (explicit modulation of a reactance at $\omega_p \approx \omega_s + \omega_i$ or $2\omega_s$), and (ii) *four-wave mixing* (Kerr-mediated self-modulation by a strong pump near the mode frequency). We will use the classical model to build intuition for gain versus detuning and the gain–bandwidth product, and then formalize these results in the quantum picture, where energy flow and noise are accounted for at the photon level [93–95].

4.2.1 Classical picture

A parametric amplifier is a resonant circuit whose natural frequency is periodically modulated by an external pump. Classically, such a system can be modeled as a damped harmonic oscillator with a time-varying resonance frequency (Fig. 4.2). Let the instantaneous angular frequency be modulated as

$$\omega^2(t) = \omega_0^2 + \alpha \cos(\Omega_p t), \tag{4.14}$$

where ω_0 is the static resonance frequency, Ω_p is the pump frequency, and α sets the modulation depth (pump strength). Including a damping term κ, which characterizes the linewidth (or bandwidth) of the resonator, the equation of motion reads

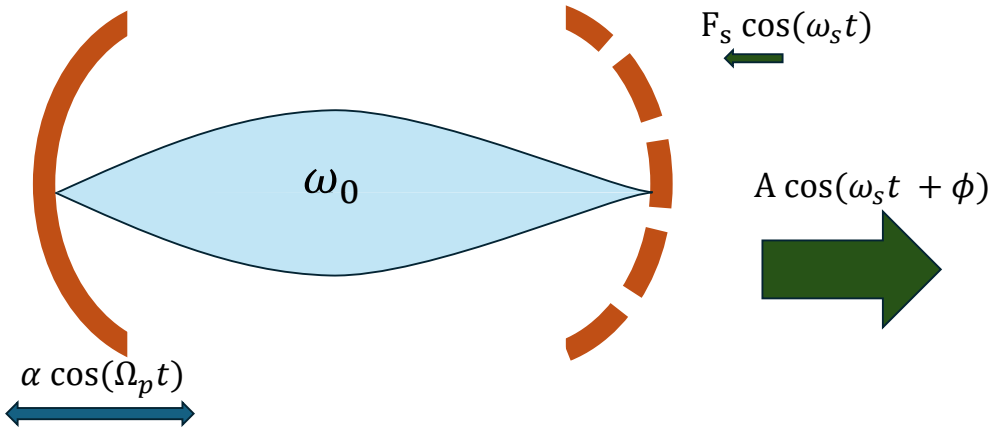

Fig. 4.2: Classical parametric amplfier: A Fabry–Pérot cavity used as a parametric amplifier: a tunable cavity in which one boundary condition is varied in time by an external pump. A weak signal is coupled in through a partially transmitting boundary.

$$\ddot{x}(t) + \kappa\dot{x}(t) + \left[\omega_0^2 + \alpha\cos(\Omega_p t)\right]x(t) = F_s\sin(\omega_s t), \tag{4.15}$$

where $x(t)$ is the generalized coordinate (e.g., voltage or current), and $F_s\sin(\omega_s t)$ represents a small input drive at signal frequency ω_s.

4.2.2 Small-signal steady-state solution

We seek a steady-state solution of (4.15) in the presence of a weak pump and a small signal near resonance ($|\omega_s - \omega_0| \ll \omega_0$). For the degenerate case $\Omega_p = 2\omega_0$, we write the motion as

a slowly varying envelope on the carrier:

$$x(t) = X(t)e^{i\omega_s t} + X^*(t)e^{-i\omega_s t}, \tag{4.16}$$

where $\dot{X} \ll \omega_s X$. Substituting into (4.15) and retaining only near-resonant terms (rotating-wave approximation) yields the coupled envelope equations

$$\left(-i\Omega + \frac{\kappa}{2}\right) X + \frac{\alpha}{2} X^* = \frac{F_s}{2i\omega_0}, \tag{4.17}$$

$$\left(+i\Omega + \frac{\kappa}{2}\right) X^* + \frac{\alpha}{2} X = -\frac{F_s^*}{2i\omega_0}, \tag{4.18}$$

where $\Omega = \omega_s - \omega_0$ is the detuning. These equations describe coupling between the signal and its phase-conjugate "idler" component through the pump modulation.

4.2.3 Frequency-dependent gain

Solving (4.17) for X under steady-state drive gives the complex response and the power gain for the amplified quadrature as

$$\boxed{G(\Omega) = \frac{\left(\frac{\kappa}{2} + \frac{\alpha}{2}\right)^2 + \Omega^2}{\left(\frac{\kappa}{2} - \frac{\alpha}{2}\right)^2 + \Omega^2}}. \tag{4.19}$$

This expression is valid below the parametric threshold $\alpha < \kappa$. At zero detuning ($\Omega = 0$), the on-resonance gain simplifies to

$$\boxed{G_0 = \left(\frac{\frac{\kappa}{2} + \frac{\alpha}{2}}{\frac{\kappa}{2} - \frac{\alpha}{2}}\right)^2}. \tag{4.20}$$

Beyond the linear model. In deriving Eq. (4.20) we assumed a single mode, constant α (undepleted pump), and negligible higher-order nonlinearity. As $\alpha \to \kappa$ the linear solution becomes marginally stable; in experiment one encounters either (i) the onset of parametric self-oscillation or (ii) gain compression due to Kerr nonlinearity and pump depletion, with internal loss and phase mismatch further rounding the response. These effects replace the divergence with a finite peak gain and define the dynamic range (e.g., the 1 dB compression point).

4.2.4 Gain–bandwidth product

The amplifier bandwidth is defined by the detuning $\Omega_{3\mathrm{dB}}$ at which the gain drops by half:

$$G(\Omega_{3\mathrm{dB}}) = \frac{G_0}{2}. \tag{4.21}$$

Substituting Eqs. (4.19) and (4.20) into (4.21) and solving for $\Omega_{3\mathrm{dB}}$ yields

$$\boxed{\Omega_{3\mathrm{dB}} = \sqrt{\frac{G_0}{G_0 - 2}} \left(\frac{\kappa}{2} - \frac{\alpha}{2}\right).} \tag{4.22}$$

In the high-gain limit ($G_0 \gg 1$), this simplifies to

$$\boxed{\Omega_{3\mathrm{dB}} \approx \frac{\kappa}{\sqrt{G_0}}.} \tag{4.23}$$

Expressed in linear frequency ($B = \Omega_{3\mathrm{dB}}/2\pi$), the classical amplitude gain–bandwidth product becomes

$$\boxed{\sqrt{G_0}\, B \approx \frac{\kappa}{2\pi} = \frac{\omega_0}{2\pi Q_L},} \tag{4.24}$$

where $Q_L = \omega_0/\kappa$ is the loaded quality factor of the resonator.

Interpretation. Equation (4.24) shows that for a resonator-based parametric amplifier, the product of amplitude gain and bandwidth is constant and determined by the resonator linewidth. As the pump strength α increases, the gain rises but the bandwidth narrows proportionally to $1/\sqrt{G_0}$, so the overall gain–bandwidth product remains fixed. This trade-off is fundamental to all linear parametric amplification processes.

4.2.5 Quantum picture

Any parametric amplifier requires a nonlinear element to respond to an external drive and modulate the frequency of the resonator. In superconducting platforms, Josephson-junction devices are the most widely used nonlinear elements, as they can be modeled as a nonlinear inductance.

The inductance of a superconducting quantum interference device (SQUID), denoted L_J, is periodic in the external magnetic flux Φ_{ext}, with a period of one flux quantum $\Phi_0 = h/2e$. This nonlinear inductance arises from the Josephson effect and can be expressed as

$$L_J(\Phi_{\text{ext}}) = \frac{\Phi_0}{2\pi I_c \cos\left(\pi \frac{\Phi_{\text{ext}}}{\Phi_0}\right)}, \tag{4.25}$$

where I_c is the critical current of the SQUID junctions, Φ_0 is the magnetic flux quantum, and Φ_{ext} is the applied external flux. The $\cos(\pi\Phi_{\text{ext}}/\Phi_0)$ term encodes the flux dependence, giving rise to a tunable inductance and hence a tunable resonance frequency when incorporated into an LC circuit. This periodicity originates from the interference of superconducting wavefunctions in the SQUID loop, a direct manifestation of the Josephson effect [96].

When the SQUID inductance is placed in parallel with a capacitance C, the resonance

frequency of the circuit is given by

$$\omega_r(\Phi_{\text{ext}}) = \frac{1}{\sqrt{L_J(\Phi_{\text{ext}})\, C}}. \tag{4.26}$$

By modulating Φ_{ext}, the resonance frequency of the LC circuit can therefore be tuned with high precision, making the SQUID a versatile tool for parametric amplification. Using this relation, one can plot the resonance frequency as a function of external flux, as illustrated in Fig. 4.3. The points labeled **symmetric** and **asymmetric** are of particular significance in amplifier operation. At the symmetric point ($\Phi_{\text{ext}} = 0$), the pump frequency is approximately equal to the resonance frequency, and amplification arises from a **four-wave mixing** process. In contrast, at the asymmetric point ($\Phi_{\text{ext}} = 0.25\Phi_0$), the pump frequency is approximately twice the resonance frequency, and amplification occurs via a **three-wave mixing** process [97].

To understand the quantum picture of a parametric amplifier, we begin with the Hamiltonian of a tunable LC resonator:

$$\hat{H}(t) = \frac{\hat{\phi}^2}{2L(t)} + \frac{\hat{Q}^2}{2C}, \tag{4.27}$$

where: $\hat{\phi}$ is the flux operator, $\hat{Q}$ is the charge operator, $L(t)$ is the time-dependent inductance, C is the capacitance. This Hamiltonian describes the energy of the resonator in terms of its quantum-mechanical degrees of freedom. The flux operator $\hat{\phi}$ and charge operator $\hat{Q}$ satisfy the canonical commutation relation $[\hat{\phi}, \hat{Q}] = i\hbar$, reflecting their conjugate nature in the quantum regime [98]. The time-dependent inductance $L(t)$ introduces parametric modulation, which is essential for amplification. We can rewrite the Hamiltonian in terms of the instantaneous frequency $\omega(t)$ of the resonator, which is a function of the applied external

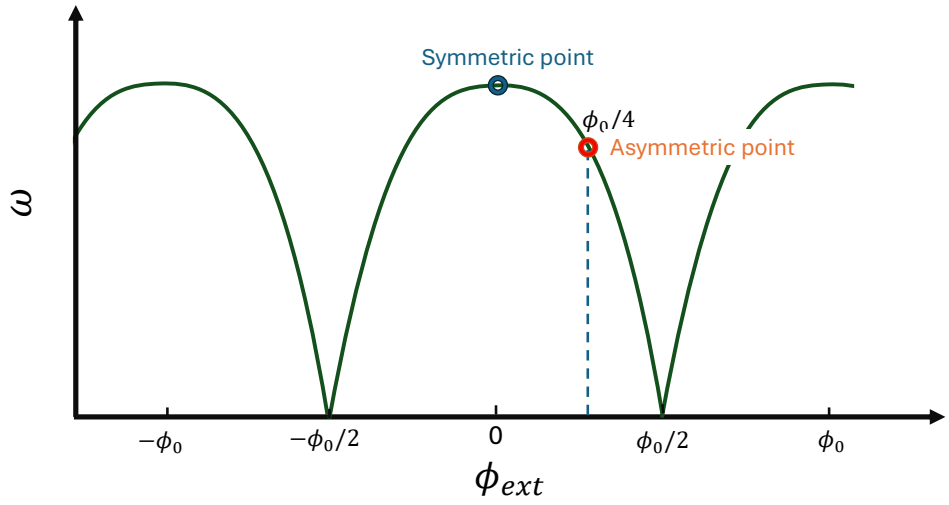

Fig. 4.3: (Frequency vs. Flux): Resonance frequency versus external magnetic flux for a SQUID-tuned LC resonator. The symmetric point (green) corresponds to zero external flux, where the pump frequency matches the resonator frequency, enabling four-wave mixing. The asymmetric point (red) corresponds to $\Phi_{\text{ext}} = 0.25\Phi_0$, where the pump frequency is twice the resonator frequency, enabling three-wave mixing. The periodic dependence of the frequency on Φ_{ext} reflects quantum interference effects in the SQUID loop.

DC flux bias and the pump tone *via a small AC flux* $\phi(t)$ around Φ_{DC}:

$$\hat{H}(t) = \frac{C\,\omega^2(t)}{2}\,\hat{\phi}^2 + \frac{\hat{Q}^2}{2C}, \tag{4.28}$$

with

$$\Phi_{\text{ext}}(t) = \Phi_{\text{DC}} + \phi(t), \qquad \omega(t) = \omega\big(\Phi_{\text{ext}}(t)\big). \tag{4.29}$$

For small oscillations, expand the frequency about the bias point and neglect higher orders:

$$\omega(t) \approx \omega_b + \omega_b'\,\phi(t) + \frac{1}{2}\,\omega_b''\,\phi^2(t), \qquad \omega_b \equiv \omega(\Phi_{\text{DC}}),\ \omega_b' \equiv \left.\frac{\partial\omega}{\partial\Phi}\right|_{\Phi_{\text{DC}}},\ \omega_b'' \equiv \left.\frac{\partial^2\omega}{\partial\Phi^2}\right|_{\Phi_{\text{DC}}}. \tag{4.30}$$

In a rotating frame of reference with respect to the input signal frequency, both the flux and charge operators can be expressed in terms of the mode's creation ($\hat{a}^\dagger$) and annihilation ($\hat{a}$) operators:

$$\hat{\phi} = \sqrt{\frac{\hbar}{2C\omega_b}}(\hat{a} + \hat{a}^\dagger), \quad \hat{Q} = -i\sqrt{\frac{\hbar C\omega_b}{2}}(\hat{a} - \hat{a}^\dagger). \tag{4.31}$$

Here, we are considering the simpler case where the input and idler modes are degenerate and can be represented by the same photonic modes. Substituting $\hat{\phi}$, $\hat{Q}$, and the $\omega(\Phi_{\mathrm{DC}} + \phi)$ expansion back into the Hamiltonian, we obtain (up to a constant):

$$\hat{H}(t) = \hbar\omega_b\hat{a}^\dagger\hat{a} + \frac{\hbar}{4}\left[2\,\frac{\omega_b'}{\omega_b}\,\phi(t) + \frac{\omega_b''}{\omega_b}\,\phi^2(t)\right](\hat{a} + \hat{a}^\dagger)^2. \tag{4.32}$$

In this Hamiltonian, the first term represents the energy of a simple harmonic oscillator. The second term is responsible for the creation of signal photons by down-converting pump photons and vice versa.

4.2.5.1 Four-wave mixing

When the amplifier is operated close to zero DC flux bias, the first-order derivative of frequency with respect to the pump tone vanishes (Fig. 4.4a) ($\omega_b' \approx 0$). Thus, the Hamiltonian simplifies to:

$$\phi(t) = \Phi_{\mathrm{ac}}\cos(\omega_p t), \qquad \omega_b' \approx 0, \tag{4.33}$$

so that

$$\hat{H}(t) = \hbar\omega_b\hat{a}^\dagger\hat{a} + \frac{\hbar}{4}\,\frac{\omega_b''}{\omega_b}\,\phi^2(t)\,(\hat{a}\hat{a}^\dagger + \hat{a}^\dagger\hat{a} + \hat{a}^2 + \hat{a}^{\dagger 2}). \tag{4.34}$$

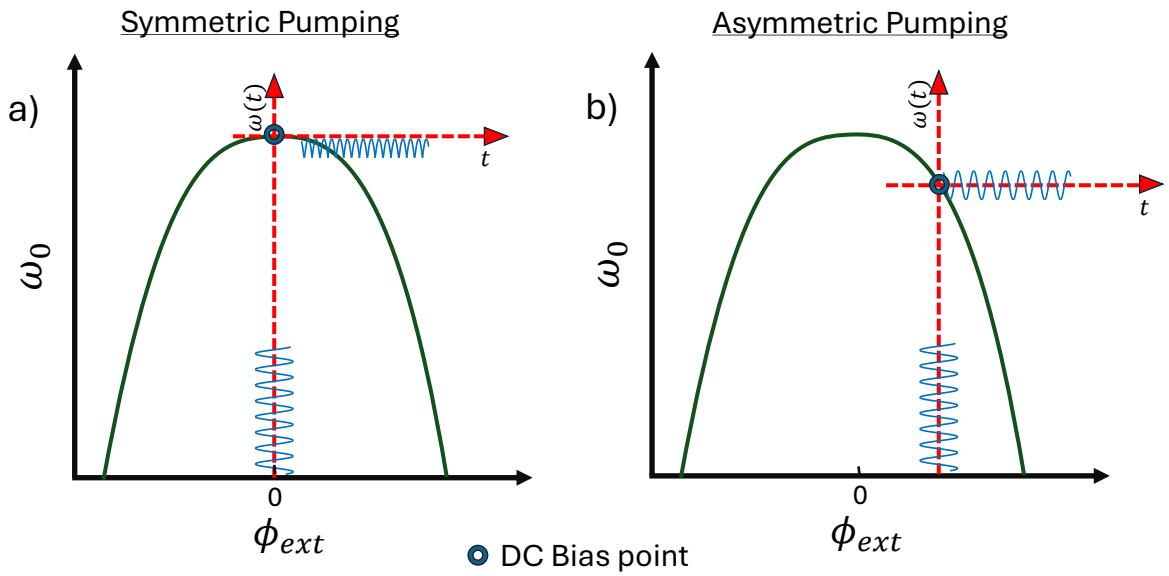

Fig. 4.4: AC pumping schemes. (a) Flux pumping when biased at zero flux quanta: the resonator's modulation frequency is twice the pump frequency. (b) Flux pumping when biased near $\Phi_0/4$ flux quanta: the resonator's modulation frequency equals the pump frequency.

With $\phi^2(t) = \frac{\Phi_{\rm ac}^2}{2}\big[1+\cos(2\omega_p t)\big]$,

$$\hat{H}(t) = \hbar\omega_b \hat{a}^\dagger\hat{a} + \frac{\hbar}{8}\frac{\omega_b''}{\omega_b}\Phi_{\rm ac}^2\Big[1+\cos(2\omega_p t)\Big]\,(\hat{a}\hat{a}^\dagger + \hat{a}^\dagger\hat{a} + \hat{a}^2 + \hat{a}^{\dagger 2}). \tag{4.35}$$

Separating the DC Stark shift and the oscillatory parametric term, and moving to a frame rotating at ω_p (RWA), gives

$$\boxed{\hat{H}_{\rm 4WDPA} = \hbar\Delta_4\hat{a}^\dagger\hat{a} + \frac{\hbar g_4}{2}\,(\hat{a}^2 + \hat{a}^{\dagger 2})} \tag{4.36}$$

with

$$\Delta_4 = \omega_b + \delta\omega_{\rm Stark} - \omega_p, \qquad \delta\omega_{\rm Stark} = \frac{\omega_b''}{4\,\omega_b}\Phi_{\rm ac}^2, \qquad g_4 = \frac{\omega_b''}{8\,\omega_b}\Phi_{\rm ac}^2. \tag{4.37}$$

Stationarity of the squeezing term requires $2\omega_p \approx 2\omega_b$ (degenerate 4WM, i.e., $\omega_p \approx \omega_b$).

4.2.5.2 Three-wave mixing

If we now bias the resonator at approximately $\Phi_{\mathrm{DC}} = \Phi_0/4$ (Fig. 4.4b), the frequency-versus-flux curve can be approximated as linear for small pump amplitudes. This allows us to ignore the second- and higher-order derivative terms in the Hamiltonian (4.32), simplifying it to:

$$\hat{H}(t) = \hbar\omega_b \hat{a}^\dagger \hat{a} + \frac{\hbar}{2}\frac{\omega_b'}{\omega_b}\,\phi(t)\,(\hat{a}\hat{a}^\dagger + \hat{a}^\dagger\hat{a} + \hat{a}^2 + \hat{a}^{\dagger 2}). \tag{4.38}$$

Here, we assign η to represent the slope of the frequency response with respect to the flux. Similar to the previous section, we define the pump tone as a monochromatic signal:

$$\phi(t) = \Phi_{\mathrm{ac}} \cos(\omega_p t).$$

Keeping only near-resonant terms and moving to a frame rotating at $\omega_p/2$ (RWA), the Hamiltonian becomes:

$$\boxed{\hat{H}_{\mathrm{3WDPA}} = \hbar\Delta_3 \hat{a}^\dagger\hat{a} + \frac{\hbar g_3}{2}\,(\hat{a}^2 + \hat{a}^{\dagger 2})} \tag{4.39}$$

with

$$\Delta_3 = \omega_b - \frac{\omega_p}{2}, \qquad g_3 = \frac{\omega_b'}{4\,\omega_b}\,\Phi_{\mathrm{ac}}. \tag{4.40}$$

Because the modulation is asymmetric, the resonance frequency oscillates both above and below the assigned DC bias, resulting in a net zero average frequency shift due to the pump modulation. This removes one tuning parameter—the pump detuning. From the above Hamiltonian, it is clear that the pump frequency must be twice the resonance frequency ($\omega_p = 2\omega_s \approx 2\omega_b$). In this process, one pump photon is converted into a signal photon and

an idler photon, a mechanism known as **three-wave mixing**. This type of amplification is highly sought after due to its simplicity and efficiency.

Connection to Non-Hermitian Physics

The above Hamiltonians will reappear in the next chapter, where they will be used to explore **non-Hermitian physics**. Non-Hermitian Hamiltonians are essential for describing open quantum systems, where gain and loss mechanisms play a significant role. The three-wave mixing process, with its inherent simplicity and well-defined photon-conversion dynamics, provides an ideal platform for studying such phenomena.

4.3 Superconducting Flux-Driven JPA

An experimental flux-driven JPA was designed and tested. This type of amplifier is capable of operating through both three-wave and four-wave mixing processes to achieve amplification. The device under consideration was first developed using finite element method (FEM) simulation software; the specific simulation techniques and design challenges will be discussed in detail in a later chapter. For now, we focus on the main aspects of the design without delving into the full design process.

The amplifier consists of an LC resonator weakly coupled to a 50-Ω environment. In addition to the linear inductance, the resonator incorporates a nonlinear inductance provided by four SQUIDs connected in series. These SQUIDs are inductively coupled to a broadband transmission line, which serves as the flux-pump line. A GDS layout of this system is shown in Fig. 4.5.

The main advantage of the above device is its simple yet effective design, which can be fabricated using a single-layer double-angle deposition process. The device was subsequently

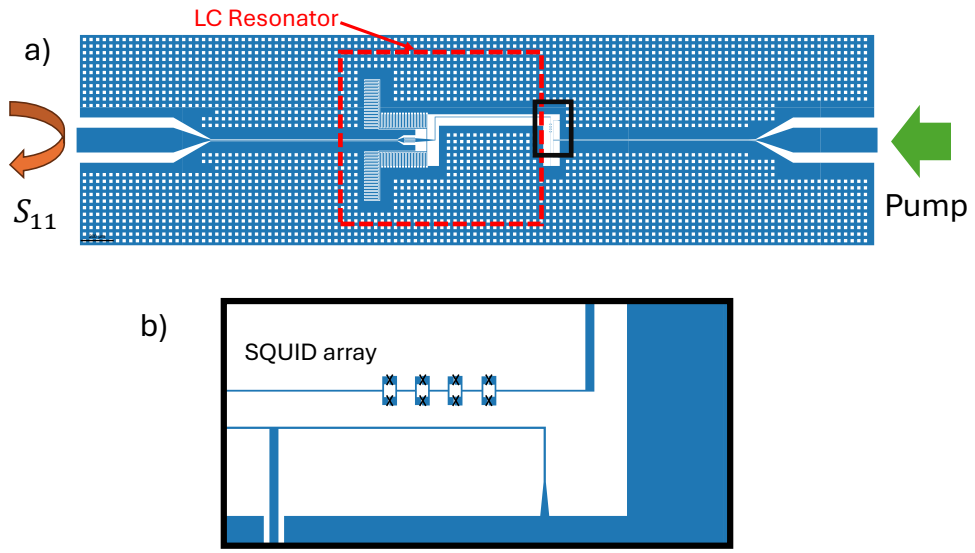

Fig. 4.5: Flux-driven JPA: (a) The complete GDS layout showing the LC resonator (red box) and the SQUID array (black box). (b) Zoomed-in view of the SQUID array.

fabricated and packaged, with appropriate connections made to a PCB launch using aluminum wire bonds (Fig. 4.6a). The on-chip flux line can also be used to apply a DC bias to the chip.

The experimental setup and design parameters are discussed in the following sections, followed by the measurement of gain as a function of pump power. The results demonstrate the effectiveness of the three-wave mixing process in achieving parametric amplification.

The design parameters are as follows for this JPA: SQUID loop inductance: $L_J \approx 0.51\,\text{nH}$, Total linear inductance: $L \approx 0.92\,\text{nH}$, DC external flux applied: $\phi/\phi_0 \approx 0.22$, Capacitance: $C \approx 1.08\,\text{pF}$, Resonant frequency: $\omega_0/2\pi \approx 4.338\,\text{GHz}$, Pump frequency: $\omega_p/2\pi \approx 8.676\,\text{GHz}$, Coupling capacitance: $C_c \approx 0.42\,\text{pF}$.

The amplifier is cooled to millikelvin temperatures in a dilution refrigerator to ensure superconducting operation (Fig. 4.6b). The input line includes approximately 60 dB of attenuation, while the pump line has about 50 dB. Both the input and output lines are equipped

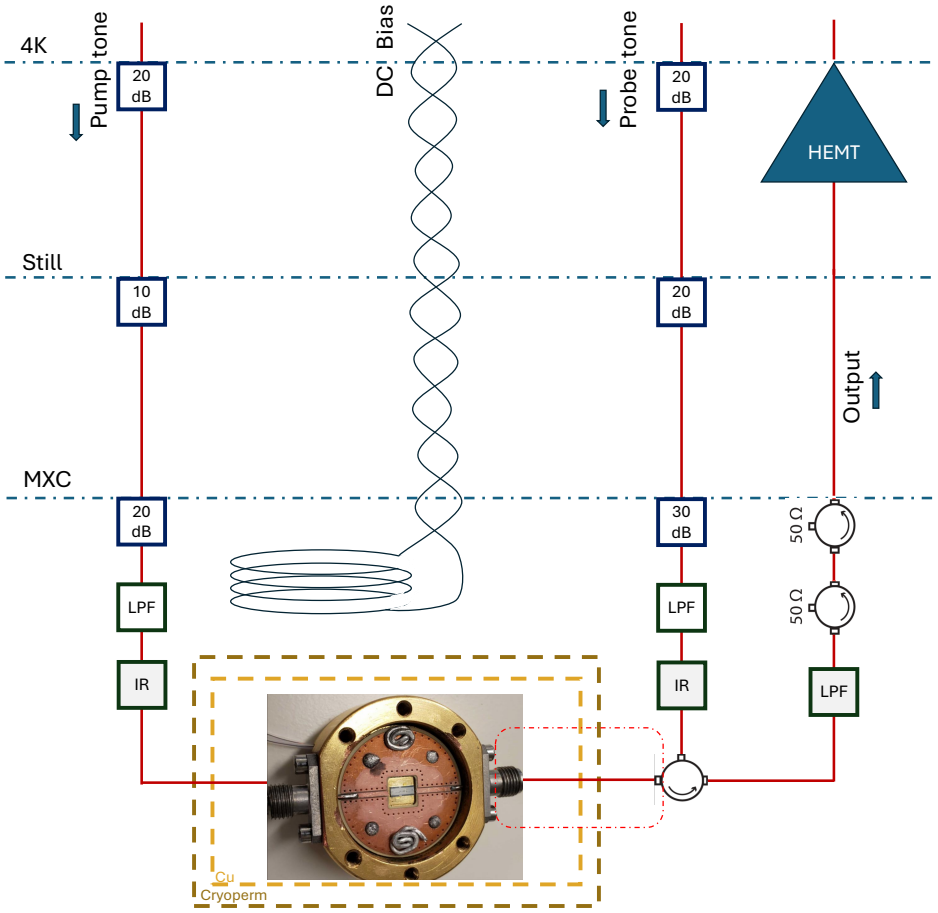

Fig. 4.6: Experimental setup: (a) Final wire-bonded chip inside a package. (b) Dilution-refrigerator setup for the measurement of the JPA.

with low-pass filters to suppress pump-tone leakage into the output path. The microwave cable between the JPA input and the circulator is kept as short as possible, since excessive cable length increases ripples caused by impedance mismatch. We then measure the S_{11} parameters of the amplifier around the resonance frequency. The input signal is applied at the resonance frequency, while the pump tone is applied at twice the resonance frequency to enable three-wave mixing.

The resulting gain response for different pump powers is shown in Fig. 4.7. The overall bandwidth achieved by this JPA was approximately 174 kHz. However, with careful

impedance-matching techniques, the bandwidth can be extended up to the GHz range in multipole-matched circuits.

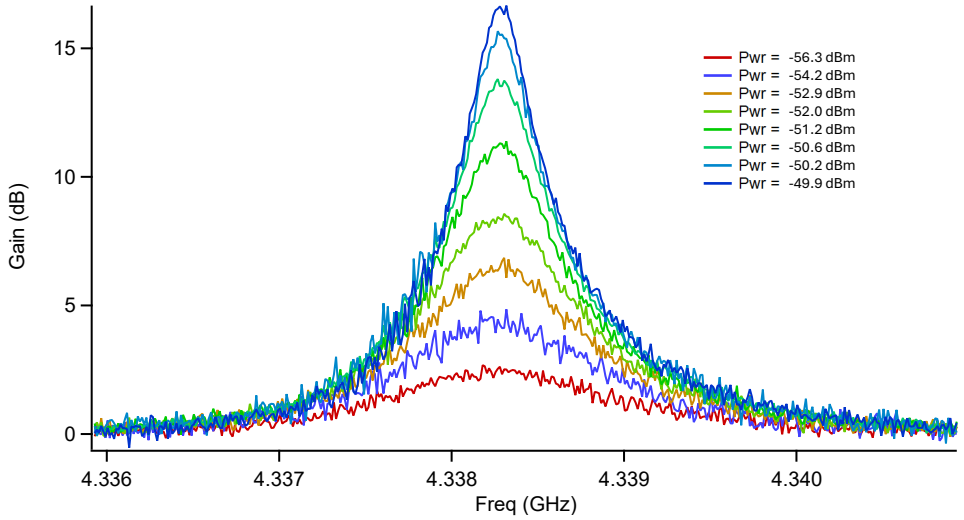

Fig. 4.7: Gain versus pump power for a flux-pumped parametric amplifier operating via three-wave mixing. The gain increases with pump power until it saturates at higher power levels. The solid line represents the theoretical prediction based on the Hamiltonian derived in Chapter 2.

Intuition

Here, we explore the intuitive workings of a parametric amplifier and how it amplifies a signal. As discussed in earlier sections, parametric amplification relies on **nonlinearity** to coherently convert pump photons into signal photons. This process is fundamental to achieving amplification in quantum systems and classical systems alike [92, 93].

Initially, when the signal strength is weak, the resonator plays a crucial role by providing the necessary delay for signal photons to become trapped and interact with the pump photons. This interaction is mediated by the nonlinear medium, which enables energy trans-

fer from the pump to the signal. These processes are governed by energy and momentum conservation laws, ensuring that the frequency and phase relationships between the pump, signal, and idler photons are preserved [99].

It is important to note that the reverse process is also possible: a signal photon and an idler photon can mix and upconvert into a pump photon. This upconversion process can stall the amplification if it becomes significant. However, in practice, the abundance of pump photons ensures that the downconversion process (amplification) dominates over upconversion. This dominance persists until the rates of upconversion and downconversion become comparable, at which point the amplification process begins to degrade.

4.4 How to Design a Good Amplifier

The first device we built demonstrated basic parametric gain but was far from optimal for practical use. In designing a JPA, three application-driven properties dominate:

1. **Instant tunability via DC flux.**
2. **Pump coupling efficiency.**
3. **Bandwidth allocation.**

Which of these you optimize depends on the target experiment. For example, some readout chains do not require large bandwidth but benefit from a very wide, fast tuning range; others must read out many qubits simultaneously and therefore demand GHz-scale bandwidth. Efficient pump coupling minimizes on-chip dissipation and eases thermal loading. Below we outline how each feature is tuned, with pros and cons, to make the trade-offs explicit [93, 94].

4.4.1 Tunability of a JPA

To understand the tunability and sensitivity of the JPA, we define the nonlinearity (Josephson participation of the inductance)

$$\eta \;\equiv\; \frac{L_J^*}{L_\ell}, \tag{4.41}$$

where L_ℓ is the linear (geometric) inductance and L_J^* sets the scale of the effective Josephson inductance. For a symmetric SQUID,

$$L_J(\Phi_{\text{ext}}) \;=\; \frac{L_J^*}{\left|\cos(\pi\Phi_{\text{ext}}/\Phi_0)\right|}, \tag{4.42}$$

so the total inductance is $L_{\text{tot}}(\Phi) = L_\ell + L_J(\Phi)$. With capacitance C, the mode frequency is

$$\omega(\Phi_{\text{ext}}) = \frac{1}{\sqrt{L_{\text{tot}}(\Phi_{\text{ext}})\,C}} = \frac{\omega_0}{\sqrt{1+\dfrac{\eta}{\left|\cos(\pi\Phi_{\text{ext}}/\Phi_0)\right|}}}, \qquad \omega_0 \equiv \frac{1}{\sqrt{L_\ell C}}. \tag{4.43}$$

Slope (sensitivity) to flux. Let $x \equiv \pi\Phi_{\text{ext}}/\Phi_0$ and, for $0 \le x < \pi/2$, drop the absolute value. From (4.43),

$$\frac{1}{\omega}\frac{d\omega}{d\Phi_{\text{ext}}} = -\frac{1}{2}\,\frac{\eta\,\sin x}{\cos^2 x}\,\frac{\pi/\Phi_0}{1+\eta/\cos x}. \tag{4.44}$$

At the commonly used bias $x = \pi/4$ ($\Phi_{\text{ext}} = \Phi_0/4$; $\sin x = \cos x = \frac{\sqrt{2}}{2}$),

$$\left|\frac{1}{\omega}\frac{d\omega}{d\Phi_{\text{ext}}}\right|_{\Phi_0/4} = \frac{\pi}{2\Phi_0}\,\frac{\eta\sqrt{2}}{1+\eta\sqrt{2}}. \tag{4.45}$$

Thus increasing η boosts tuning sensitivity near $\Phi_0/4$ but saturates to $\frac{\pi}{2\Phi_0}$ as $\eta \to \infty$.

Tuning range examples. The fractional frequency between two flux biases x_1, x_2 follows directly from (4.43):

$$\frac{\omega(x_2)}{\omega(x_1)} = \sqrt{\frac{1+\eta/\cos x_1}{1+\eta/\cos x_2}}. \tag{4.46}$$

Taking $x_1 = 0$ and $x_2 = \pi/3$ (i.e., $\cos x_2 = \frac{1}{2}$):

$$\frac{\omega(\pi/3)}{\omega(0)} = \sqrt{\frac{1+\eta}{1+2\eta}}. \tag{4.47}$$

Numerically,

$$\eta = 0.55: \quad \omega(\pi/3)/\omega(0) \approx 0.86 \quad (\sim 14\% \text{ drop}), \tag{4.48}$$

$$\eta = 4: \quad \omega(\pi/3)/\omega(0) = \sqrt{\tfrac{5}{9}} \approx 0.745 \quad (\sim 26\% \text{ drop}). \tag{4.49}$$

So pushing η from 0.55 to 4 yields substantially larger tunability over practical bias ranges (e.g., around $\Phi_0/4$–$\Phi_0/3$). Larger η increases the Josephson participation $p = L_J/(L_\ell + L_J) = \eta/(1+\eta)$, which strengthens the effective Kerr nonlinearity. While this improves tunability, it lowers the 1 dB compression power P_{1dB} (dynamic range degrades roughly as nonlinearity grows). One straightforward way to increase nonlinearity is to add more SQUID elements in series and use the inductance from the SQUID array (Fig. 4.8c) instead of the linear inductance of the resonator. Adopting a *fractal* capacitor also reduces the parasitic linear inductance introduced by the planar capacitor in the JPA design. In practice, η must be chosen to balance *tunability* against *compression* for the target application.

4.4.2 Current coupling vs. flux coupling

Parametric modulation in a JPA can be realized in two ways: *(i) flux pumping* away from zero flux bias to activate three-wave mixing (3WM), and *(ii) current (amplitude) pumping* near zero flux bias to activate four-wave mixing (4WM). Current-pumped devices often require no dedicated pump line: the strong pump tone is injected via the weak (signal) port and still yields gain through the Kerr (4WM) nonlinearity. By contrast, a flux-pumped device needs a separate line that couples *magnetically* (mutual inductance) into the SQUID loop to drive the 3WM process [93, 94]. Ideally, the flux line couples *purely inductively* to the SQUID array (no electric coupling to the resonator). In practice, stray capacitance between the flux line and the resonator is difficult (often impossible) to reduce to zero. The consequence is twofold: (i) the intended *flux* drive produces 3WM when biased away from zero flux; (ii) the unintended *capacitive* drive injects coherent current through both junction arms in the same direction, generating an AC Stark (Kerr) shift that detunes the JPA away from its chosen bias point. If the capacitive coupling dominates the flux coupling, the resonance shifts appreciably *before* appreciable gain develops, making calibration difficult and, in the extreme, the device unusable.

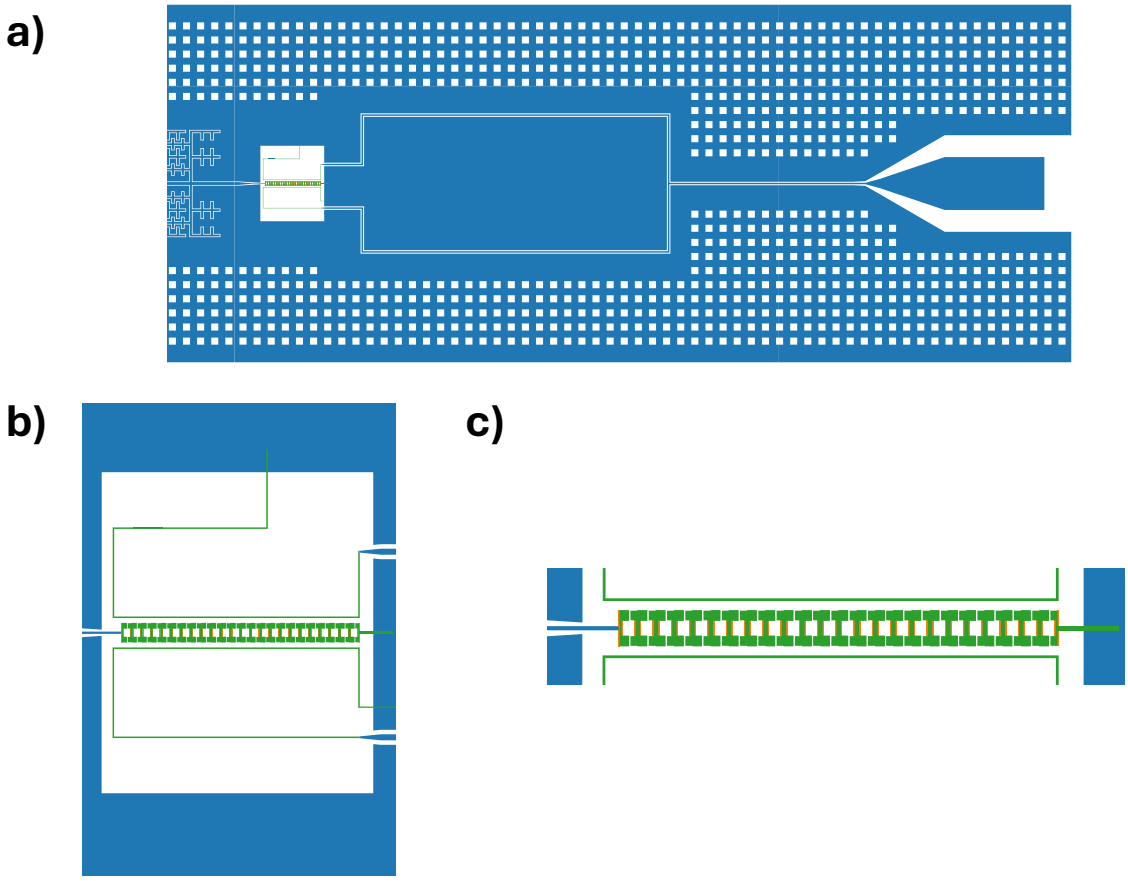

Fig. 4.8: Novel flux-line design. (a) Image of the split flux-line geometry. (b) Zoomed-in image of the flux line. (c) SQUID array.

Mitigation I: increase flux coupling (mutual inductance). A direct lever is to increase the mutual inductance M from the flux line to the SQUID loops. We adopted a split-flux-line design that wraps the line around the SQUID array (Fig. 4.8a,b), effectively doubling the loop linkage and boosting M. An additional advantage of the split geometry is interference control: by choosing the termination of the second arm appropriately, one can engineer destructive interference for resonator leakage through the pump path, reducing pump-line radiation loss.

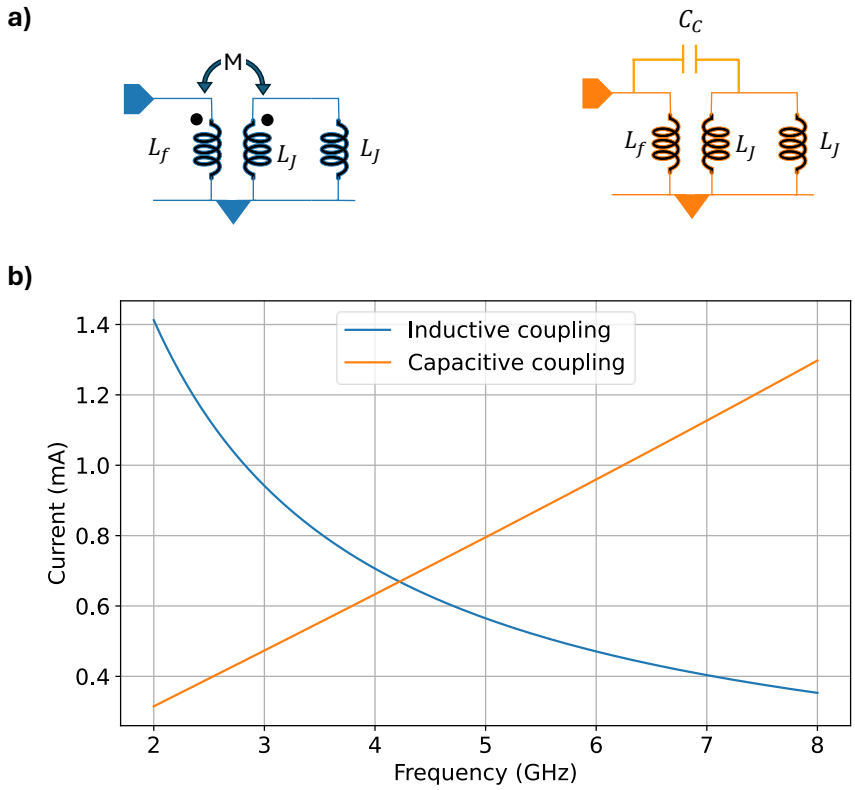

Fig. 4.9: Inductive vs. capacitive coupling. Schematic comparison of (left) purely inductive coupling and (right) purely capacitive coupling between the flux line and a SQUID arm. (c) Simulated current flowing in one SQUID inductor for capacitive (orange) and inductive (blue) coupling.

Mitigation II: reduce capacitive coupling. To suppress capacitive feedthrough, minimize the flux-line electrode area and its overlap with the resonator traces, increase separation, and avoid broad ground-referenced pads near the mode's voltage antinodes. A complementary tactic is to *float* the JPA resonator (no shared ground plane with the flux line), which strongly reduces parasitic capacitance between the line and the mode.

Consider the two limiting couplings sketched in Fig. 4.9a: purely inductive versus purely capacitive drive of one SQUID arm. With increasing frequency ω, $|Z_L| = \omega L$ grows while

$|Z_C| = 1/(\omega C)$ shrinks. Accordingly, the relative current (Fig. 4.9c) induced by capacitive feedthrough increases with ω, while the effectiveness of inductive (flux) drive diminishes. Above a device-specific crossover, capacitive injection inevitably dominates unless its parasitic coupling is made vanishingly small.

At microwave frequencies where capacitive feedthrough is hard to suppress, one can eliminate the flux line altogether and *embed the required 3WM asymmetry in the nonlinear element*. Asymmetric multi-junction loops (SNAILs) generate a strong cubic nonlinearity at a fixed DC flux; the amplifier is then pumped through the weak port near $2\omega_0$ (or $\omega_s + \omega_i$), achieving 3WM gain while avoiding a flux-line capacitive path [93, 94, 100]. This approach is therefore preferred for higher-frequency 3WM designs where maintaining purely inductive pump coupling is impractical.

4.4.3 Impedance-matching techniques

Up to this point, we have considered a simple Josephson parametric amplifier (JPA) consisting of a single resonator, coupled to the weak (reflection) port through a single coupling capacitor. In this basic configuration, the small-signal gain spectrum follows a Lorentzian response, characteristic of a first-order (single-pole) resonant system with loaded quality factor Q_{L} [101, 102]. A convenient single-pole transfer function is

$$H(\omega) \;=\; \frac{1}{1 + j\,\dfrac{\omega - \omega_0}{\kappa/2}}, \qquad |H(\omega)|^2 \;=\; \frac{1}{1 + 4\left(\dfrac{\omega - \omega_0}{\kappa}\right)^2}, \tag{4.50}$$

with resonance ω_0, total linewidth $\kappa = \omega_0/Q_{\mathrm{L}}$, and a Lorentzian power response.

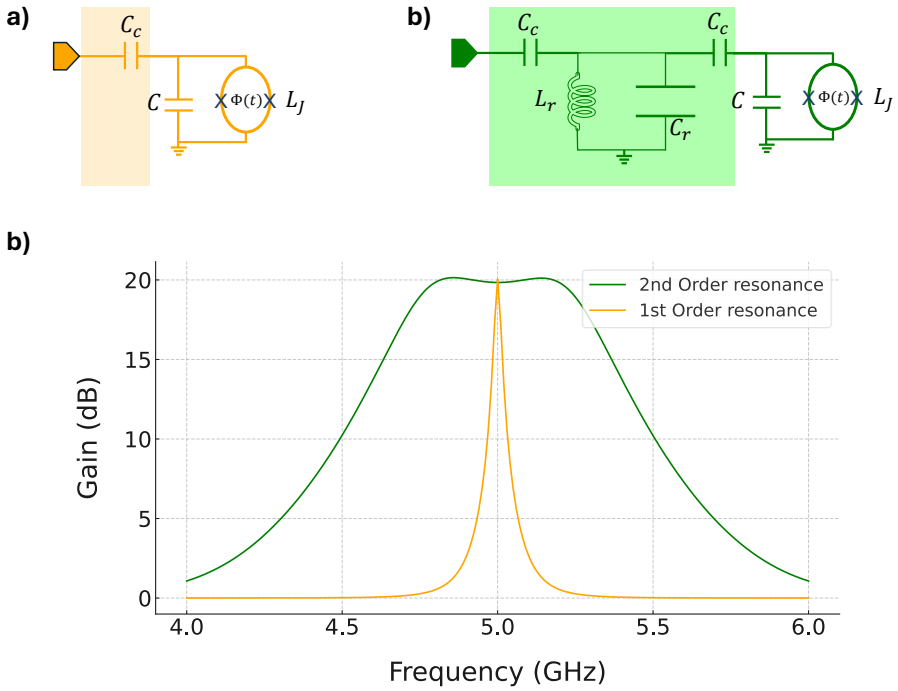

Fig. 4.10: Impedance-matched amplifier. (a) First-order JPA circuit. (b) Second-order JPA circuit. (c) Gain response of first-order (yellow) and impedance-matched (green) JPAs.

Impedance engineering with higher-order matching. Replacing the single coupling capacitor by a matching *resonator* raises the overall order from one pole to two poles. More generally, an N-pole network has

$$H(\omega) = \prod_{n=1}^{N} \frac{1}{1 + j\,\dfrac{\omega - \omega_n}{\kappa_n/2}}, \tag{4.51}$$

where the pole locations $\{\omega_n, \kappa_n\}$ can be engineered to yield a flatter passband and sharper skirts, closely paralleling classical microwave filter synthesis (e.g., Butterworth/Chebyshev

prototypes) [103–105]. In reflection-mode JPAs, such *impedance-engineered* matching networks (resonant or transformer-based) have been shown to expand instantaneous bandwidths while maintaining near-quantum-limited noise performance [106–108].

This bandwidth enhancement comes with a trade-off: to achieve the same peak gain at larger external coupling (lower Q_{L}), the required pump amplitude increases [101, 109]. Fundamentally, these trade-offs are consistent with Bode–Fano limits on matching reactive loads over a finite band [110–112].

Single-pole example. An example single-pole JPA resonator is shown in Fig. 4.10a, with

$$C_c = 146 \text{ fF}, \qquad C = 670 \text{ fF}, \qquad L_J = 0.9 \text{ nH}.$$

The corresponding gain response is plotted in Fig. 4.10c (yellow curve) and exhibits the expected Lorentzian shape.

Two-pole example with a matching resonator. Figure 4.10b illustrates a two-pole configuration in which an additional resonator is capacitively coupled to both the JPA resonator and the reflection port:

$$C_{c1} = 180 \text{ fF}, \quad C_{c2} = 330 \text{ fF}, \quad L_r = 1.68 \text{ nH}, \quad L_J = 0.9 \text{ nH}, \quad C_r = 325 \text{ fF}, \quad C = 325 \text{ fF}.$$

The resulting gain (green curve in Fig. 4.10c) displays a much broader, flatter top—approximately ~ 400 MHz of bandwidth versus ~ 10 MHz for the single-pole design—with a correspondingly higher pump requirement (about $\times 9$) to maintain similar peak gain, consistent with the reduced Q_{L} of the broadband match [105, 106].

Beyond two poles. By cascading additional resonant stages or using wideband transmission-line transformers (e.g., Ruthroff-type) to transform the effective source impedance seen by the nonlinear resonator, one can realize multi-pole responses with wide, well-controlled pass-bands and low ripple [103, 104, 113]. Such impedance-engineered JPAs are now routinely explored for broadband qubit readout and multiplexed measurements [105–108].

Conclusion In this chapter, we examined how amplification enables the detection of weak quantum signals and how its fundamental limits shape device performance. We showed that while phase-preserving amplifiers must add at least half a quantum of noise, phase-sensitive operation can amplify one quadrature without added noise.

We derived the classical gain and gain–bandwidth trade-off for parametric amplification and connected it to the quantum picture through three- and four-wave mixing processes. A practical flux-driven JPA was designed, fabricated, and measured to demonstrate these principles in experiment.

We also outlined key design trade-offs—tunability, pump coupling, and impedance engineering—that determine performance in real systems. These design considerations provide a flexible framework for tailoring JPAs to specific experimental requirements, from narrowband high-gain operation to broadband, impedance-matched amplification.

In the next chapter, we build on this foundation by using one of the devices developed here to explore **non-Hermitian physics in the quadrature space of the JPA**. By tuning gain, loss, and coupling parameters, the same parametric processes that enable amplification will be harnessed to study exceptional points and engineered gain–loss dynamics in a controlled superconducting platform.

Chapter 5

Non-Hermitian Systems and Parity–Time Symmetry

5.1 Introduction to Hermitian and Non-Hermitian Systems

In every closed system, due to its isolation, energy cannot be added to or removed from the system. Such systems are described by **Hermitian Hamiltonians**, which have real eigenvalues and conserve energy over time. The Hermitian property ensures that the system's dynamics are unitary, meaning the total probability is preserved, and the system evolves in a predictable and reversible manner [114].

A simple example of a Hermitian Hamiltonian is the two-level system

$$\hat{H}_{\text{Hermitian}} = \begin{pmatrix} E_1 & V \\ V^* & E_2 \end{pmatrix}, \tag{5.1}$$

where E_1 and E_2 are real energy levels, and V is the coupling between them with $V^* = V$ ensuring Hermiticity. Since $\hat{H}_{\text{Hermitian}} = \hat{H}^\dagger_{\text{Hermitian}}$, the eigenvalues are always real, repre-

senting physically observable energies, and the time-evolution operator $e^{-i\hat{H}t/\hbar}$ is unitary. However, in reality, no system is perfectly isolated. Every system is in fact a subsystem embedded within a larger environment, and interactions with this environment lead to energy exchange, dissipation, and decoherence. A Hermitian Hamiltonian can be assigned when the information decay rate is significantly smaller than the system's study timescale. For example, consider a qubit coupled to a readout resonator, as discussed in previous chapters. The qubit loses information due to dispersive coupling with the resonator, but if the Purcell limit (the rate at which the qubit decays into the resonator) is on the order of 1 ms, then for a fraction of that time (e.g., 100 μs) the qubit can be effectively described using a Hermitian Hamiltonian [5].

When the system's interaction time is comparable to its decay or gain timescale, the Hermitian description breaks down. In such cases, we assign a **non-Hermitian Hamiltonian** that includes appropriate decay and gain terms. Non-Hermitian Hamiltonians are characterized by complex eigenvalues, which reflect the system's dissipative or amplifying nature, and are broadly used to model open quantum systems where energy and information exchange with the environment is essential [43].

A canonical example is

$$\hat{H}_{\text{non-Hermitian}} = \begin{pmatrix} E_1 - i\gamma_1 & V \\ V^* & E_2 + i\gamma_2 \end{pmatrix}, \tag{5.2}$$

where $\gamma_1 > 0$ is the decay rate of the first level and $\gamma_2 > 0$ is the gain rate of the second level. Here $\hat{H}_{\text{non-Hermitian}} \neq \hat{H}^\dagger_{\text{non-Hermitian}}$, yielding complex eigenvalues whose imaginary parts describe exponential growth/decay of probability amplitudes.

Non-Hermitian systems are relevant across quantum optics, condensed matter physics,

and quantum information science. In quantum optics, they describe laser systems where gain and loss are central to coherent light generation [115]. In condensed matter, non-Hermitian models capture topological phases and exceptional points, where eigenvalues and eigenvectors coalesce, producing unique phenomena [116]. In quantum information, such models help capture decoherence and dissipation in qubits, enabling strategies to mitigate noise and improve device performance [93].

5.2 Parity–Time (PT) Symmetry

A PT-dimer is the simplest non-Hermitian system that still captures the key features of parity–time symmetry: two coupled modes with balanced gain and loss. This picture is a special case of the general two-level non-Hermitian model presented earlier (Fig. 5.1). The system is invariant under parity and time-reversal: parity swaps modes A and B, and time-reversal exchanges gain and loss. Under appropriate conditions, this special system yields a real eigenvalue spectrum. The region where the spectrum remains real is called the PT-symmetric region. PT symmetry was introduced as a compelling paradigm for non-Hermitian Hamiltonians that can nevertheless exhibit real spectra [117]. Originally developed in the context of complex potentials, PT symmetry has gained practical relevance with progress in optics [118].

Coupled-mode PT systems have been widely explored experimentally [119–125]. Of particular interest are exceptional points (EPs) [126, 127], which offer advantages such as enhanced sensitivity [**chen17**, 128, 129] and tuning capabilities [130]. Recent work has extended EP studies into the quantum domain, including superconducting circuits realizing passive PT symmetry with purely lossy dynamics [131–134], and Hamiltonian dilation approaches [135] implemented in platforms such as nitrogen-vacancy centers [136, 137].

In the quantum domain, amplification is constrained by the need to preserve operator commutation relations, leading to fundamental limits on added noise [93]. Dissipation-free gain—and thus noiseless amplification—is achievable via *squeezing*, wherein one quadrature is amplified while its conjugate is deamplified. In this chapter we realize a PT-dimer in such a dissipation-free setting [138], using a three-wave-mixing Josephson parametric amplifier (JPA) [102, 139, 140]. The two quadratures of an electromagnetic mode are mapped to the gain/loss modes of the PT-dimer, while detuning between pump and resonance couples the quadratures, enabling observation of PT symmetry breaking in the transient response. This opens a path to quantum microwave devices that exploit non-Hermiticity and EPs for non-reciprocity [141], enhanced sensing [142, 143], and exploration of topological quantum materials [144–148].

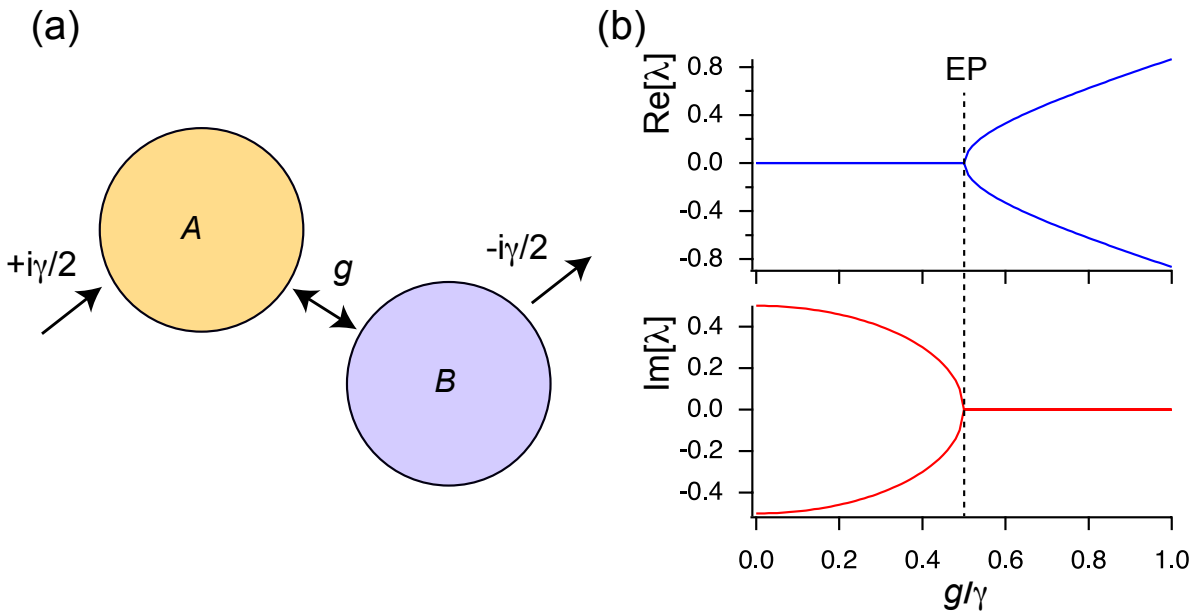

Fig. 5.1: The PT-dimer. (a) Two coupled modes with respective gain and loss. (b) Complex eigenvalue spectrum exhibiting a transition from purely imaginary to purely real eigenvalues separated by an exceptional point. For this plot, $\gamma = 1$.

5.2.1 The PT-Dimer Model

The PT-dimer consists of two coupled modes with equal and opposite gain/loss at rate $\gamma/2$. Under PT, parity swaps modes $A \leftrightarrow B$, and time-reversal exchanges gain and loss. Let the modes be coupled at rate g. The time evolution is

$$i\partial_t \begin{pmatrix} A \\ B \end{pmatrix} = H_{\mathrm{PT}} \begin{pmatrix} A \\ B \end{pmatrix}, \tag{5.3}$$

with

$$H_{\mathrm{PT}} = \begin{pmatrix} +i\frac{\gamma}{2} & g \\ g & -i\frac{\gamma}{2} \end{pmatrix} = g\sigma_x + i\frac{\gamma}{2}\sigma_z. \tag{5.4}$$

The eigenvalues are

$$\lambda_\pm = \pm\sqrt{g^2 - \left(\frac{\gamma}{2}\right)^2}, \tag{5.5}$$

revealing an "unbroken" PT-symmetric region ($g > \gamma/2$) with real eigenvalues and a "broken" region ($g < \gamma/2$) with purely imaginary eigenvalues. The exceptional point occurs at $g = \gamma/2$, where H_{PT} is not diagonalizable and the eigenvectors coalesce [Fig. 5.1(b)]. The tuning from real to imaginary spectra corresponds to the PT-symmetry-breaking transition. In the unbroken region, dynamics are oscillatory; in the broken region they amplify/deamplify according to gain/loss [131, 136]. Near the EP, eigenvalues are highly sensitive to the control parameter g [128, 149, 150]. The eigenvectors of Eq. (5.4) can be written as

$$|\pm\rangle \propto \begin{pmatrix} \lambda_\pm \\ g \end{pmatrix}, \tag{5.6}$$

which are generally nonorthogonal and coalesce at the EP. Introducing additional control parameters allows the eigenvalues to become complex (with both real and imaginary parts), producing a nontrivial Riemann surface. Encircling the EP leads to nonreciprocity [130] and chiral behavior [151].

5.3 Experimental Implementation with a Flux-Driven Josephson Parametric Amplifier

We utilize a JPA to realize the PT-dimer physics. JPAs leverage the nonlinearity of Josephson junctions to mix a strong classical pump with weak quantum signals [139]. They are widely used in circuit QED [5, 152] for quantum-noise-limited amplification and for exploring quantum nonlinear dynamics [153, 154].

We focus on three-wave mixing: one pump photon at ω_{p} converts into a signal ω_{s} and an idler ω_{i}, in the degenerate mode $\omega_{\mathrm{s}} = \omega_{\mathrm{i}} = \omega_{\mathrm{p}}/2$. In the rotating frame [155],

$$H_{\mathrm{DPA}} = \delta a^{\dagger} a + \frac{\nu}{2}\left(i a^{\dagger 2} - i a^{2}\right), \tag{5.7}$$

where $\delta \equiv (\omega_{\mathrm{p}}/2 - \omega_0)$ is detuning from the amplifier resonance ω_0, ν is the pump strength, and $a\,(a^{\dagger})$ is the annihilation (creation) operator at the signal frequency. The last two terms encode three-wave mixing between two signal photons and one pump photon; the pump is treated as classical.

5.3.1 Connection to the PT-Dimer Hamiltonian

Although the system is a single bosonic mode, a and $a^\dagger$ couple via the parametric drive. Define the vector $|a\rangle = (a, a^\dagger)^T$. The Heisenberg equations are

$$\partial_t a^\dagger(t) = i[H_{\mathrm{DPA}}, a^\dagger(t)] = i\delta a^\dagger + \nu a, \tag{5.8}$$

and

$$\partial_t a(t) = i[H_{\mathrm{DPA}}, a(t)] = -i\delta a + \nu a^\dagger. \tag{5.9}$$

Collecting terms,

$$i\partial_t |a\rangle = \begin{pmatrix} \delta & i\nu \\ i\nu & -\delta \end{pmatrix} |a\rangle . \tag{5.10}$$

Transform to quadratures $I = (a + a^\dagger)/\sqrt{2}$ and $Q = (a - a^\dagger)/(i\sqrt{2})$, with

$$\begin{pmatrix} I \\ iQ \end{pmatrix} = \frac{1}{\sqrt{2}} \begin{pmatrix} 1 & 1 \\ 1 & -1 \end{pmatrix} \begin{pmatrix} a \\ a^\dagger \end{pmatrix} \equiv S \begin{pmatrix} a \\ a^\dagger \end{pmatrix} . \tag{5.11}$$

Substituting into Eq. (5.10) yields

$$i\partial_t \begin{pmatrix} I \\ iQ \end{pmatrix} = \begin{pmatrix} i\nu & \delta \\ \delta & -i\nu \end{pmatrix} \begin{pmatrix} I \\ iQ \end{pmatrix} . \tag{5.12}$$

This evolution matrix realizes the PT-dimer Hamiltonian: the pump provides coherent gain/loss and the detuning provides coupling. A PT transition occurs at $|\delta| = |\nu|$. For $|\delta| > |\nu|$ the dynamics are oscillatory (unbroken PT), while for $|\delta| < |\nu|$ one quadrature amplifies and the other is squeezed (broken PT).

5.3.2 Simulated Results for the Three-Wave-Mixing Process

The time-evolution response of the Hamiltonian in Eq. (5.7) provides a clear framework for what to measure and how to analyze the experimental results. It also connects the PT-dimer picture of three-wave mixing to the JPA amplification mechanism [156]. In practice, a weak signal is coupled to the device to measure the output response. The flux line and the weak measurement port act as decay channels; together with other dissipation, these are captured by a Lindblad operator $\sqrt{\kappa}\, a$ [157]. For the device studied, we use $\kappa/2\pi \approx 0.19$ MHz, directly obtained from measurements discussed later. Eq. (5.7) is written in the rotating-wave approximation, and does not explicitly depend on the bare resonator frequency. The control parameters are the pump amplitude ν and the detuning δ between the probe and the resonator frequency. The pump frequency is twice the drive tone.

$$H = \delta a^\dagger a + i\frac{\nu}{2}\left(a^{\dagger 2} - a^2\right) - \chi a^{\dagger 2} a^2 + i\beta\left(a^\dagger - a\right). \tag{5.13}$$

Here χ is the self-Kerr nonlinearity and β is the probe strength. Since χ is typically small compared to the three-wave-mixing term, we set $\chi = 0$ for simulation simplicity. The simulation is initialized in the ground state $|\psi(0)\rangle = |0\rangle$. At $t = 0$ the input drive and pump are turned on. As time evolves, we compute $|\psi(t)\rangle$ and evaluate

$$I(t) = \langle\psi(t)|\,\hat{I}\,|\psi(t)\rangle\,, \qquad Q(t) = \langle\psi(t)|\,\hat{Q}\,|\psi(t)\rangle\,, \qquad n(t) = \sqrt{I^2(t) + Q^2(t)}.$$

An example input and the corresponding evolution of $I(t)$ is shown in Fig. 5.2 for zero pump and several detunings δ. We observe oscillations in the trajectories when the detuning is non-zero. These oscillations appear as the signal and pump tone are turned on, and the system eventually reaches a steady state, as shown in Fig. 5.2. In contrast, when the

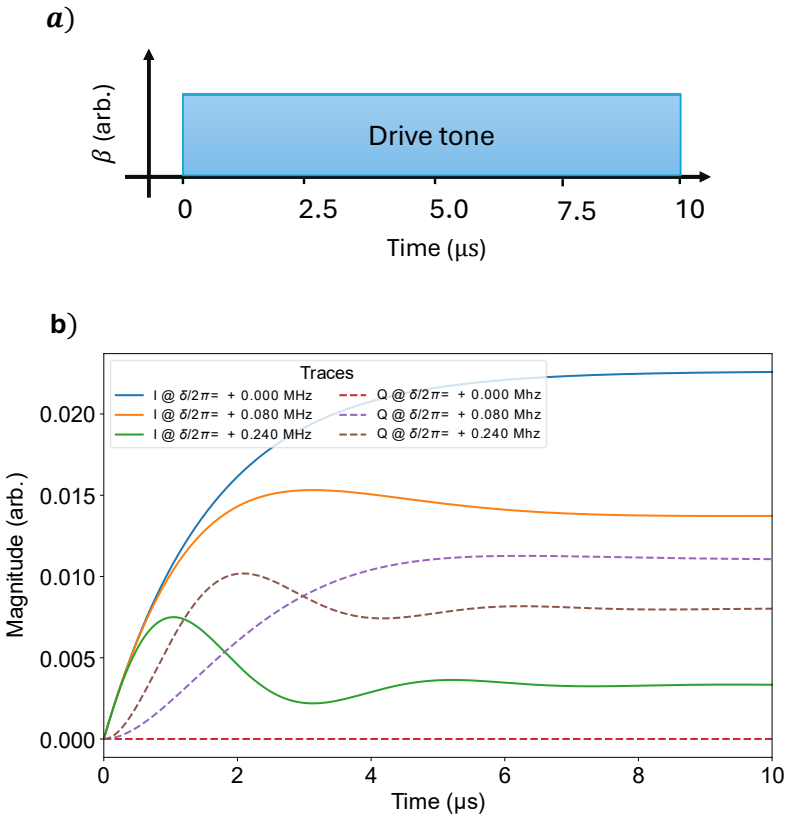

Fig. 5.2: Simulated time evolution of quadratures. (a) Pulse scheme: pump and probe are turned on simultaneously and held for 10 μs. (b) Simulated evolution of I and Q for several δ with zero pump amplitude $\nu/2\pi = 0.0$ MHz.

detuning is set to zero, the quadrature amplitudes reach their steady-state values without any oscillations. This behavior indicates that the $\mathcal{PT}$-dimer physics manifests primarily in the transient response of the signal [156].

With introduction of a pump ($\nu/2\pi = 0.095$ MHz), the quadrature response changes markedly: the amplitudes grow at zero detuning and for some nonzero detunings, indicating imaginary parts of the eigenvalues and amplification—i.e., PT-symmetry breaking. To visualize this, Fig. 5.3 shows colormaps of $I(t)$ vs. detuning and representative I–Q trajecto-

ries. At zero detuning, trajectories are straight lines because the coupling between $\hat{I}$ and $\hat{Q}$ vanishes, keeping the I quadrature phase-aligned. For nonzero detuning, $\hat{I}$ and $\hat{Q}$ exchange population at a rate set by the eigenvalues, producing spiral trajectories that later saturate. Such "curly'' patterns correspond to real eigenvalues, while straight, exponentially growing traces indicate imaginary eigenvalues.

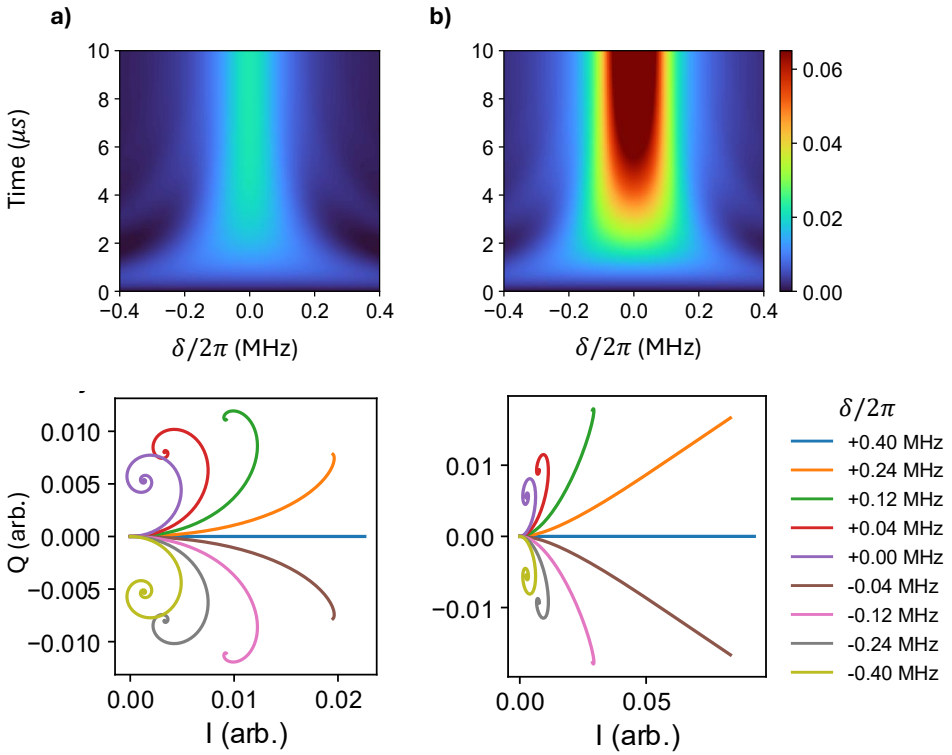

Fig. 5.3: Color map and I–Q trajectories. (a) Top: $I(t)$ over a sweep of δ with $\nu/2pi = 0$. Bottom: $I(t)$ vs. $Q(t)$ at representative detunings. (b) Same for $\nu/2\pi = 0.095$ MHz.

To quantify this behavior, we fit $I(t)$ to

$$A(t) = A_0 e^{-\alpha t} \sin(\omega t + \phi) + A_1, \tag{5.14}$$

extracting the oscillation frequency versus detuning. Nonzero fitted ω indicates a nonzero

real part of the eigenvalue; $\omega = 0$ with nonzero growth/decay indicates a purely imaginary eigenvalue. Figure 5.4 shows the extracted frequencies for pump-on and pump-off conditions. In the pump-on case, a frequency gap appears around zero detuning that widens with pump strength, indicating an expanding PT-broken region. The same behavior is visible in the I–Q trajectories: oscillatory (curly) traces for pump-off straighten and grow exponentially with pump-on.

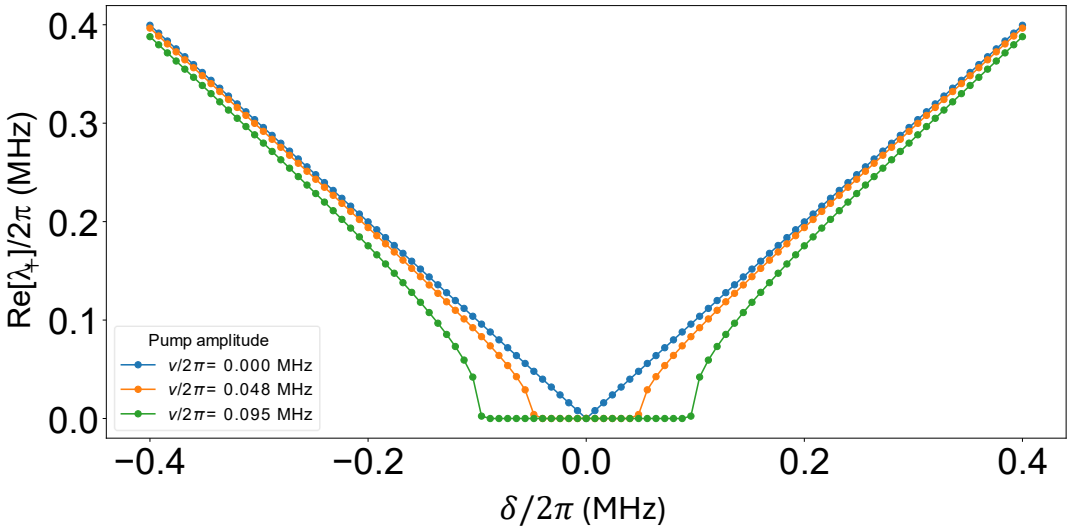

Fig. 5.4: Extracted eigenvalues from simulation. Frequency extracted from the time evolution of $I(t)$ for three pump amplitudes.

This comparison highlights the behavior expected experimentally. The model provides a quantitative framework for extracting eigenvalues and interpreting the JPA response as a PT-dimer realized via three-wave mixing. Beyond this device, the analysis illustrates how non-Hermitian systems can be used as sensors near exceptional points [158]. In the pump-on case, the oscillation frequency versus detuning departs from the linear pump-off response and follows a quadratic dependence near the exceptional point, characteristic of the EP order.

5.3.3 Device Design and Characterization

The Hamiltonian above ideally describes an amplifier operating via three-wave mixing. To probe the associated physics, an experimental device requires input and output ports to inject probe signals and monitor quadrature dynamics via a weakly coupled output. Formally,

$$a_{\mathrm{out}} = \sqrt{\kappa_{\mathrm{out}}}\, a,$$

where κ_{out} is the coupling rate to the output port. Hence, the output quadratures $(I_{\mathrm{out}}, Q_{\mathrm{out}})$ are proportional to the intracavity quadratures (I, Q) [159]. Because the output port introduces dissipation, the dynamics manifest strongly in the transient response; thus a high-Q amplifier is advantageous.

A narrow-bandwidth three-wave-mixing amplifier was designed. It is similar to the flux-driven JPA in previous chapters, but with a significantly smaller coupling capacitance to enhance the transient response. Figure 5.5a shows an EM layout of the device (inset: reduced coupling capacitor). The equivalent circuit schematic (Fig. 5.5b) comprises $C_{\mathrm{a}} = 1.085$ pF, $L_{\mathrm{a}} = 0.92$ nH, and $L_{\mathrm{J}} = 0.516$ nH. Coupling to a 50 Ω port through $C_{\mathrm{c}} = 84$ fF yields a resonance of 4.028 GHz (zero flux) with quality factor 2.0×10^4. L_{J} is realized as an array of four SQUIDs, each with loop area 5.5×5 μm^2 and critical current 3.2 μA. A high-bandwidth input line is coupled to the SQUID array with mutual inductance 80 pH to modulate L_{J} at twice the amplifier frequency; residual capacitive coupling allows weak probe injection [160].

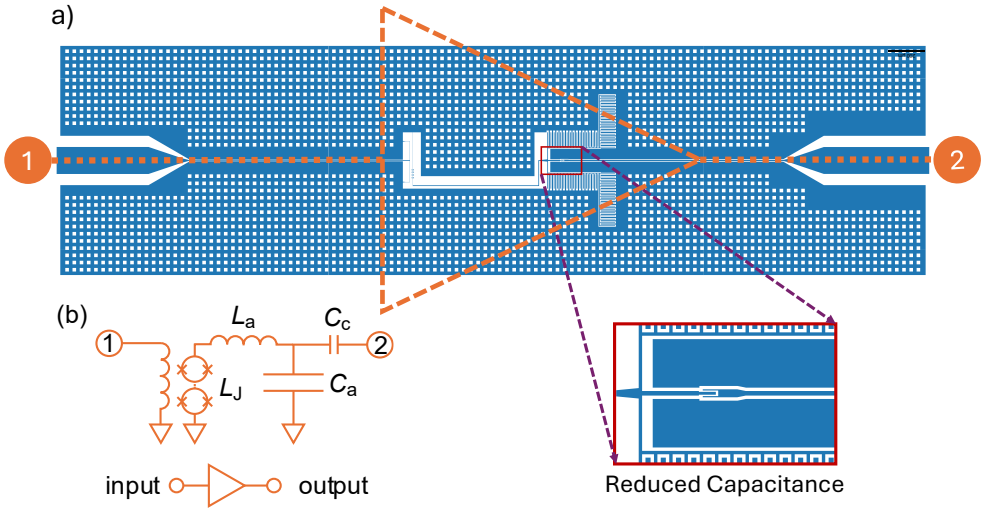

Fig. 5.5: Degenerate parametric amplifier. (a) EM layout of the device (inset: reduced coupling capacitor). (b) Circuit schematic; the input port provides pump/probe coupling and the output port monitors dynamics.

The device is wire-bonded to a microwave circuit board, cooled to 20 mK, and shielded from stray magnetic flux and radiation. The pump port is filtered and attenuated (total ∼50 dB). The cryogenic setup (Fig. 5.6) is similar to that in the previous chapter; both the weak probe and pump tones are applied to the flux-pump line, while the output is measured at the weakly coupled port. Transmission measurements ensure detected photons have interacted with the JPA; the weak input coupling complicates reflection measurements. The output passes through two cryogenic circulators and a 4 K HEMT amplifier. A DC flux bias of $\Phi_0/6$ is applied via an external superconducting coil, establishing linear coupling between pump and amplifier and enabling pump-driven modulation of L_J.

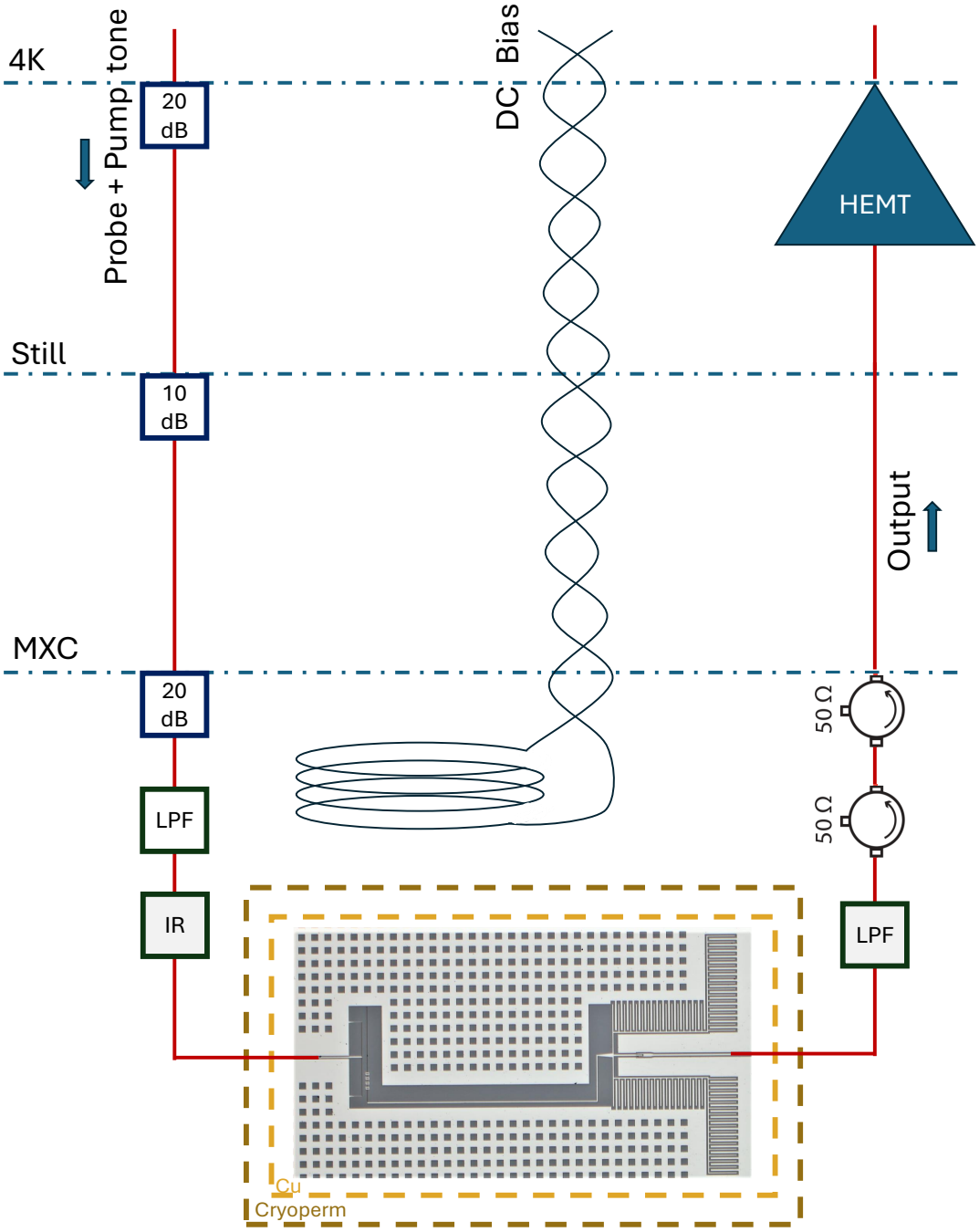

Fig. 5.6: Fridge setup. Schematic of the cryogenic wiring used in the PT-dimer experiment.

We first characterize the frequency response. Figure 5.7 shows (a) frequency modulation of the JPA due to flux coupling and (b) transmission with pump off (baseline) and pump on (gain ~ 4.2 dB). The resonance peak is clearly visible, and the gain appears as enhanced transmission above the baseline [161].

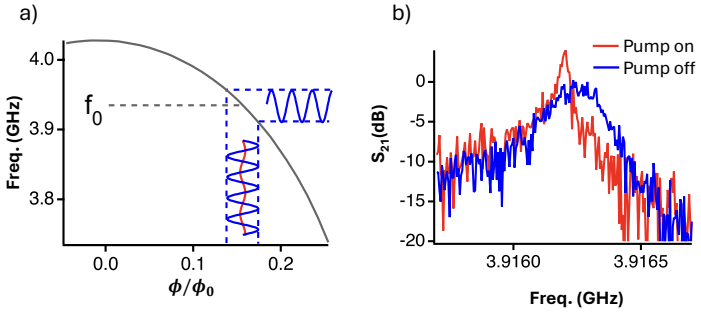

Fig. 5.7: Frequency response. (a) Frequency modulation of the JPA under flux drive. (b) Transmission with pump off/on; gain ~ 4.2 dB.

5.4 Time-Domain Measurements

The experiment should reproduce the simulated behavior. Because the input probe is extremely weak, we average over long acquisition times with repeated measurements. Each run requires the probe and pump to start with the same relative phase; otherwise, operating in degenerate mode, phase averaging would wash out the distinction between I and Q. The phase-locking scheme is shown in Fig. 5.8. Two independent generators provide pump and probe. The probe frequency is detuned by $\Delta = 5$ MHz from $\omega_p/2$. Both sources are split to create a common trigger. The post-split probe is frequency-doubled and bandpass filtered to isolate the second harmonic, then mixed with the post-split pump (mixer "A"), generating a 10 MHz tone used as the external trigger. The remaining probe is upconverted by single-sideband modulation back to exactly $\omega_p/2$ (mixer "B"), which also sets the pump–probe

phase. The pump is gated by a DC square pulse (mixer "C"). The upconverted probe and pump are combined with a directional coupler and sent to the flux-pump port. Signals transmitted through the amplifier are demodulated at $\omega_s - \Delta$ (mixer "D") for heterodyne detection.

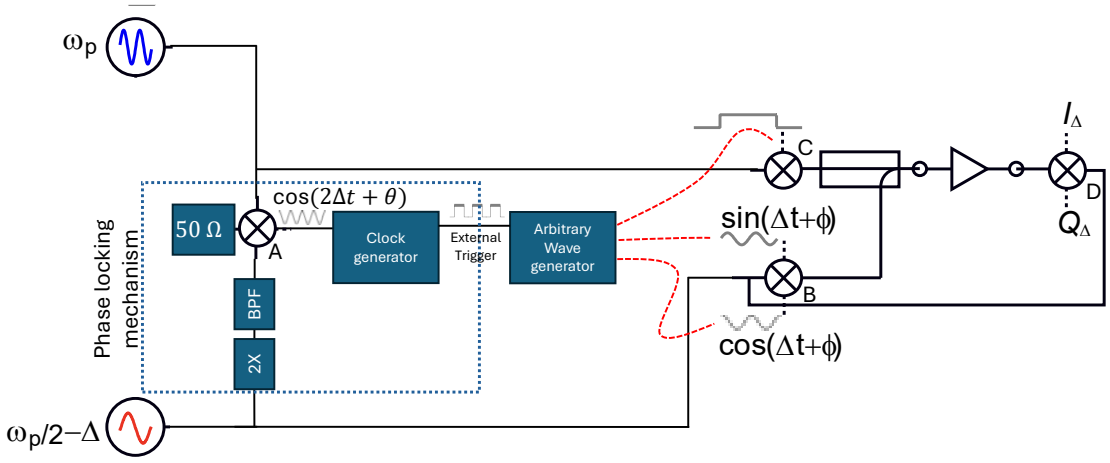

Fig. 5.8: Microwave setup. The probe is phase-locked to the pump (dashed box). Single-sideband modulation sets $\omega_s = \omega_p/2$. The output is demodulated.

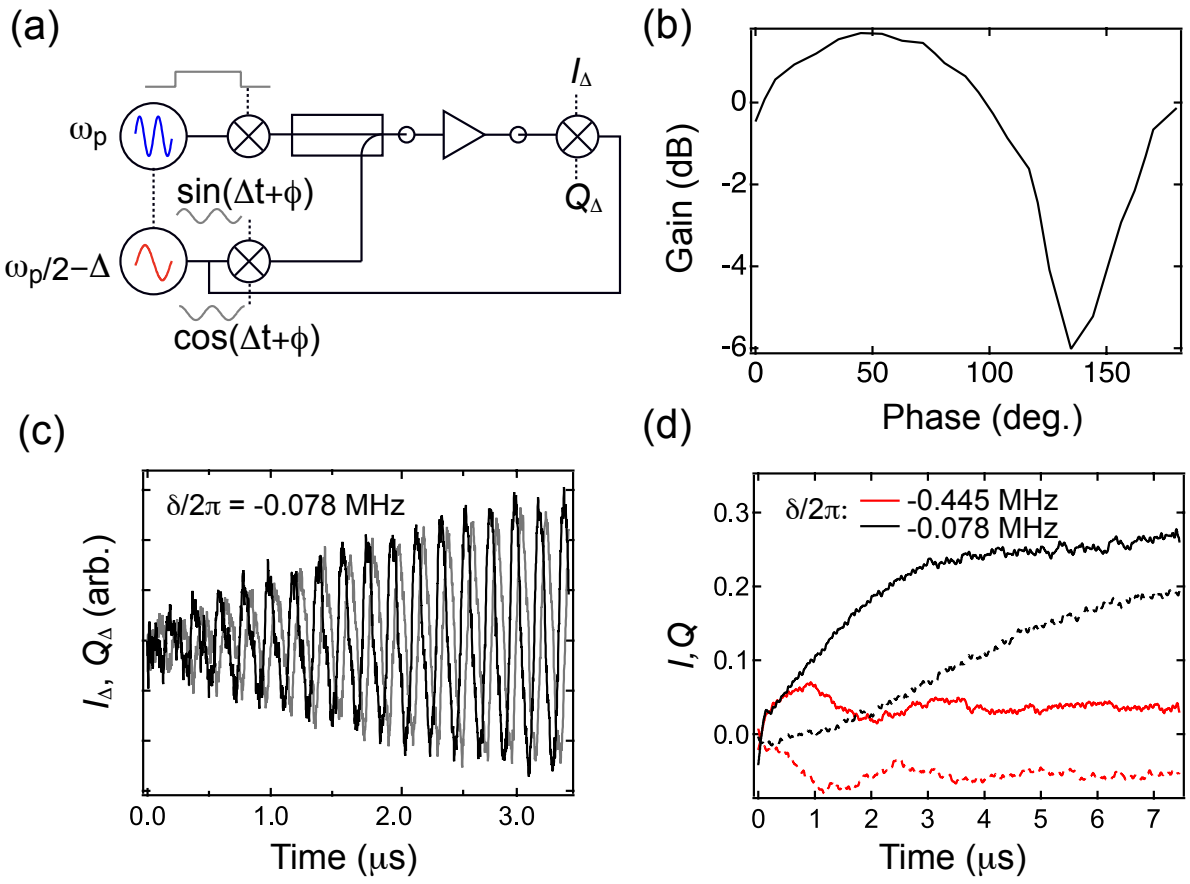

Fig. 5.9: Time-domain measurements. (a) Phase-sensitive response: sweeping probe phase shows amplification of one quadrature and squeezing of the orthogonal one. (b) Time-domain response of I_Δ and Q_Δ when probe and pump are turned on simultaneously; further demodulation yields I and Q. (c) Time evolution of I (solid) and Q (dashed) for three detunings.

Operating in degenerate mode ($2\omega_s = \omega_p$) yields inherently phase-sensitive amplification: in-phase signals are amplified, while quadrature signals are deamplified [162]. Figure 5.9(a) demonstrates phase-sensitive gain and validates the phase lock. In our experiments we fix the phase offset at $\phi_0 = 45°$ to amplify the input and achieve the required SNR.

Figure 5.9(b) shows a representative time trace. At $t = 0$, probe and pump are enabled, and the demodulated quadratures exhibit an exponentially varying envelope modulated at $\Delta/2\pi = 5$ MHz. Further demodulation yields I and Q, smoothed with a Savitzky–Golay filter (500 ns window, polynomial order 5). Figure 5.9(c) displays I and Q versus time for different detunings, showing a crossover from oscillatory to exponentially saturating behavior—marking the onset of PT-symmetry breaking.

5.5 Observation of PT-Symmetry-Breaking Transition

Figure 5.10 shows I versus detuning for three pump strengths. At low pump [Fig. 5.10(a)], we observe oscillations with frequency set by detuning, as expected when eigenvalues track detuning (cf. Eq. 5.5). Increasing the pump [Fig. 5.10(b,c)] produces a clear transition from oscillatory to non-oscillatory behavior as $|\delta|$ decreases. The I–Q plots (bottom panels) show alternating regions of oscillatory and non-oscillatory dynamics depending on detuning.

The data agree with a model that includes self-Kerr nonlinearity and a probe drive:

$$H = \delta a^\dagger a + i\frac{\nu}{2}\left(a^{\dagger 2} - a^2\right) - \chi a^{\dagger 2} a^2 + i\beta\left(a^\dagger - a\right). \tag{5.15}$$

Dissipation through the output port is modeled via a Lindblad term $\sqrt{\kappa}\, a$ with $\kappa/2\pi = 0.19$ MHz, determined from the device quality factor.

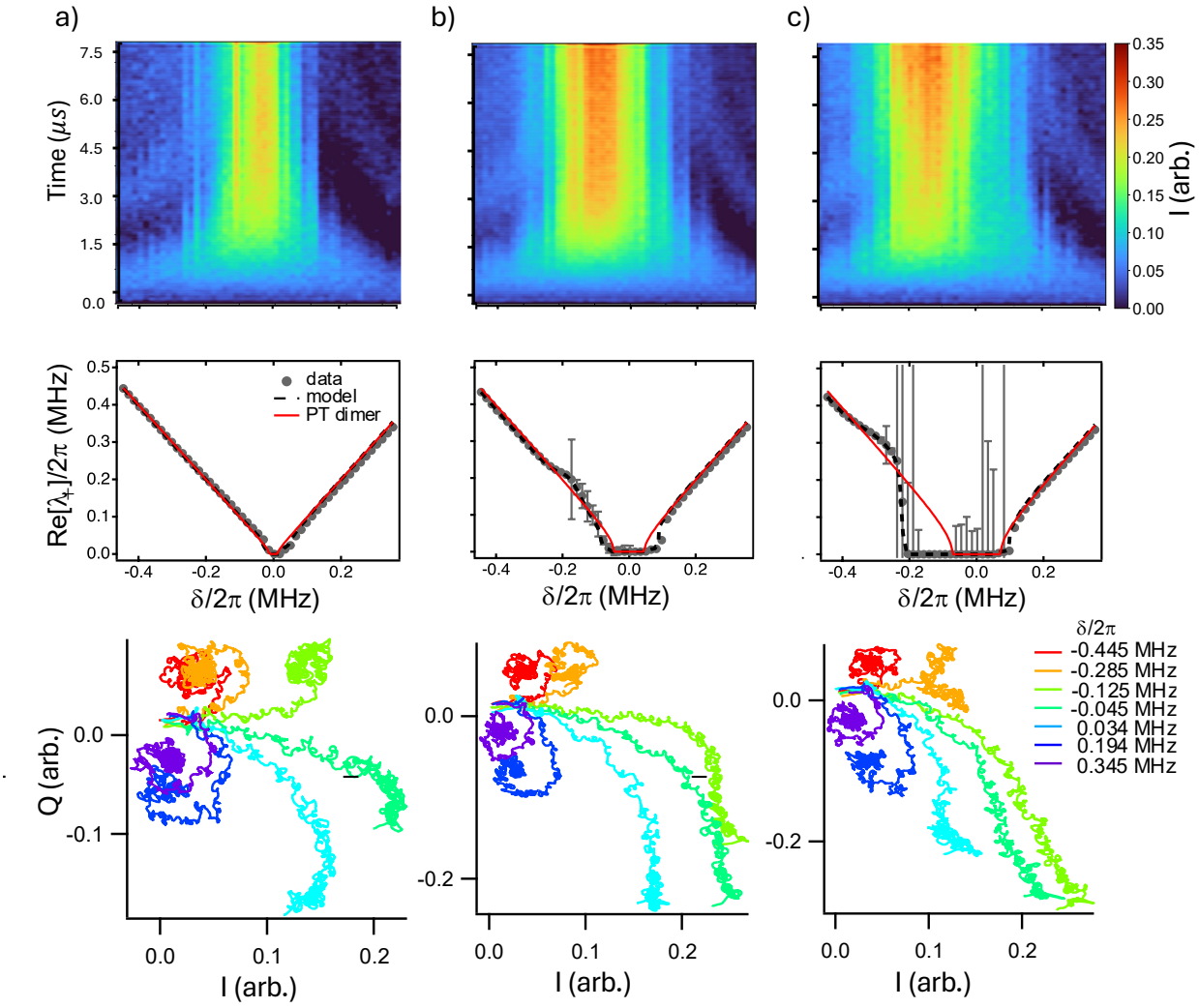

Fig. 5.10: PT-symmetry breaking in a parametric amplifier. Top row: $I(t)$ versus detuning for three pump strengths $\nu/2\pi = 0.013$ (a), 0.046 (b), and 0.072 (c) MHz. Middle row: extracted frequencies from measured $I(t)$ (dots), model (dashed), and ideal PT-dimer eigenvalues (solid red). Bottom row: representative $I(t)$–$Q(t)$ trajectories ("curly" plots).

We use QuTiP [163, 164] to compute the time evolution of I and Q for different detunings. The input drive and three-wave mixing are turned on at $t = 0$. From $I(t)$ we fit Eq. (5.14) to obtain ω, displayed in the middle panels; the same analysis is applied to data with initial guesses from the model. Fits with α and ω of similar magnitude can be weakly constrained (large fit errors), so the analysis demonstrates consistency with the model rather than precise parameter extraction. We tune χ to best match experiment, yielding $\chi/2\pi \approx 0.095$ MHz and pump strengths $\nu/2\pi = 0.013$, 0.046, and 0.072 MHz. For comparison, we plot the ideal PT-dimer eigenvalues using the model-extracted ν.

An asymmetry about zero detuning arises from the self-Kerr term, which always lowers the resonance, dominating at negative detuning. In the ideal PT-dimer, a second-order transition is expected at the EP; with self-Kerr included, a sharper transition is observed, suggesting richer dynamics and possibly higher-order effects. Future work can improve SNR by adding a wider-band JPA as a preamplifier for the PT-dimer JPA. Because most physics occurs in the transient state, increasing the Q further will extend the transient; however, higher Q reduces saturation power, so maintaining a sufficiently weak probe may require a quantum-limited post-amplifier. With these improvements, we aim to probe quantum correlations and entanglement in the output modes [138], while adopting strategies to reduce self-Kerr [165].

Conclusion This experiment establishes a connection between the transient dynamics of Josephson parametric amplifiers and the PT-symmetry-breaking transition. In optics, PT symmetry and exceptional points have motivated a broad range of devices and functionalities. Extending EP physics to Josephson circuits invites studies of quantum correlations and noise near EPs, with potential applications in sensing and quantum information processing.

Bibliography

1. Nielsen, M. A. & Chuang, I. L. *Quantum Computation and Quantum Information* 10th Anniversary (Cambridge University Press, 2010).
2. Preskill, J. Quantum Computing in the NISQ era and beyond. *Quantum* **2,** 79 (2018).
3. Devoret, M. H. & Schoelkopf, R. J. Superconducting Circuits for Quantum Information: An Outlook. *Science* **339,** 1169–1174 (2013).
4. Josephson, B. D. Possible new effects in superconductive tunnelling. *Physics Letters* **1,** 251–253 (1962).
5. Blais, A., Grimsmo, A. L., Girvin, S. M. & Wallraff, A. Circuit quantum electrodynamics. *Reviews of Modern Physics* **93,** 025005 (2021).
6. Barone, A. & Paternò, G. *Physics and Applications of the Josephson Effect* (Wiley, 1982).
7. Clarke, J. & Braginski, A. I. *The SQUID Handbook: Applications of SQUIDs and SQUID Systems* (Wiley-VCH, 2006).
8. Tinkham, M. *Introduction to Superconductivity* 2nd ed. (McGraw-Hill, 1996).
9. Likharev, K. K. Dynamics of Josephson Junctions and Circuits. *Gordon and Breach* (1986).
10. Koch, J. *et al.* Charge-insensitive qubit design derived from the Cooper pair box. *Phys. Rev. A* **76,** 042319 (2007).
11. Devoret, M. H. & Schoelkopf, R. J. Superconducting circuits for quantum information: an outlook. *Science* **339,** 1169–1174 (2013).
12. You, J. Q. & Nori, F. Atomic physics and quantum optics using superconducting circuits. *Nature* **474,** 589–597 (2011).
13. Abramowitz, M. & Stegun, I. A. *Handbook of Mathematical Functions* (Dover, 1964).
14. Koch, J. *et al.* Charge-insensitive qubit design derived from the Cooper pair box. *Phys. Rev. A* **76,** 042319 (2007).
15. Pozar, D. M. *Microwave Engineering* 4th ed. (Wiley, 2011).

16. Houck, A. A. *et al.* Controlling the spontaneous emission of a superconducting transmon qubit. *Phys. Rev. Lett.* **101,** 080502 (2008).

17. Martinis, J. M., Nam, S., Aumentado, J. & Urbina, C. Decoherence in Josephson Qubits from Dielectric Loss. *Phys. Rev. Lett.* **95,** 210503 (2005).

18. Müller, C., Cole, J. H. & Lisenfeld, J. Towards understanding two-level-systems in amorphous solids. *Rep. Prog. Phys.* **82,** 124501 (2019).

19. Blais, A., Huang, R.-S., Wallraff, A., Girvin, S. M. & Schoelkopf, R. J. Cavity quantum electrodynamics for superconducting electrical circuits: An architecture for quantum computation. *Phys. Rev. A* **69,** 062320 (2004).

20. Krantz, P. *et al.* A quantum engineer's guide to superconducting qubits. *Applied Physics Reviews* **6,** 021318 (2019).

21. Gambetta, J. *et al.* Qubit-photon interactions in a cavity: Measurement-induced dephasing and number splitting. *Phys. Rev. A* **74,** 042318 (2006).

22. Blais, A., Grimsmo, A. L., Girvin, S. M. & Wallraff, A. Circuit quantum electrodynamics (Review Article). *Rev. Mod. Phys.* **93,** 025005 (2021).

23. Barends, R., Kelly, J., Megrant, A. & et al. Superconducting quantum circuits at the surface code threshold for fault tolerance. *Nature* **508,** 500–503 (2014).

24. Arute, F., Arya, K., Babbush, R. & et al. Quantum supremacy using a programmable superconducting processor. *Nature* **574,** 505–510 (2019).

25. Didier, N., Bourassa, J. & Blais, A. Parametrically Activated Entangling Gates Using Transmon Qubits. *Phys. Rev. Lett.* **115,** 203601 (2015).

26. Caldwell, S. A. & et al. Parametrically Activated Entangling Gates Using Transmon Qubits. *Phys. Rev. Applied* **10,** 034050 (2018).

27. *NIST Digital Library of Mathematical Functions* `https://dlmf.nist.gov/`. Jacobi–Anger expansions and Bessel function identities.

28. Reagor, M. & et al. Demonstration of universal parametric entangling gates on a multi-qubit lattice. *Science Advances* **4,** eaao3603 (2018).

29. Nielsen, M. A. & Chuang, I. L. *Quantum Computation and Quantum Information* (Cambridge University Press, 2000).

30. Bell, J. S. On the Einstein Podolsky Rosen paradox. *Physics* **1,** 195–200 (1964).

31. Clauser, J. F., Horne, M. A., Shimony, A. & Holt, R. A. Proposed experiment to test local hidden-variable theories. *Phys. Rev. Lett.* **23,** 880–884 (1969).

32. Aspect, A., Grangier, P. & Roger, G. Experimental Realization of Einstein-Podolsky-Rosen-Bohm Gedankenexperiment: A New Violation of Bell's Inequalities. *Phys. Rev. Lett.* **49,** 91–94 (1982).

33. Hensen, B., Bernien, H., Dréau, A. E. & et al. Loophole-free Bell inequality violation using electron spins separated by 1.3 kilometres. *Nature* **526,** 682–686 (2015).

34. Nielsen, M. A. & Chuang, I. L. *Quantum Computation and Quantum Information: 10th Anniversary Edition* (Cambridge University Press, Cambridge, 2010).

35. Chow, J. M., Gambetta, J. M., Cross, A. W. & et al. *Simple All-Microwave Entangling Gate for Fixed-Frequency Superconducting Qubits* in *APS March Meeting* (2011).

36. Yan, F., Sung, Y., Krantz, P. & et al. Tunable Coupling Scheme for Implementing High-Fidelity Two-Qubit Gates. *Phys. Rev. Applied* **10,** 054062 (2018).

37. Mundada, P., Zhang, G., Hazard, T. & Houck, A. A. Suppression of Qubit Crosstalk in a Tunable Coupling Superconducting Circuit. *Phys. Rev. Applied* **12,** 054023 (2019).

38. Wootters, W. K. Entanglement of Formation of an Arbitrary State of Two Qubits. *Physical Review Letters* **80,** 2245–2248 (1998).

39. Zurek, W. H. Decoherence, einselection, and the quantum origins of the classical. *Rev. Mod. Phys.* **75,** 715–775. https://link.aps.org/doi/10.1103/RevModPhys.75.715 (3 May 2003).

40. Jacquod, P. & Petitjean, C. Decoherence, entanglement and irreversibility in quantum dynamical systems with few degrees of freedom. *Advances in Physics* **58,** 67–196. eprint: https://doi.org/10.1080/00018730902831009. https://doi.org/10.1080/00018730902831009 (2009).

41. Lindblad, G. On the generators of quantum dynamical semigroups. *Communications in Mathematical Physics* **48,** 119–130 (1976).

42. Gorini, V., Kossakowski, A. & Sudarshan, E. C. G. Completely positive dynamical semigroups of N-level systems. *Journal of Mathematical Physics* **17,** 821–825 (1976).

43. Breuer, H.-P. & Petruccione, F. *The Theory of Open Quantum Systems* ISBN: 978-0199213900 (Oxford University Press, 2007).

44. Andersen, C. K. *et al.* Repeated quantum error detection in a surface code. *Nature Physics* **16,** 875–880. https://doi.org/10.1038/s41567-020-0920-y (2020).

45. Leghtas, Z. *et al.* Hardware-Efficient Autonomous Quantum Memory Protection. *Phys. Rev. Lett.* **111,** 120501. https://link.aps.org/doi/10.1103/PhysRevLett.111.120501 (12 Sept. 2013).

46. Touzard, S. *et al.* Coherent Oscillations inside a Quantum Manifold Stabilized by Dissipation. *Phys. Rev. X* **8,** 021005. https://link.aps.org/doi/10.1103/PhysRevX.8.021005 (2 Apr. 2018).

47. Murch, K. W. *et al.* Cavity-assisted quantum bath engineering. *Physical Review Letters* **109,** 1–5. ISSN: 00319007. arXiv: 1207.0053 (2012).

48. Magnard, P. *et al.* Fast and Unconditional All-Microwave Reset of a Superconducting Qubit. *Phys. Rev. Lett.* **121,** 060502. https://link.aps.org/doi/10.1103/PhysRevLett.121.060502 (6 Aug. 2018).

49. Holland, E. T. *et al.* Single-Photon-Resolved Cross-Kerr Interaction for Autonomous Stabilization of Photon-Number States. *Phys. Rev. Lett.* **115,** 180501. https://link.aps.org/doi/10.1103/PhysRevLett.115.180501 (18 Oct. 2015).

50. Kimchi-Schwartz, M. E. *et al.* Stabilizing Entanglement via Symmetry-Selective Bath Engineering in Superconducting Qubits. *Phys. Rev. Lett.* **116,** 240503. https://link.aps.org/doi/10.1103/PhysRevLett.116.240503 (24 June 2016).

51. Harrington, P. M., Mueller, E. J. & Murch, K. W. Engineered dissipation for quantum information science. *Nature Reviews Physics* **4,** 660–671. https://doi.org/10.1038/s42254-022-00494-8 (2022).

52. Nakajima, S. On Quantum Theory of Transport Phenomena: Steady Diffusion. *Progress of Theoretical Physics* **20,** 948–959. ISSN: 0033-068X. eprint: https://academic.oup.com/ptp/article-pdf/20/6/948/5440766/20-6-948.pdf. https://doi.org/10.1143/PTP.20.948 (Dec. 1958).

53. Zwanzig, R. Ensemble Method in the Theory of Irreversibility. *The Journal of Chemical Physics* **33,** 1338–1341. eprint: https://doi.org/10.1063/1.1731409. https://doi.org/10.1063/1.1731409 (1960).

54. Aharonov, D., Kitaev, A. & Preskill, J. Fault-Tolerant Quantum Computation with Long-Range Correlated Noise. *Phys. Rev. Lett.* **96,** 050504. https://link.aps.org/doi/10.1103/PhysRevLett.96.050504 (5 Feb. 2006).

55. Alicki, R., Lidar, D. A. & Zanardi, P. Internal consistency of fault-tolerant quantum error correction in light of rigorous derivations of the quantum Markovian limit. *Phys. Rev. A* **73,** 052311. https://link.aps.org/doi/10.1103/PhysRevA.73.052311 (5 May 2006).

56. Rossini, M., Maile, D., Ankerhold, J. & Donvil, B. I. C. Single-Qubit Error Mitigation by Simulating Non-Markovian Dynamics. *Phys. Rev. Lett.* **131,** 110603. https://link.aps.org/doi/10.1103/PhysRevLett.131.110603 (11 Sept. 2023).

57. Reich, D. M., Katz, N. & Koch, C. P. Exploiting Non-Markovianity for Quantum Control. *Scientific Reports* **5.** ISSN: 2045-2322. http://dx.doi.org/10.1038/srep12430 (July 2015).

58. Vlachos, E. *et al.* Master equation emulation and coherence preservation with classical control of a superconducting qubit. *Phys. Rev. A* **106,** 062620. https://link.aps.org/doi/10.1103/PhysRevA.106.062620 (6 Dec. 2022).

59. Liu, Z.-D. *et al.* Experimental realization of high-fidelity teleportation via a non-Markovian open quantum system. *Phys. Rev. A* **102,** 062208. https://link.aps.org/doi/10.1103/PhysRevA.102.062208 (6 Dec. 2020).

60. Wolf, M. M., Eisert, J., Cubitt, T. S. & Cirac, J. I. Assessing Non-Markovian Quantum Dynamics. *Physical Review Letters* **101,** 150402 (2008).

61. Breuer, H.-P., Laine, E.-M. & Piilo, J. Measure for the Degree of Non-Markovian Behavior of Quantum Processes in Open Systems. *Physical Review Letters* **103,** 210401 (2009).

62. Breuer, H.-P., Laine, E.-M., Piilo, J. & Vacchini, B. Colloquium: Non-Markovian dynamics in open quantum systems. *Reviews of Modern Physics* **88,** 021002 (2016).

63. Rivas, Á., Huelga, S. F. & Plenio, M. B. Entanglement and Non-Markovianity of Quantum Evolutions. *Physical Review Letters* **105,** 050403 (2010).

64. Johansson, J. R., Nation, P. D. & Nori, F. QuTiP: An open-source Python framework for the dynamics of open quantum systems. *Computer Physics Communications* **183,** 1760–1772 (2012).

65. Johansson, J. R., Nation, P. D. & Nori, F. QuTiP 2: A Python framework for the dynamics of open quantum systems. *Computer Physics Communications* **184,** 1234–1240 (2013).

66. Misra, B. & Sudarshan, E. C. G. The Zeno's paradox in quantum theory. *Journal of Mathematical Physics* **18,** 756–763 (1977).

67. Facchi, P. & Pascazio, S. Quantum Zeno Subspaces. *Phys. Rev. Lett.* **89,** 080401 (2002).

68. Itano, W. M., Heinzen, D. J., Bollinger, J. J. & Wineland, D. J. Quantum Zeno effect. *Phys. Rev. A* **41,** 2295–2300 (1990).

69. Fischer, M. C., Gutiérrez-Medina, B. & Raizen, M. G. Observation of the quantum Zeno and anti-Zeno effects in an unstable system. *Phys. Rev. Lett.* **87,** 040402 (2001).

70. Shah, P. A. *et al. qiskit-community/qiskit-metal: Qiskit Metal 0.1.5a1 (2023)* version 0.1.5a1. June 2023. https://doi.org/10.5281/zenodo.8061781.

71. Barends, R. *et al.* Coherent Josephson Qubit Suitable for Scalable Quantum Integrated Circuits. *Phys. Rev. Lett.* **111,** 080502. https://link.aps.org/doi/10.1103/PhysRevLett.111.080502 (8 Aug. 2013).

72. Minev, Z. K. *et al. pyEPR: The energy-participation-ratio (EPR) open- source framework for quantum device design* https://github.com/zlatko-minev/pyEPR https://pyepr-docs.readthedocs.io/en/latest/. May 2021. https://doi.org/10.5281/zenodo.4744447%20https://github.com/zlatko-minev/pyEPR.

73. Wisbey, D. S., Martin, A., Reinisch, A. & Gao, J. New Method for Determining the Quality Factor and Resonance Frequency of Superconducting Micro-Resonators from Sonnet Simulations. *Journal of Low Temperature Physics* **176,** 538–544. https://doi.org/10.1007/s10909-014-1099-3 (2014).

74. Ranadive, A. *et al.* Kerr reversal in Josephson meta-material and traveling wave parametric amplification. *Nature Communications* **13,** 1737. https://doi.org/10.1038/s41467-022-29375-5 (2022).

75. Hutchings, M. D. & et al. Tunable Superconducting Qubits with Flux-Independent Coherence. *Phys. Rev. Applied* **8,** 044003 (2017).

76. Kundu, S. & et al. Efficient characterization of quantum devices using average gate fidelities. *npj Quantum Information* **5,** 74 (2019).

77. James, D. F. V., Kwiat, P. G., Munro, W. J. & White, A. G. Measurement of qubits. *Phys. Rev. A* **64,** 052312 (2001).

78. Coffman, V., Kundu, J. & Wootters, W. K. Distributed entanglement. *Phys. Rev. A* **61,** 052306 (2000).

79. Hatridge, M. *et al.* Quantum Back-Action of an Individual Variable-Strength Measurement. *Science* **339,** 178–181 (2013).

80. In the Supplemental Materials we provide further details on the experimental setup, system's Hamiltonian, numerical simulations, calibration of the parametric drive, device design, and quantum state tomography. The Supplemental Material contains additional references: [70–74, 166–168].

81. Harrington, P. M., Monroe, J. T. & Murch, K. W. Quantum Zeno Effects from Measurement Controlled Qubit-Bath Interactions. *Physical Review Letters* **118,** 1–5. ISSN: 10797114. arXiv: 1703.08371 (2017).

82. Misra, B. & Sudarshan, E. C. G. The Zeno's paradox in quantum theory. *Journal of Mathematical Physics* **18,** 756–763. ISSN: 0022-2488, 1089-7658. arXiv: arXiv:1011.1669v3. http://scitation.aip.org/content/aip/journal/jmp/18/4/10.1063/1.523304%7B%5C%%7D5Cnhttp://scitation.aip.org/deliver/fulltext/aip/journal/jmp/18/4/1.523304.pdf;jsessionid=4hhg6b15ak221.x-aip-live-03?itemId=/content/aip/journal/jmp/18/4/10.1063/1.523304%7B%5C&%7DmimeType=pdf (1977).

83. Itano, W. M., Heinzen, D. J., Bollinger, J. J. & Wineland, D. J. Quantum Zeno effect. *Physical Review A* **41,** 2295–2300. ISSN: 1094-1622. http://dx.doi.org/10.1103/PhysRevA.41.2295 (Mar. 1990).

84. Kakuyanagi, K. *et al.* Observation of quantum Zeno effect in a superconducting flux qubit. *New Journal of Physics* **17,** 63035. ISSN: 13672630. http://dx.doi.org/10.1088/1367-2630/17/6/063035 (2015).

85. Hacohen-Gourgy, S., García-Pintos, L. P., Martin, L. S., Dressel, J. & Siddiqi, I. Incoherent Qubit Control Using the Quantum Zeno Effect. *Physical Review Letters* **120.** ISSN: 1079-7114. http://dx.doi.org/10.1103/PhysRevLett.120.020505 (Jan. 2018).

86. Blumenthal, E. *et al.* Demonstration of universal control between non-interacting qubits using the Quantum Zeno effect. *npj Quantum Information* **8.** ISSN: 2056-6387. http://dx.doi.org/10.1038/s41534-022-00594-4 (July 2022).

87. Slichter, D. H. *et al.* Quantum Zeno effect in the strong measurement regime of circuit quantum electrodynamics. *New Journal of Physics* **18,** 053031. ISSN: 1367-2630. http://dx.doi.org/10.1088/1367-2630/18/5/053031 (May 2016).

88. Patsch, S., Maniscalco, S. & Koch, C. P. Simulation of open-quantum-system dynamics using the quantum Zeno effect. *Phys. Rev. Res.* **2,** 023133. https://link.aps.org/doi/10.1103/PhysRevResearch.2.023133 (2 May 2020).

89. Gambetta, J. *et al.* Quantum trajectory approach to circuit QED: Quantum jumps and the Zeno effect. *Phys. Rev. A* **77,** 012112. https://link.aps.org/doi/10.1103/PhysRevA.77.012112 (1 Jan. 2008).

90. Al-Nasrallah, E., Das, S., Illuminati, F., Petruzziello, L. & Vagenas, E. C. Discriminating quantum gravity models by gravitational decoherence. *Nuclear Physics B* **992,** 116246. ISSN: 0550-3213. http://dx.doi.org/10.1016/j.nuclphysb.2023.116246 (July 2023).

91. Friis, H. T. Noise Figures of Radio Receivers. *Proceedings of the IRE* **32,** 419–422 (1944).

92. Caves, C. M. Quantum limits on noise in linear amplifiers. *Phys. Rev. D* **26,** 1817–1839 (1982).

93. Clerk, A. A., Devoret, M. H., Girvin, S. M., Marquardt, F. & Schoelkopf, R. J. Introduction to quantum noise, measurement, and amplification. *Reviews of Modern Physics* **82,** 1155–1208 (2010).

94. Devoret, M. H. & Schoelkopf, R. J. Superconducting circuits for quantum information: an outlook. *Science* **339,** 1169–1174 (2013).

95. Louisell, W. H., Yariv, A. & Siegman, A. E. Quantum fluctuations and noise in parametric processes. I. *Phys. Rev.* **124,** 1646–1654 (1961).

96. Tinkham, M. *Introduction to Superconductivity* (Dover Publications, 2004).

97. Yurke, B. *et al.* Observation of parametric amplification and deamplification in a Josephson parametric amplifier. *Physical Review A* **39,** 2519–2533 (1988).

98. Devoret, M. H. *Quantum Fluctuations in Electrical Circuits* in *Quantum Fluctuations, Les Houches Session LXIII* (eds Reynaud, S., Giacobino, E. & Zinn-Justin, J.) Comprehensive introduction to circuit quantization (Elsevier, Amsterdam, 1997), 351–386.

99. Boyd, R. W. *Nonlinear Optics* 4th (Academic Press, 2020).

100. Frattini, N. E. *et al.* 3-wave mixing Josephson dipole element. *Applied Physics Letters* **110,** 222603 (2017).

101. Devoret, M. & Roy, A. Introduction to Quantum-limited Parametric Amplification of Quantum Signals with Josephson Circuits. *Comptes Rendus Physique* **17,** 740–755. eprint: `arXiv:1605.00539` (2016).

102. Castellanos-Beltran, M. A., Irwin, K. D., Hilton, G. C., Vale, L. R. & Lehnert, K. W. Amplification and squeezing of quantum noise with a tunable Josephson metamaterial. *Nature Physics* **4,** 929–931 (2008).

103. Matthaei, G. L., Young, L. & Jones, E. M. T. *Microwave Filters, Impedance-Matching Networks, and Coupling Structures* (McGraw–Hill, New York, 1964).

104. Pozar, D. M. *Microwave Engineering* 4th ed. ISBN: 978-0-470-63155-3 (Wiley, Hoboken, NJ, 2012).

105. Kaufman, R., Hacohen-Gourgy, S., Siddiqi, I., *et al.* Josephson parametric amplifier with Chebyshev gain profile using a band-pass impedance-matching network. *Physical Review Applied* **20,** 054058 (2023).

106. Grebel, J. *et al.* Flux-pumped impedance-engineered broadband Josephson parametric amplifier. *Applied Physics Letters* **118,** 142601 (2021).

107. Ranzani, L., Ribeill, G., Hassick, B. & Fong, K. C. *Wideband Josephson Parametric Amplifier with Integrated Transmission Line Transformer* arXiv:2208.02331. 2022. `https://arxiv.org/abs/2208.02331`.

108. Qing, B. *et al.* Broadband coplanar-waveguide-based impedance-transformed Josephson parametric amplifier. *Physical Review Research* **6,** L012035 (2024).

109. Roy, A. & Devoret, M. Quantum-limited parametric amplification with Josephson circuits in the regime of pump depletion. *Physical Review B* **98,** 045405 (2018).

110. Bode, H. W. *Network Analysis and Feedback Amplifier Design* (D. Van Nostrand, New York, 1945).

111. Fano, R. M. Theoretical limitations on the broadband matching of arbitrary impedances. *Journal of the Franklin Institute* **249,** 57–83, 139–154 (1950).

112. Kerr, A. R. *Some Fundamental and Practical Limits on Broadband Matching to Capacitive Devices and the Implications for SIS Mixer Design* tech. rep. (NRAO Electronics Division Internal Report No. 295, Charlottesville, VA, 1993).

113. Ranzani, L., Bardin, J. C., Hurst, P. K. & Walker, R. C. *A 4:1 Transmission-Line Impedance Transformer for Superconducting MMICs* tech. rep. Demonstrates superconducting Ruthroff-type TLTs for wideband matching (NIST, 2012).

114. Sakurai, J. J. & Napolitano, J. *Modern Quantum Mechanics* 2nd. ISBN: 978-0805382914 (Pearson, 2011).

115. Siegman, A. E. *Lasers* ISBN: 978-0935702118 (University Science Books, 1986).

116. Miri, M.-A. & Alù, A. Exceptional points in optics and photonics. *Science* **363,** eaa7709 (2019).

117. Bender, C. M. & Boettcher, S. Real Spectra in Non-Hermitian Hamiltonians Having $\mathcal{PT}$ Symmetry. *Physical Review Letters* **80,** 5243–5246. https://doi.org/10.1103/physrevlett.80.5243 (June 1998).

118. El-Ganainy, R. *et al.* Non-Hermitian physics and PT symmetry. *Nature Physics* **14,** 11 (2018).

119. Guo, A. *et al.* Observation of $\mathcal{PT}$-Symmetry Breaking in Complex Optical Potentials. *Phys. Rev. Lett.* **103,** 093902. https://link.aps.org/doi/10.1103/PhysRevLett.103.093902 (9 Aug. 2009).

120. Rüter, C. E. *et al.* Observation of parity—time symmetry in optics. *Nature physics* **6,** 192 (2010).

121. And Sahin Kaya Özdemir and Fuchuan Lei and Faraz Monifi and Mariagiovanna Gianfreda and Gui Lu Long and Shanhui Fan and Franco Nori and Carl M. Bender, B. P. & Yang, L. Parity-time-symmetric whispering-gallery microcavities. *Nature Physics* **10,** 394–398 (2014).

122. Hodaei, H., Miri, M.-A., Heinrich, M., Christodoulides, D. N. & Khajavikhan, M. Parity-time-symmetric microring lasers. *Science* **346,** 975–978 (2014).

123. Zeuner, J. M. *et al.* Observation of a Topological Transition in the Bulk of a Non-Hermitian System. *Phys. Rev. Lett.* **115,** 040402 (4 July 2015).

124. Li, J. *et al.* Observation of parity-time symmetry breaking transitions in a dissipative Floquet system of ultracold atoms. *Nature Communications* **10,** 855. https://doi.org/10.1038/s41467-019-08596-1 (Feb. 2019).

125. Xiao, L. *et al.* Observation of topological edge states in parity-time-symmetric quantum walks. *Nature Physics* **13,** 1117–1123. https://doi.org/10.1038/nphys4204 (July 2017).

126. Özdemir, Ş. K., Rotter, S., Nori, F. & Yang, L. Parity–time symmetry and exceptional points in photonics. *Nature Materials* **18,** 783–798. https://doi.org/10.1038/s41563-019-0304-9 (Apr. 2019).

127. Miri, M.-A. & Alù, A. Exceptional points in optics and photonics. *Science* **363,** eaar7709. https://doi.org/10.1126/science.aar7709 (Jan. 2019).

128. Wiersig, J. Enhancing the Sensitivity of Frequency and Energy Splitting Detection by Using Exceptional Points: Application to Microcavity Sensors for Single-Particle Detection. *Phys. Rev. Lett.* **112,** 203901. https://link.aps.org/doi/10.1103/PhysRevLett.112.203901 (20 May 2014).

129. Hodaei, H. *et al.* Enhanced sensitivity at higher-order exceptional points. *Nature* **548,** 187 (2017).

130. Xu, H., Mason, D., Jiang, L. & Harris, J. G. E. Topological energy transfer in an optomechanical system with exceptional points. *Nature* **537,** 80–83. https://doi.org/10.1038/nature18604 (July 2016).

131. Naghiloo, M., Abbasi, M., Joglekar, Y. N. & Murch, K. W. Quantum state tomography across the exceptional point in a single dissipative qubit. *Nature Physics* **15,** 1232–1236. https://doi.org/10.1038/s41567-019-0652-z (Oct. 2019).

132. Chen, W., Abbasi, M., Joglekar, Y. N. & Murch, K. W. Quantum Jumps in the Non-Hermitian Dynamics of a Superconducting Qubit. *Physical Review Letters* **127.** https://doi.org/10.1103/physrevlett.127.140504 (Sept. 2021).

133. Chen, W. *et al.* Decoherence-Induced Exceptional Points in a Dissipative Superconducting Qubit. *Physical Review Letters* **128.** https://doi.org/10.1103/physrevlett.128.110402 (Mar. 2022).

134. Abbasi, M., Chen, W., Naghiloo, M., Joglekar, Y. N. & Murch, K. W. Topological Quantum State Control through Exceptional-Point Proximity. *Physical Review Letters* **128.** https://doi.org/10.1103/physrevlett.128.160401 (Apr. 2022).

135. Wang, K. *et al.* Experimental realization of continuous-time quantum walks on directed graphs and their application in PageRank. *Optica* **7,** 1524. https://doi.org/10.1364/optica.396228 (Nov. 2020).

136. Wu, Y. *et al.* Observation of parity-time symmetry breaking in a single-spin system. *Science* **364,** 878–880. https://doi.org/10.1126/science.aaw8205 (May 2019).

137. Liu, W., Wu, Y., Duan, C.-K., Rong, X. & Du, J. Dynamically Encircling an Exceptional Point in a Real Quantum System. *Physical Review Letters* **126.** https://doi.org/10.1103/physrevlett.126.170506 (Apr. 2021).

138. Wang, Y.-X. & Clerk, A. A. Non-Hermitian dynamics without dissipation in quantum systems. *Physical Review A* **99.** https://doi.org/10.1103/physreva.99.063834 (June 2019).

139. Aumentado, J. Superconducting Parametric Amplifiers: The State of the Art in Josephson Parametric Amplifiers. *IEEE Microwave Magazine* **21,** 45–59. https://doi.org/10.1109/mmm.2020.2993476 (Aug. 2020).

140. Yamamoto, T. *et al.* Flux-driven Josephson parametric amplifier. *Applied Physics Letters* **93,** 042510. https://doi.org/10.1063/1.2964182 (July 2008).

141. Clerk, A. Introduction to quantum non-reciprocal interactions: from non-Hermitian Hamiltonians to quantum master equations and quantum feedforward schemes. *SciPost Physics Lecture Notes*. https://doi.org/10.21468/scipostphyslectnotes.44 (Mar. 2022).

142. Lau, H.-K. & Clerk, A. A. Fundamental limits and non-reciprocal approaches in non-Hermitian quantum sensing. *Nature Communications* **9.** https://doi.org/10.1038/s41467-018-06477-7 (Oct. 2018).

143. Budich, J. C. & Bergholtz, E. J. Non-Hermitian Topological Sensors. *Physical Review Letters* **125.** https://doi.org/10.1103/physrevlett.125.180403 (Oct. 2020).

144. Shindou, R., Matsumoto, R., Murakami, S. & Ohe, J.-i. Topological chiral magnonic edge mode in a magnonic crystal. *Physical Review B* **87.** https://doi.org/10.1103/physrevb.87.174427 (May 2013).

145. Peano, V., Houde, M., Brendel, C., Marquardt, F. & Clerk, A. A. Topological phase transitions and chiral inelastic transport induced by the squeezing of light. *Nature Communications* **7.** https://doi.org/10.1038/ncomms10779 (Mar. 2016).

146. Peano, V., Houde, M., Marquardt, F. & Clerk, A. A. Topological Quantum Fluctuations and Traveling Wave Amplifiers. *Physical Review X* **6.** https://doi.org/10.1103/physrevx.6.041026 (Nov. 2016).

147. Chen, W., Leykam, D., Chong, Y. & Yang, L. Nonreciprocity in synthetic photonic materials with nonlinearity. *MRS Bulletin* **43,** 443–451. https://doi.org/10.1557/mrs.2018.124 (2018).

148. Nasari, H., Pyrialakos, G. G., Christodoulides, D. N. & Khajavikhan, M. Non-Hermitian topological photonics. *Optical Materials Express* **13,** 870. https://doi.org/10.1364/ome.483361 (Mar. 2023).

149. Hodaei, H. *et al.* Enhanced sensitivity at higher-order exceptional points. *Nature* **548,** 187–191. https://doi.org/10.1038/nature23280 (Aug. 2017).

150. Chen, W., Özdemir, Ş. K., Zhao, G., Wiersig, J. & Yang, L. Exceptional points enhance sensing in an optical microcavity. *Nature* **548,** 192–196 (2017).

151. Abbasi, M., Chen, W., Naghiloo, M., Joglekar, Y. N. & Murch, K. W. Topological quantum state control through exceptional-point proximity. en. *Phys. Rev. Lett.* **128,** 160401 (Apr. 2022).

152. Kjaergaard, M. *et al.* Superconducting Qubits: Current State of Play. *Annual Review of Condensed Matter Physics* **11,** 369–395 (2020).

153. Murch, K. W. *et al.* Quantum fluctuations in the chirped pendulum. *Nature Physics* **7,** 105–108. https://doi.org/10.1038/nphys1867 (Dec. 2010).

154. Chen, Q.-M. *et al.* Quantum behavior of the Duffing oscillator at the dissipative phase transition. *Nature Communications* **14.** https://doi.org/10.1038/s41467-023-38217-x (May 2023).

155. Planat, L. *et al.* Understanding the Saturation Power of Josephson Parametric Amplifiers Made from SQUID Arrays. *Physical Review Applied* **11.** https://doi.org/10.1103/physrevapplied.11.034014 (Mar. 2019).

156. Bender, C. M. & Boettcher, S. Real spectra in non-Hermitian Hamiltonians having PT symmetry. *Physical Review Letters* **80,** 5243–5246 (1998).

157. Breuer, H.-P. & Petruccione, F. *The Theory of Open Quantum Systems* (Oxford University Press, 2002).

158. Heiss, W. The physics of exceptional points. *Journal of Physics A: Mathematical and Theoretical* **45,** 444016 (2012).

159. Gardiner, C. W. & Zoller, P. *Quantum Noise* (Springer, 2004).

160. Yamamoto, T. *et al.* Flux-driven Josephson parametric amplifier. *Applied Physics Letters* **93,** 042510 (2008).

161. Castellanos-Beltran, M. A. & Lehnert, K. W. Amplification and squeezing of quantum noise with a tunable Josephson metamaterial. *Applied Physics Letters* **91,** 083509 (2007).

162. Yurke, B. *et al.* Observation of parametric amplification and deamplification in a Josephson parametric amplifier. *Physical Review Letters* **60,** 764–767 (1988).

163. Johansson, J., Nation, P. & Nori, F. QuTiP: An open-source Python framework for the dynamics of open quantum systems. *Computer Physics Communications* **183,** 1760–1772. ISSN: 00104655 (8 Aug. 2012).

164. Johansson, J., Nation, P. & Nori, F. QuTiP 2: A Python framework for the dynamics of open quantum systems. *Computer Physics Communications* **184,** 1234–1240. ISSN: 00104655 (4 Apr. 2013).

165. Frattini, N. E., Sivak, V. V., Lingenfelter, A., Shankar, S. & Devoret, M. H. Optimizing the Nonlinearity and Dissipation of a SNAIL Parametric Amplifier for Dynamic Range. *Phys. Rev. Appl.* **10,** 054020. https://link.aps.org/doi/10.1103/PhysRevApplied.10.054020 (5 Nov. 2018).

166. Virtanen, P. *et al.* SciPy 1.0: Fundamental Algorithms for Scientific Computing in Python. *Nature Methods* **17,** 261–272 (2020).

167. Johansson, J., Nation, P. & Nori, F. QuTiP: An open-source Python framework for the dynamics of open quantum systems. *Computer Physics Communications* **183,** 1760–1772. ISSN: 0010-4655. https://www.sciencedirect.com/science/article/pii/S0010465512000835 (2012).

168. Johansson, J., Nation, P. & Nori, F. QuTiP 2: A Python framework for the dynamics of open quantum systems. *Computer Physics Communications* **184,** 1234–1240. ISSN: 0010-4655. https://www.sciencedirect.com/science/article/pii/S0010465512003955 (2013).